

VERY MASSIVE STARS : MASS DETERMINATION AND
FATE

NORHASLIZA BINTI YUSOF

THESIS SUBMITTED IN FULFILLMENT OF THE
REQUIREMENTS FOR THE DEGREE OF
DOCTOR OF PHILOSOPHY

FACULTY OF SCIENCE
UNIVERSITY OF MALAYA
KUALA LUMPUR

2012

UNIVERSITI MALAYA
ORIGINAL LITERARY WORK DECLARATION

Name of Candidate: Norhasliza binti Yusof (I.C/Passport No: 800710-07-5396)
Registration/Matric No: SHC070063
Name of Degree: Doctor of Philosophy
Title of Thesis ("this Work"): Very Massive Stars : Mass Determination and Fate

Field of Study: Theoretical Nuclear Astrophysics

I do solemnly and sincerely declare that:

- (1) I am the sole author/writer of this Work;
- (2) This Work is original;
- (3) Any use of any work in which copyright exists was done by way of fair dealing and for permitted purposes and any excerpt or extract form, or reference to or reproduction of any copyright work has been disclosed expressly and sufficiently and the title of the Work and its authorship have been acknowledged in this Work;
- (4) I do not have any actual knowledge nor do I ought reasonably to know that the making of this work constitutes an infringement of any copyright work;
- (5) I hereby assign all and every rights in the copyright to this Work to the University of Malaya ("UM"), who henceforth shall be owner of the copyright in this Work and that any reproduction or use in any form or by any means whatsoever is prohibited without the written consent of UM having been first had and obtained;
- (6) I am fully aware that if in the course of making this Work I have infringed any copyright whether intentionally or otherwise, I may be subject to legal action or any other action as may be determined by UM.

Candidate's Signature:

Date 31 July 2012

Subscribed and solemnly declared before,

Witness's Signature:

Date 31 July 2012

Name: Hasan Abu Kassim

Designation: Associate Professor

Abstract

The first generation of stars is thought to have been very massive (150-300 M_{\odot}) and produces pair creation supernovae (PCSNe) at the end of their life. However, the chemical signature of PCSNe is not observed in extremely metal poor stars (e.g. Umeda & Nomoto, 2002) and it raises the following questions: Were stars born less (or more massive) than the mass range expected to lead to the PCSNe? Or is mass loss too strong during the evolution of these stars and prevented them from retaining enough mass to produce PCSNe? The discovery of very massive stars (VMS, $M > 100 M_{\odot}$) in the Milky Way and LMC (Crowther et al., 2010) shows that VMS can form and exist. The observation of PCSN candidates (SN 2006gy & SN 2007bi) also seems to indicate that such supernovae (SNe) may occur. Mass loss plays a crucial role in the life of VMS since the star will only die as a PCSN if the star retains a high mass throughout its life. In this thesis, we shall describe the dependence of VMS evolution on metallicity and present stellar evolution models at various metallicities, including the effects of mass loss and rotation. Based on our models, we will give our predictions concerning the fate of these VMS, either a PCSN or supernova Type Ic (SN Ic) as a function of metallicity and mass loss rate prescriptions used. Our models that predict the star will end up as PCSN are models at LMC metallicity with mass around 500 M_{\odot} and rotating SMC metallicity models with mass $120 < M_{\odot} < 280$. Other than that it will die as a black hole or a core-collapse supernova. We also study the impact of the updated neutrino energy loss from Itoh et al. (1996) that supersedes the neutrino energy loss from Itoh et al. (1989) which has been used in the Geneva stellar evolution code. Neutrino energy loss is an important process in

the evolution of advanced stages of massive stars since most of the energy loss is through the neutrino processes. From our study, the VMS do not have any significant effects when we update the neutrino energy loss. This is due to the prominent process in neutrino energy loss which is photoneutrino process that remains unchanged in Itoh et al. (1996). Finally we apply an updated nuclear reaction rates using WKB method for $^{12}\text{C}(p,\gamma)^{13}\text{N}$, $^{15}\text{N}(p,\gamma)^{16}\text{O}$ and $^{16}\text{O}(p,\gamma)^{17}\text{F}$ in the CNO cycle. Evolution of massive and very massive stars are studied and we find the new reaction rates influence the surface and central abundances of ^{12}C in these stars.

Abstrak

Generasi pertama bintang difikirkan mempunyai jisim yang sangat tinggi (150-300 M_{\odot}) dan menghasilkan supernova pengwujudan pasangan (PCSNe) disaat kematiannya. Tetapi tanda kimia PCSNe ini tidak dapat dicerap pada bintang yang mempunyai kandungan logam yang sangat rendah (sebagai contoh Umeda & Nomoto, 2002) dan ini menimbulkan persoalan-persoalan berikut: Adakah bintang dilahirkan lebih ringan (atau berat) dari jisim yang dijangka untuk menjadi PCSNe? Atau adakah kehilangan jisim amat kuat semasa evolusi menyekat bintang-bintang ini dari menyimpan jisim secukupnya untuk menghasilkan PCSNe? Penemuan bintang sangat berjisim ($VMS > 100M_{\odot}$) di Bima Sakti dan LMC (Crowther et al., 2010) menunjukkan VMS boleh terbentuk dan wujud. Cerapan calon PCSN (SN 2006gy dan SN2007bi) juga menunjukkan supernova (SNe) jenis ini boleh wujud. Kehilangan jisim memainkan peranan penting dalam kehidupan VMS ini memandangkan ia hanya boleh mati sebagai PCSN jika ia dapat mengekalkan sejumlah besar jisim sepanjang hayatnya. Di dalam tesis ini, akan diterangkan pengantungan evolusi VMS ke atas kelogaman dan akan mempersembahkan model evolusi bintang pada beberapa kelogaman termasuk kesan kehilangan jisim dan putaran. Berdasarkan model tersebut, jangkaan akan diberi berkenaan takdir VMS samada ia sebagai PCSN atau supernova Jenis Ic (SN Ic) sebagai fungsi kelogaman dan kadar kehilangan jisim yang digunakan. Model di dalam kerja ini menjangkakan bintang tersebut akan mati sebagai PCSN pada kelogaman LMC sekitar 500 M_{\odot} dan model putaran SMC dengan jisim diantara $120 < M_{\odot} < 280$. Selain itu, ia akan mati sebagai lohong hitam atau

supernova teras-runtuh. Kajian juga dibuat terhadap impak kehilangan tenaga neutrino yang dikemaskini dari Itoh et al. (1996) yang menggantikan kehilangan tenaga neutrino Itoh et al. (1989) yang telah digunapakai dalam kod evolusi bintang Geneva. Kehilangan tenaga neutrino adalah proses penting dalam evolusi bintang sangat berjisim pada peringkat lanjut memandangkan hampir kesemua tenaga hilang adalah melalui proses neutrino ini. Daripada kajian ini, didapati VMS tidak mengalami sebarang kesan bererti apabila kehilangan tenaga neutrino dikemaskinikan. Ini adalah disebabkan proses yang menonjol dalam kehilangan tenaga neutrino iaitu proses fotoneutrino masih tidak berubah di dalam Itoh et al. (1996). Akhir sekali, tindakbalas nuklear dikemaskini melalui kaedah WKB digunakan untuk $^{12}\text{C}(p,\gamma)^{13}\text{N}$, $^{15}\text{N}(p,\gamma)^{16}\text{O}$ dan $^{16}\text{O}(p,\gamma)^{17}\text{F}$ dalam kitaran CNO. Evolusi bintang berjisim dan sangat berjisim dikaji dan didapati kadar tindakbalas baru ini mempengaruhi kelimpahan ^{12}C di permukaan dan pusat bintang tersebut.

Acknowledgments

I would like to thank both my supervisors, Associate Professor Dr Hasan Abu Kassim and Dr Raphael Hirschi: Hasan Abu Kassim for his support, advice, kindness and trust he gave to me to do my work; Raphael Hirschi for always available when I need scientific advice although we always discuss in different time zones, his support and hospitality whenever I visited him in Keele. Both of them give me the best of both worlds.

Many thanks to my colleagues both in Keele University and University of Malaya. To Nor Sofiah Ahmad, my junior colleague who always help me in managing the Theoretical Physics Laboratory. Without her, I will not be able to do all the paper work for our lab. I also extend my thanks to Azni, Siti Madiha, Iza, Nazrul, Noora and Mahirah whom always cheer up our lab.

I am indebted to my colleagues who share the PhD supervision with Dr Hirschi, Michael Bennett and Urs Frischknecht whom I always enjoy sharing many scientific chats and also have helped me in learning Python and Matplotlib. Thanks to Dr Olivier Schnurr who have introduced the observational information for very massive stars and Professor Paul Crowther for inviting me and my supervisors to join the collaboration in the quest of very massive stars.

Thanks to my family especially to Mak and Abah whom have always supported my academic career. Their support and prayers have provided me emotional strength whenever I need it the most. Also to both my brother and my sister whom are most willing to become my financial guarantors for my scholarship. Without them, I am not able to

finish my studies.

I also want to extend my gratitude to the former Head of Physics Department, Professor Abdul Kariem Mohd Arof who always support my PhD studies. Special thanks to Dr Robert Breault, one of my mentors who has always encourage me to pursue my PhD studies. I am very touched when he came to visit me during his visit to Kuala Lumpur in 2009 after about 8 years from our first meeting.

Finally I want to thank University of Malaya and Ministry of Higher Education of Malaysia for my PhD SLAI scholarship, UNESCO under Programme Priorities Support 2008-2009 for funding my visit to Keele for six month on Feb 08-July 09 and Commonwealth Split-Site Scholarship for funding part of my research in Keele University. I also gratefully acknowledge the University of Malaya and Ministry of Higher Education, Malaysia for financial support through the Fundamental Research Grant (FGRS), FP036/2008C.

Contents

Abstract	i
Abstrak	iii
Acknowledgments	v
List of Figures	viii
List of Tables	ix
1 Introduction	1
1.1 The life of very massive stars	1
1.1.1 Observations and mass determination of very massive stars	3
1.2 Physics of massive stars	4
1.2.1 Mass loss	4
1.2.2 Rotation	6
1.2.3 Neutrino energy loss	7
1.2.4 Nuclear reaction rates	8
1.3 Summary	8
1.4 Overview of the thesis	8
2 Geneva Stellar Evolution Code	10

2.1	Introduction	10
2.2	Stellar structure equations and its physical ingredients	12
2.2.1	Rotation	14
2.2.2	Nuclear networks	17
2.2.3	Opacity	21
2.2.4	Mass Loss	21
2.2.5	Equation of State	27
2.2.6	Convection	27
2.2.7	Overshooting	28
2.2.8	Neutrino Energy Loss	28
3	Main Sequence Phase of Very Massive Stars: Comparison with Observations	29
3.1	Motivation	29
3.2	Observations	31
3.3	Main sequence models	32
3.3.1	Physics of the models	33
3.3.2	Evolution of the main sequence models	33
3.4	Mass determination of the most massive stars	36
3.4.1	Verification of the mass determination : NGC3603	36
3.4.2	Mass determination of the most massive star: R136a1	40
3.5	Summary	42
4	Post Main Sequence and Fate of Very Massive Stars	43
4.1	Introduction	43
4.2	Wolf-Rayet stars	45
4.2.1	Observational classification for WR stars	46
4.2.2	Classification scheme applicable to Geneva stellar evolution code	47

4.3	Supernova classification	48
4.3.1	SN2006gy	49
4.3.2	SN2007bi	50
4.4	Physics of the models	52
4.5	Hetzprung-Russell (HR) lifetimes and diagrams	54
4.5.1	Lifetimes and surface properties	54
4.5.2	Hertzprung Russell diagrams	59
4.6	Eddington limit	61
4.7	Internal structure evolution	63
4.7.1	Central evolution	63
4.7.2	Kippenhahn diagrams	66
4.8	Fate of very massive stars	67
4.8.1	Final mass and mass of carbon-oxygen core	70
4.8.2	Surface He abundance for SNe Ib/Ic	71
4.9	Comparison with the literature	75
4.9.1	Post-main sequence evolution of very massive stars	75
4.9.2	Comparison for the fate of very massive stars	77
4.10	Initial mass range for SN2007bi progenitors	78
4.11	Mass loss effect using different mass loss prescriptions	79
4.12	Summary	87
5	Neutrino Energy Loss in Massive Stars	88
5.1	Neutrino loss in massive stars	88
5.2	Neutrino Processes	89
5.2.1	Pair neutrino process	91
5.2.2	Photoneutrino process	92
5.2.3	Plasma neutrino process	92

5.2.4	Bremsstrahlung neutrino process	93
5.3	Numerical aspect	95
5.4	Neutrino energy losses for 20, 60 and 120 M_{\odot} solar metallicity models . .	96
5.4.1	HR diagram	96
5.4.2	Internal evolution	97
5.4.3	Comparison of neutrino energy loss	97
5.4.4	Kippenhahn diagrams	106
5.5	Summary	108
6	Updated Nuclear Reaction Rate Using WKB Method and Application	
	in the Evolution of Massive Stars	109
6.1	Motivation	109
6.2	WKB method and astrophysical S-factor	111
6.2.1	S-factor	112
6.2.2	Derivation of effective energy	119
6.2.3	Updated reaction rates	120
6.3	Application to stellar models: 20 M_{\odot} and 120 M_{\odot} solar metallicity models	124
6.4	Hertzsprung-Russell and Kippenhahn diagrams	125
6.4.1	Surface abundances	126
6.4.2	Central abundances	134
6.5	Summary	137
7	Conclusions and Future Work	138
7.1	Stellar evolution models-life and fate of very massive stars	138
7.2	Neutrino energy loss	139
7.3	Updated nuclear reaction rates	140
7.4	Future work	140

A List of Publications **142**

Bibliography **151**

*

List of Figures

1.1	Evolutionary tracks from Langer et al. (2007) in the $\log T_c - \rho_c$ diagram. The instability region is indicated as $\Gamma < 4/3$. Shown in blue is the slowly rotating $150 M_\odot$ model at $Z = Z_\odot/20$, and the $250 M_\odot$ model at $Z = Z_\odot/20$ entering the instability region.	2
1.2	Artist's illustration of R136a1 (credit to European South Observatory). .	4
1.3	Mass loss rates of rotating $120 M_\odot$ and $300 M_\odot$ models with solar metallicity ($Z = 0.014$).	5
1.4	Probability density in km s^{-1} of rotation velocity for 496 stars with O9.5 to B8 (Huang & Gies, 2006).	7
2.1	The pp chain and CNO tri-cycle diagram. The underline reaction rates are explicitly considered (Maeder, 1983).	18
3.1	A Hubble Space Telescope image of R136 (<i>left</i>) and NGC3603 (<i>right</i>). In the center of star-forming region 30 Doradus lies a huge cluster of the largest, hottest, most massive stars known as R136 (N. Walborn, STScI). Image of NGC3603 recorded by Hubble's Advanced Camera for Surveys, the image spans about 17 light-years (NASA, 2007).	30

3.2	VLT MAD K_s -band 12×12 arcsec (3×3 parsec for the LMC distance of 49 kpc) image of R136 (Campbell et al. (2010) together with a view of the central 4×4 arcsec (1×1 parsec) in which the very massive WN5h stars discussed in this thesis are labeled (component b is a lower mass WN9h star). Relative photometry agrees closely with integral field SINFONI observations (Schnurr et al. 2009).	32
3.3	Comparison between main sequence evolutionary predictions for both rotating ($Z = 0.006$:H120z06S400) and non-rotating ($Z = 0.006$:H120z06S000, $Z = 0.014$:H120z14S000) $120 M_{\odot}$ models. For model H120z06S400, the horizontal lines in the top left-hand panel correspond to the transition to the WR phase, phase during which the photosphere is in the wind rather than at the surface of the star.	34
3.4	Comparison between surface abundances and mass loss rate for both rotating ($Z = 0.006$: H120z06S400) and non-rotating ($Z = 0.006$:H120z06S000, $Z = 0.014$: H120z14S000) $120 M_{\odot}$ models.	35
3.5	Comparison between solar metallicity ($Z = 1.4\%$) models calculated for the main-sequence evolution of 85 - $200 M_{\odot}$ stars (initially rotating at $V_{\text{init}}/v_{\text{crit}} = 0.4$ [dotted] and 0 [solid]), and the physical properties derived from spectroscopic analysis of NGC 3603 WN6h stars.	37
3.6	Comparison between LMC-metallicity models calculated for the main-sequence evolution of 85 - $500 M_{\odot}$ stars, initially rotating at $v_{\text{init}}/v_{\text{crit}} = 0.4$ (dotted) or 0 (solid) and the physical properties derived from our spectroscopic analysis.	41
4.1	SNe classification (Turatto, 2003)	50

4.2	a: The R-band light curve of SN2007bi. b: Comparison with theoretical light curve of PCSN model with SN2007Bi observation (Gal-Yam et al., 2009).	51
4.3	HR diagrams of rotating solar, LMC and SMC metallicities.	60
4.4	Γ_{Edd} of $150 M_{\odot}$ in solar, LMC and SMC metallicities as a function of time before core-collapse. Solid line represents rotating models and dashed line represents non-rotating models.	61
4.5	Mass loss rate of $150 M_{\odot}$ in solar metallicity both rotating and non-rotating models as a function of mass loss. Right panel: Effective temperature of $150 M_{\odot}$ in solar, LMC and SMC metallicities as a function of time before core collapse.	62
4.6	Log T_c vs Log ρ_c diagrams: Evolutionary tracks for 150 - $500 M_{\odot}$ models for solar metallicity (left panel) and the evolutionary tracks zoomed in the advanced stages for 150 - $500 M_{\odot}$ models (left panel). The additional dotted line corresponds to the limit between non-degenerate and degenerate electron gas ($P^{elperfectgas} = P^{eldegenerategas}$). The gray shaded area is the pair instability region.	64
4.7	Log T_c vs Log ρ_c diagrams: Evolutionary tracks for 150 - $500 M_{\odot}$ models for LMC metallicity. The additional dotted line corresponds to the limit between non-degenerate and degenerate electron gas ($P^{elperfectgas} = P^{eldegenerategas}$). The gray shaded area is the instability region.	65
4.8	Log T_c vs Log ρ_c diagrams: Evolutionary tracks for 150 - $500 M_{\odot}$ models for SMC metallicity. The additional dotted line corresponds to the limit between non-degenerate and degenerate electron gas ($P^{elperfectgas} = P^{eldegenerategas}$). The gray shaded area is the instability region.	66

4.9	Kippenhahn diagrams for non-rotating and and rotating $150 M_{\odot}$ model with solar, LMC and SMC metallicities in terms of age. The blue zones represent the convective regions.	68
4.10	Kippenhahn diagrams for non-rotating and and rotating $150 M_{\odot}$ model with solar, LMC and SMC metallicities in terms of time before core collapse. The blue zones represent the convective regions.	69
4.11	Final mass of 120, 150, 200, 300 and $500 M_{\odot}$ for solar, LMC and SMC metallicities for both rotating and non-rotating models.	70
4.12	Mass of carbon-oxygen core of 120, 150, 200, 300 and $500 M_{\odot}$ for solar, LMC and SMC metallicities for both rotating and non-rotating models. The shaded area represents the range when the final mass of the models will end up as PCSN.	72
4.13	Mass of total helium envelope (left) and the mass fraction of He at the surface (right).	74
4.14	Comparison of Yoshida & Umeda (2011) $140 M_{\odot}$ with our $150 M_{\odot}$ with LMC non-rotating and SMC rotating and non-rotating models. Left panel: The HR diagrams of our models and Yoshida & Umeda (2011). The square, circle and triangles symbol represent the entrance of WR phase. Right panel: Comparison of the evolution of mass loss.	76
4.15	Fate comparison of final mass (left) and mass of carbon-oxygen core (right) Yoshida & Umeda (2011) with our models.	77
4.16	Fate comparison of He surface mass fraction (left) and total He mass envelope (right) Yoshida & Umeda (2011) with our models.	78
4.17	Fate comparison of Yoshida & Umeda (2011) with our models.	79
4.18	Estimated final mass for Case A and Case B at the upper panel. Lower panel shows the final mass from our full stellar models.	85

5.1	Feynman diagram of pair-annihilation neutrino process where G_F is the Fermi coupling constant.	91
5.2	Feynman diagram of photo neutrino process.	92
5.3	Feynman diagram of plasma neutrino process.	93
5.4	HR diagram of 20, 60 and 120 M_\odot models.	97
5.5	T_c - ρ_c diagrams of 20, 60 and 120 M_\odot models. The solid lines represent models with updated neutrino loss while the dotted lines represent models using the old neutrino loss prescription.	98
5.6	Comparison of neutrino energy loss and nuclear energy generation for the 20 M_\odot models at the start of C-burning. Solid lines represent data from models using Itoh et al. (1996) while dotted lines are from models using Itoh et al. (1989)	99
5.7	Neutrino energy loss for 20 M_\odot models at start of the C-, Ne and O-burning. Solid lines represent data from models using Itoh et al. (1996) while dotted lines are from models using Itoh et al. (1989)	100
5.8	Neutrino energy loss for 20 M_\odot models at the start of C-burning in terms of temperature (left) and density (right). Solid lines represent data from models using Itoh et al. (1996) while dotted lines are for models using Itoh et al. (1989)	102
5.9	Neutrino energy loss for 20 M_\odot models at start of C-, Ne and O-burning. Solid lines represent models using Itoh et al. (1996) while dotted lines represent model using Itoh et al. (1989).	103
5.10	Neutrino energy loss for 60 M_\odot models at start of C-burning, Ne-burning and O-burning. Solid lines represent models using Itoh et al. (1996) while dotted lines represent model using Itoh et al. (1989).	104

5.11	Neutrino energy loss for $120 M_{\odot}$ models at start of C-burning, Ne-burning and O-burning. Solid lines represent models using Itoh et al. (1996) while dotted lines represent model using Itoh et al. (1989).	105
5.12	Kippenhahn diagrams of $20 M_{\odot}$ models using Itoh et al. (1996) (N020z14S000) and models using Itoh et al. (1989) (G020z14S000).	106
5.13	Kippenhahn diagrams of $60 M_{\odot}$ models using Itoh et al. (1996) (N060z14S000) and models using Itoh et al. (1989) (G060z14S000).	107
5.14	Kippenhahn diagrams of $120 M_{\odot}$ models using Itoh et al. (1996) (N120z14S000) and models using Itoh et al. (1989) (G120z14S000).	107
6.1	Coulomb barrier where r_N is the nuclear radius when the net charge is at the center of the nucleus and r_c is the position of the incoming particle. .	111
6.2	Comparison of exact probability and standard probability for $^{12}\text{C}(p,\gamma)^{13}\text{N}$.	113
6.3	S-factor of $^3\text{He}(^3\text{He},2p)^4\text{He}$ reaction.	114
6.4	S-factor of $^3\text{He}(\alpha,\gamma)^7\text{Be}$ reaction.	115
6.5	S-factor for $^{12}\text{C}(p,\gamma)^{13}\text{N}$ reaction.	116
6.6	S-factor for $^{15}\text{N}(p,\gamma)^{16}\text{O}$ reaction.	117
6.7	S-factor for $^{16}\text{O}(p,\gamma)^{17}\text{F}$ reaction.	118
6.8	The effective energy derived from the exact probability in comparison with the effective energy using the standard probability for $^{12}\text{C}(p,\gamma)^{13}\text{N}$ reaction.	120
6.9	The reaction rate ratio of $^3\text{He}(^3\text{He},2p)^4\text{He}$ compared to NACRE.	121
6.10	The reaction rate ratio of $^3\text{He}(\alpha,\gamma)^7\text{Be}$ compared to NACRE.	122
6.11	The reaction rate ratio of $^{12}\text{C}(p,\gamma)^{13}\text{N}$ compared to NACRE.	122
6.12	The reaction rate ratio of $^{15}\text{N}(p,\gamma)^{16}\text{O}$ compared to NACRE.	123
6.13	The reaction rate of $^{16}\text{O}(p,\gamma)^{17}\text{F}$ compared to NACRE.	123
6.14	HR diagrams of $20 M_{\odot}$ rotating and non-rotating models with comparison to models using standard nuclear reaction rates.	126

6.15	HR diagrams of $120 M_{\odot}$ rotating and non-rotating models with comparison to models using standard nuclear reaction rates.	127
6.16	Kippenhahn diagrams of $20 M_{\odot}$ rotating and non-rotating models with comparison to models using standard nuclear reaction rates. The models with updated reaction rates are on the left panels and models using standard rates are on the right panels.	128
6.17	Kippenhahn diagrams of $120 M_{\odot}$ rotating and non-rotating models with comparison to models used standard nuclear reaction rates. The models with updated reaction rates are on the left panels and models using standard rates are on the right panels.	129
6.18	Surface abundances of $20 M_{\odot}$ solar metallicity for non-rotating model (upper panel) and rotating models (lower panel). Our models, A020z14z000 and A020z14z400 are compared with models using the standard nuclear reaction rates, G020z14S000 and G020z12S400.	131
6.19	Surface abundances of $120 M_{\odot}$ solar metallicity for non-rotating model (upper panel) and rotating models (lower panel). Our models, A020z14z000 and A020z14z400 are compared with models using the standard nuclear reaction rates, G120z14S000 and G120z12S400.	132
6.20	Evolution of ^{12}C , ^{14}N and ^{16}O central abundances of $20 M_{\odot}$ non-rotating models.	135
6.21	Evolution of ^{12}C , ^{14}N and ^{16}O central abundances of $20 M_{\odot}$ rotating models.	135
6.22	Evolution of ^{12}C , ^{14}N and ^{16}O central abundances of $120 M_{\odot}$ non-rotating models.	136
6.23	Evolution of ^{12}C , ^{14}N and ^{16}O central abundances of $120 M_{\odot}$ rotating models.	136

List of Tables

2.1	Table of a_{ij} coefficients for fitting in the mass loss prescriptions in de Jager et al. (1988) for Eq. 2.24.	24
2.2	Values of x_1 and x_2 used in the metallicity scaling relation for the mass loss rate of WR stars.	26
3.1	Physical Properties of NGC 3603 WN6h stars.	39
3.2	Physical Properties of R136 WN5h stars.	42
4.1	Final evolution of the stars depending on their initial mass at ($Z \equiv 0$) (Heger et al., 2003; Woosley et al., 2007).	44
4.2	Hydrogen (X), helium (Y) and metal (Z) mass fractions for the chemical abundances in our models.	53
4.3	Key properties of stellar models at the end of H-burning phase. The mass are in solar mass, $\Gamma_{\text{Edd}_{\text{init}}}$ is the initial Eddington factor, the lifetimes are in 10^6 years, the main sequence velocity are in km s^{-1} and the abundances are mass fraction abundances.	56
4.4	Key properties of stellar models at the end of He-burning. The mass is in solar mass, the lifetimes in 10^6 years, equatorial velocity $\langle v_{eq} \rangle$ are in km s^{-1} and the surface abundances are mass fraction abundances.	57

4.5	Key properties at the end of the stellar models. The mass are in solar mass, the lifetimes are in million years equatorial velocity $\langle v_{eq} \rangle$ are in km s ¹ and the abundances in mass fraction.	58
4.6	Mass range of initial mass, total He envelope, mass of carbon-oxygen core, final mass and the final fate.	73
4.7	Total mass estimates of the models using different mass loss rates. The table is divided into 5 parts: Total mass of the models at various stages of WR phase, Case A and Case B. In each case, we provide the mass loss rate and the final mass. The unit for $\langle \dot{M} \rangle$ is in M_{\odot} /year and $\langle M_f \rangle$ is M_{\odot}	86
6.1	Table of $\langle \sigma v \rangle$ at temperatures relevant to H-burning, $\log_{10} T = 7$ and $\log_{10} T = 8$. The unit for these values is cm ³ mol ⁻¹ s ⁻¹	121
6.2	Properties of the stellar models at the end of H- and He- burning phases. We compare our models with models using the standard reaction rates.	133

Chapter 1

Introduction

In this chapter we present the framework of this thesis. The relevance of very massive stars is highlighted. The key ingredients that are important in very massive stars, i.e. mass loss and rotation are introduced in this chapter. Finally, the objectives and the outline of this thesis are presented.

1.1 The life of very massive stars

Simulations of the collapse of primordial molecular clouds suggest that the first generation stars or Population III (Pop III) stars which have zero metallicity ($Z = 0$) (Ostriker & Gnedin, 1996) contain many extremely massive members, from 100 up to 1000 M_{\odot} (see for e.g. Bromm et al., 1999; Abel et al., 2000).

Stars with initial mass $\sim 140 - 260 M_{\odot}$ with zero metallicity are thought to end up as pair creation supernovae (PCSNe) or pair instability supernovae (PISNe) and explode completely without leaving any remnants (Barkat et al., 1967; Rakavy & Shaviv, 1967; Bond et al., 1984; Langer & El Eid, 1986; Umeda & Nomoto, 2002; Heger & Woosley, 2002; Woosley et al., 2007; Moriya et al., 2010). This type of stars experiences very small or almost zero mass loss. For massive objects larger than 260 M_{\odot} at the same metallicity

are thought to collapse directly to black holes without any association with supernova (Heger & Woosley, 2002).

PCSN refers to stars where their carbon-oxygen core becomes dynamically unstable during the oxygen-burning stage due to the creation of electron-positron pairs. As the internal energy is spent by the pair creations, the core loses its stability and starts to collapse. Fig. 1.1 shows the evolutionary tracks from Langer et al. (2007) for $250 M_{\odot}$ with extremely low metallicity, $Z = Z_{\odot}/20$ entering the instability region, $\Gamma < 4/3$.

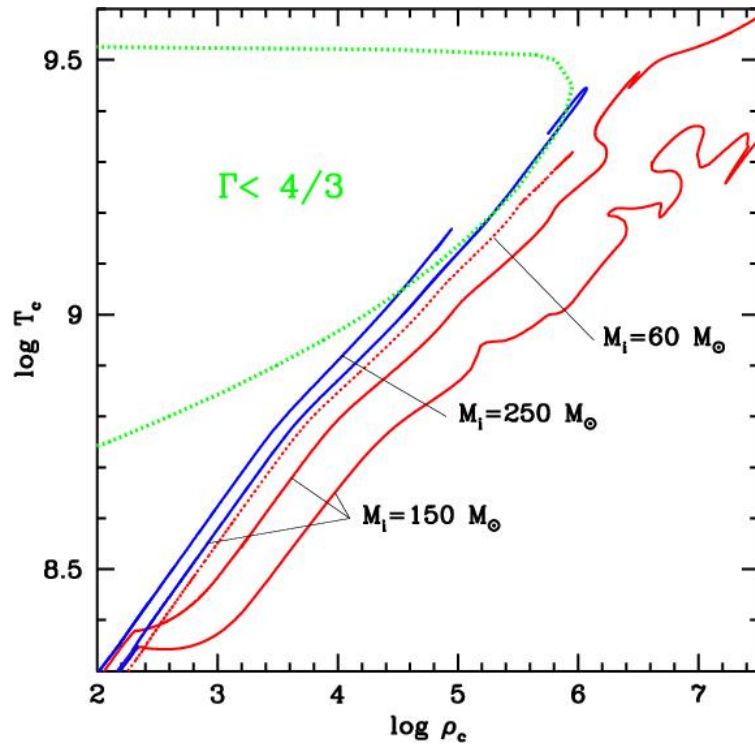


Figure 1.1: Evolutionary tracks from Langer et al. (2007) in the $\log T_c - \rho_c$ diagram. The instability region is indicated as $\Gamma < 4/3$. Shown in blue is the slowly rotating $150 M_{\odot}$ model at $Z = Z_{\odot}/20$, and the $250 M_{\odot}$ model at $Z = Z_{\odot}/20$ entering the instability region.

Numerous work on progenitor of PCSNe are based on stars of Population III (Bond et al., 1984; Heger & Woosley, 2002; Langer et al., 2007; Yungelson et al., 2008; Ekström et al., 2008; Ohkubo et al., 2009; Langer, 2009). Population III contains metal free stars with mass range from $\sim 10^2$ to $\sim 10^5 M_{\odot}$. These stars have enough mass to produce

PCSNe.

The energy predicted in an explosion of PCSNe is $\sim 10^{53}$ erg for most massive stars (Heger & Woosley, 2002). The light curves of the most massive PCSNe are then expected to be very luminous, between $10^{43} - 10^{44}$ erg s^{-1} and long lasting (~ 300 days). PCSNe also have a distinct chemical signature, they produce a lot of iron but this chemical signature is not observed in the extremely metal-poor star (EMP) (Nomoto et al., 2003) therefore bringing question into the existence of PCSNe.

In 2009, Gal-Yam et al. observed the first candidate for the pair creation supernova, SN2007bi. They observed a luminous, slowly evolving object located within a dwarf galaxy. Their spectroscopic analysis shows the supernova contains no traces of helium, thus classified them as SN Ic. It also shows no interaction of any circumstellar material during the event. Gal-Yam et al. (2009) estimated the exploding core mass with the theoretical light curve of PCSNe models (Heger & Woosley, 2002; Kasen et al., 2008) and the result gives the progenitor models of PCSNe to be $\sim 100 M_{\odot}$. This observation leads the support for the existence of PCSNe.

1.1.1 Observations and mass determination of very massive stars

Observations of massive stars have been done extensively in near and far galaxies. Observations of massive stars are limited to the surface properties of the stars: surface abundance, effective temperature and luminosity. These three main properties are deduced either from photometry or spectroscopy analyses from the observed stars. These observational properties can be compared with theoretical stellar models and can provide a good constraint for stellar models. In 2010, we have successfully determined the mass of the most massive star known to date in the Tarantula Nebula (R136a1) with mass at birth $\sim 320 M_{\odot}$. This finding exceeds the upper limit of very massive stars set by Figer (2005) which is around $150 M_{\odot}$. The comparison of R136a1 with red, yellow and blue

dwarfs is illustrated in Fig. 1.2. Details in determining the very massive star mass using stellar evolution models are discussed in Chapter 3.

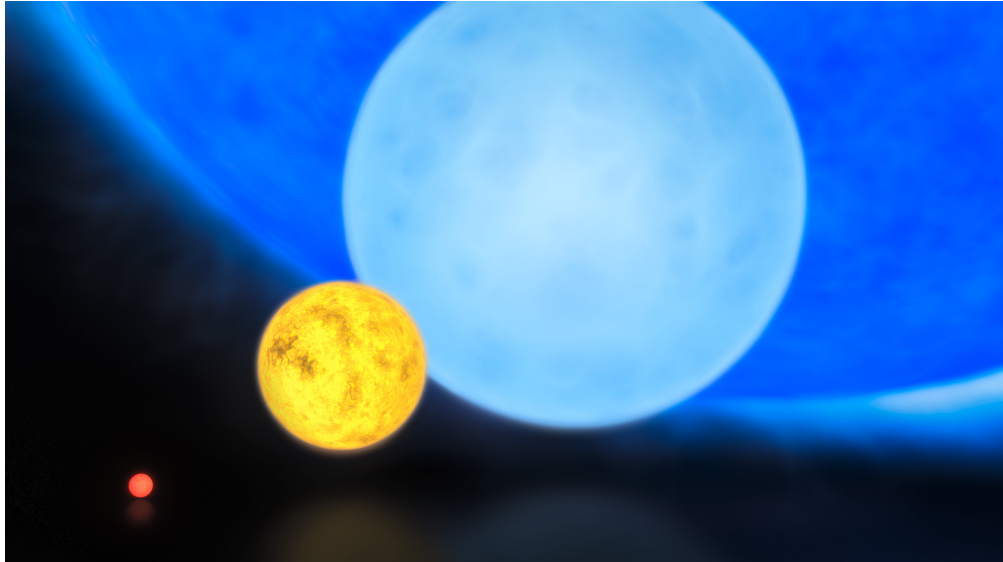


Figure 1.2: Artist's illustration of R136a1 (credit to European South Observatory).

1.2 Physics of massive stars

The two important effects in the evolution of massive stars (or more accurately very massive stars for this work) are mass loss and rotational mixing. Very massive stars have a large temperature-density ratio, T/ρ ratio and it affects the ratio of radiation over gas pressure thus enhances the stellar winds. This ratio also affects the mixing through rotation of the star since the shear turbulence is scaled in terms of thermal diffusivity, $K = 4acT^3/(3C_p\kappa\rho^2)$.

1.2.1 Mass loss

One of the important input for stellar evolution is mass loss. Stars lose mass at all evolutionary phases including during the main sequence. Mass loss rate varies over very

wide range depending on the initial mass of the star. Lower mass stars have very low mass loss rate compared to massive stars. For example, the mass loss rate of the Sun is $\sim 10^{-14} M_{\odot} \text{ yr}^{-1}$ which will amount to $\approx 10^{-5}$ of the solar mass during the main sequence.

Mass loss plays an important role in characterizing the fate of massive stars. It is important to map the specific mass loss process during the various stages of evolution of the massive stars, since the mass loss influences the evolutionary tracks and its fate (see e.g. Meynet et al., 1994; Heger & Woosley, 2002). The effects of mass loss on the evolutionary tracks are at least two-fold: first and foremost the stellar mass is reduced, and secondly, the rotational velocity is strongly affected, as the mass also carries away angular momentum (e.g. Maeder & Meynet, 2000).

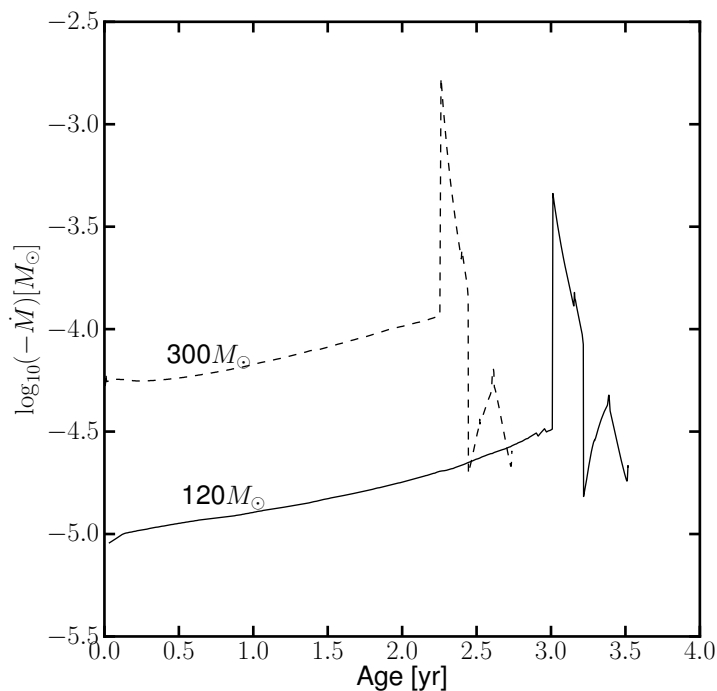


Figure 1.3: Mass loss rates of rotating 120 M_{\odot} and 300 M_{\odot} models with solar metallicity ($Z = 0.014$).

Mass loss is a complex process which involves several mechanisms. Several theories were developed to explain how the particles of matter are lost from the stellar surface and

how they are accelerated up to their terminal velocity. For example, amongst the theories proposed are coronal wind theory, the dust driven wind theory and the line driven wind theory to name a few.

The main process operating on the surface of hot massive stars is the line driven wind. Mass loss from the stellar winds is driven by the strong radiation pressure of very luminous stars which pushes the mass towards the surface. The main transfer of momentum is due to the absorption of stellar radiation by atomic lines. The study of this particular subject for both theoretical and observational has been done for many decades (Lucy & Solomon, 1970; Castor et al., 1975; de Koter et al., 1997; Vink et al., 1999; Nugis & Lamers, 2000; Vink et al., 2001; Mokiem et al., 2007). Recently, a new mass loss prescription has been proposed by Vink et al. (2011) for very massive stars up to $300 M_{\odot}$.

Mass loss rates in very massive stars for example $120 M_{\odot}$ with solar metallicity is around $\log_{10}(-3.35) M_{\odot} \text{ yr}^{-1}$ which leads to a final mass $\sim 18 M_{\odot}$. As we go to the higher initial mass, the mass loss rate also increases. In our $300 M_{\odot}$ solar metallicity models, we find that the mass loss rate can be as high as $\log_{10}(-2.8) M_{\odot} \text{ yr}^{-1}$. The mass loss rates for these two initial masses are shown in Fig. 1.3

1.2.2 Rotation

Rotation is also another important input because it influences the lifetimes, evolutionary tracks, abundances, chemical yields and the fate of the stars. It also enhances the mass loss for very massive stars. O-type stars that are used in this work, have high rotational velocities, v . Fig. 1.4 shows the distribution of v for 496 OB-type stars (Huang & Gies, 2006) where the average velocity is 190 km s^{-1} after correction for the projection angle $\sin i$. In our work, we calculate the rotating models that produce an average velocity which corresponds to the average velocity determined by observations. A summary of the

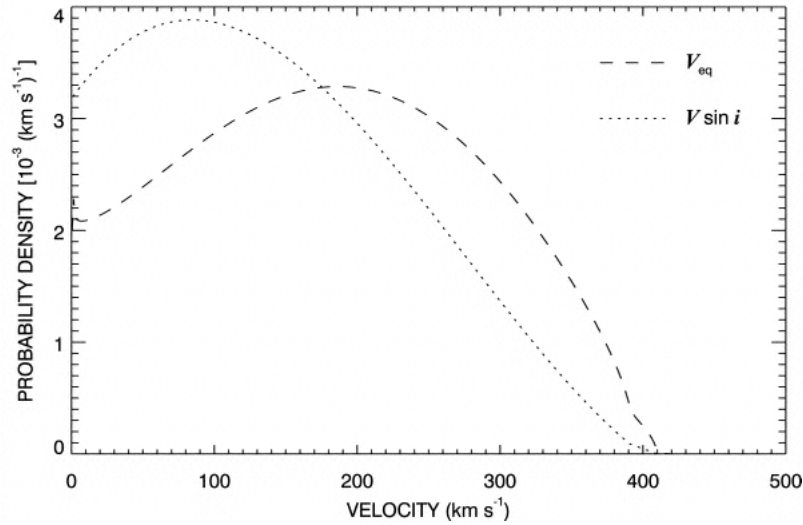


Figure 1.4: Probability density in km s^{-1} of rotation velocity for 496 stars with O9.5 to B8 (Huang & Gies, 2006).

physics of rotation used in the stellar evolution code for this work is discussed in Chapter 2.

1.2.3 Neutrino energy loss

In the evolution of stars, there are six major burning stages: hydrogen burning, helium burning, carbon burning, neon burning, oxygen burning and silicon burning. During H and He-burnings, the star loses its energy by radiation while during the remaining four stages, neutrinos dominate the energy loss. Thus, the neutrino cooling rate is important especially during the late stages of the evolution of the star since most of the energy loss is through the neutrino processes. When the star evolves, the temperature and density increase with time; the rate of neutrino energy loss becomes higher since the neutrino processes depend on the temperature and density of the interior of the star. Major work in neutrino energy loss that are suitable for the application in a stellar evolution code have been done extensively by Itoh and his collaborators (Itoh & Kohyama, 1983; Itoh et al., 1984; Munakata et al., 1985, 1987; Itoh et al., 1989, 1992, 1993; Kohyama et al.,

1993, 1994; Itoh et al., 1989, 1996).

1.2.4 Nuclear reaction rates

The most important process in stellar evolution and nucleosynthesis is the thermonuclear fusion. Light nuclei fuse into heavier nuclei and produce photons which serve as the interior source of energy radiated from the surface. For massive stars, 90% of their life is spent on burning hydrogen and the rest burning helium. In order to calculate the reaction rates, we must have at our disposal the cross section data of the interacting particles involved in the nuclear network at temperatures and densities found in stellar interior. NACRE compilation of reaction rates is by far the commonly used rates in most stellar evolution codes.

1.3 Summary

We have described the life of very massive stars and the key ingredients that are important in the evolution of very massive stars. Since the most massive stars have been observed in R136 star cluster (R136a1) with the potential to end as PCSNe, the goal of this thesis is to study the evolution of very massive stars observed in the Magellanic Clouds. In this thesis, we study the impact of mass loss and its metallicity dependence on the fate of the stars.

1.4 Overview of the thesis

In this section, an overview of this thesis is described. Chapter 2 discusses the stellar evolution models that are used in this work. This includes the physical ingredients and the treatment of rotation and mass loss used in computing the stellar models of very massive stars.

In Chapter 3, the mass determination of very massive stars using the main sequence models is compared with the surface properties from Very Large Telescope observation of NGC3603 and R136 star clusters. This work has successfully determine the mass of the most massive star known to date, the R136a1 with mass at birth around $320 M_{\odot}$. This work has gained extremely wide interest in the astronomy and astrophysics communities.

In Chapter 4, the discussion involves the life and death of very massive stars. Grid of 120 to $500 M_{\odot}$ models with both rotation and non-rotation are presented here. It is the continuation of the work in Chapter 3, where we evolve the models further up to at least at the end of He-burning. We discuss the possibility of our models would end up as PCSN by analyzing the mass of carbon-oxygen core at the final models. For the impact of different mass loss prescriptions, we find that the star might end up as PCSN even at solar metallicity. The details of this work are discussed in Sect. 4.11. In this chapter also we estimate the initial mass of the progenitor of SN2007bi, the candidate of PCSN. Finally we compare our result with Yoshida & Umeda (2011).

In Chapter 5, we update the neutrino energy loss in the Geneva stellar evolution code. In this code, the neutrino energy loss used is from Itoh et al. (1989) and we update it using Itoh et al. (1996). The result of the evolution is presented in this chapter.

In Chapter 6, we implement an improved nuclear reaction rate using the full solution of WKB method in several reactions in the pp chain and CNO burning. For the CNO burning, we find that the new rates give some effects in the N/C surface abundances. In this work, we only evolve 20 and $120 M_{\odot}$ in order to see its affects on different initial mass of the massive stars.

Finally, in Chapter 7, we give a summary of our work and future endeavor is also discussed.

Chapter 2

Geneva Stellar Evolution Code

2.1 Introduction

In this chapter, we present the Geneva stellar evolution code (GENEC) that is used in this work. This code originated back in 1967 (Kippenhahn et al., 1967) and it has gone through major improvements in the 1990's, during which the physics of rotation has been included. It is used to calculate the evolution of massive stars until the pre-supernova stage. It is also able to calculate low-mass stars including solar-type stars and also the Sun. Grids of stellar models of various masses and metallicities have been published and used extensively by the astrophysics community (see Maeder & Meynet (1994); Hirschi et al. (2004); Ekström et al. (2008) for example). This code includes physics of rotation, which successfully reproduces the properties in the observed stars.

This code written in FORTRAN language has evolved through time and been updated continuously with the most updated physics available. An interesting note about this code is that some descriptions are written in German, French and English. It is a very challenging task to understand and use this code for a novice. Since its interception in 1967, the simple stellar evolution code has evolved to become a very complex code and thus it is difficult to discuss it in detail.

In this chapter, we shall discuss about the stellar evolution equations used in this code, followed by the basic physics ingredient used and finally the description of the physics of rotation.

In Geneva stellar evolution code, the model of a star is divided into three main zones: atmosphere, the envelope and the interior. The summary of these zones is given in the text below.

The atmosphere

In this zone, we assume the gravity and opacity are constant. The integration variable is the optical depth, τ defined as $d\tau \equiv -\kappa\rho dr$. The hydrostatic equilibrium equation is solved from pressure, $P=0$, down to an optical depth $\tau = \frac{2}{3}$, where the temperature is by definition the effective temperature of the star. All the boundary conditions are thus known at that optical depth: luminosity L , the effective temperature T_{eff} , the pressure P and radius, R . Details of the atmosphere zones can be found in Maeder (2009).

The envelope

The envelope spreads from the bottom of the atmosphere, down to a given mass fraction of the star, called the fitting mass, FITM. In the envelope, we suppose that there is no energy production by nuclear reactions. The three remaining structure equations are integrated down to FITM. Partial ionisation is accounted for, and the convection is treated non-adiabatically. If the rotation is accounted for, we assume the envelope rotates at constant angular velocity, equal to the angular velocity of the first layer of the interior. The transport of angular momentum equation is not applied in this part of the star but the code ensures that the total angular momentum of the star is considered. To ensure a better follow-up of the rotation, FITM is set to 0.9999 for rotation and for non-rotating case FITM is set to 0.98.

The interior

This part is the main structure of the star, fully ionised, when energy generation occurs by nuclear reactions and where the effects of rotation are carefully accounted for. The medium is suppose to be fully ionised and the convection adiabatic. The full set of structure equations are solved here. The numerical method used is a relaxation method which in the implementation for stellar physics was described by Henyey et al. (1964).

2.2 Stellar structure equations and its physical ingredients

Standard stellar structure codes are governed by four nonlinear equations in order to describe the structure of the star: conservations of mass and energy, momentum and the energy transport equations. On top of these equations, the chemical elements evolution are to be followed. The structure equations and the evolution of chemical abundances are calculated in split mode from each other in the Geneva code in one dimension as in the original version (Kippenhahn et al., 1967).

The system of equations governing the stellar structure comprises a set of four non-linear partial differential equations with four unknowns; mass $M(r)$, pressure $P(r)$, luminosity $L(r)$ and temperature, $T(r)$ where r is the stellar radius with boundary conditions to be satisfied at the center and the surface. These equations are:

1. Mass density relation:

$$\frac{dM}{dr} = 4\pi r^2 \rho \quad (2.1)$$

where ρ is the density.

2. Hydrostatic equilibrium:

$$\frac{dP}{dr} = -\rho \frac{GM}{r^2} \quad (2.2)$$

where G is the gravitational constant.

3. Radial luminosity profile where the luminosity of the star is produced by nuclear burning in a shell radius r and thickness dr :

$$\frac{dL}{dr} = 4\pi r^2 \rho \left[\epsilon_N - T \frac{dS}{dt} \right] - \epsilon_\nu \quad (2.3)$$

where $\epsilon_N(r)$ is the energy production rate per unit volume, $\epsilon_\nu(r)$ is the energy loss by neutrinos, S is the entropy and t is the time. The nuclear energy can be determined by considering all nuclear reaction rates at a given temperature and density.

4. Equation for radiative energy transport :

$$\frac{dT}{dr} = - \frac{3}{4ac} \frac{\kappa \rho L(r)}{T^3 4\pi r^2} \quad (2.4)$$

where κ is the Rosseland's mean opacity, a is the Stefan-Boltzmann constant and c is the speed of light. For convective transfer

$$\frac{dT}{dr} = \frac{\Gamma_2 - 1}{\Gamma_2} \frac{T}{P} \frac{dP}{dr}. \quad (2.5)$$

Here Γ_2 is the Chandrasekhar's second adiabatic exponent which is

$$\Gamma_2 = \frac{32 - 24\beta - 3\beta^2}{24 - 18\beta - 3\beta^2} \quad (2.6)$$

and $\beta = P/P_g$ where P_g is the total gas pressure.

2.2.1 Rotation

In the Geneva code, the physics of rotation has been developed over the last decade. A review of this development can be found in Maeder & Meynet (2000). Here we present short summaries of the physics of rotation used in the code.

Hydrostatic effects

The main assumption made in Geneva code to treat the effects of rotation is the hypothesis of shellular rotation, i.e. the angular rotation velocity is constant on isobar. This is justified if we suppose that there is a strong horizontal diffusion on the isobar, which stabilizes the angular velocity. This assumption is reasonable since the density gradient in the vertical direction tends to stabilize the matter in that direction, whereas the motions are less restricted horizontally (Zahn 1992; Maeder 2003).

For a star in shellular rotation, the surface of constant ψ is an isobaric surface defined as

$$\psi = \phi - \frac{1}{2}\Omega^2 r^2 \sin^2(\theta) = \text{const} \quad (2.7)$$

where ϕ is the gravitational potential and Ω the mean angular velocity.

According to Kippenhahn & Thomas (1970) and Meynet & Maeder (1997), the structure equations of the star can be expressed with respect to isobaric surfaces with only small changes compared to the standard non-rotating case. The new radial coordinate r_p is defined as:

$$V_p = \frac{4\pi}{3} r_p^3 \quad (2.8)$$

where V_p is the volume surrounded by the isobar labeled by p . The hydrostatic equilibrium can be written as

$$\frac{dP}{dM_p} = -\frac{GM_p}{4\pi r_p^4} f_p. \quad (2.9)$$

The factor f_p is defined as

$$f_p = \frac{4\pi r_p^4}{GM_p S_p} \frac{1}{\langle g_{eff}^{-1} \rangle} \quad (2.10)$$

which takes into account all the effects of rotation. Here S_p is the total surface of the isobar considered and $\langle \rangle$ is an average over the whole surface. When f_p is equal to 1 meaning the star is without rotation, Eq. (2.9) is then the same as in the standard case. Note that in the Geneva code, the mass is used as the independent variable. The transformation of integrations above (using the radius as the independent variable) is done using continuity equations. The continuity equation as a function of the isobar is defined as:

$$\frac{dr_p}{dM_p} = \frac{1}{4\pi r_p^2 \bar{\rho}}. \quad (2.11)$$

Here $\bar{\rho}$ is the mean density between two isobars.

Using the equation of state, it is now possible to define a mean temperature \bar{T} using the pressure P and the density $\bar{\rho}$. With a few more simplifying assumptions (see Meynet & Maeder 1997), the energy conservation equation becomes:

$$\frac{dL_p}{dM_p} = \epsilon_{nuc} - \epsilon_\nu + \epsilon_{grav} \quad (2.12)$$

with ϵ_{nuc} is the nuclear energy production rate, ϵ_ν the energy removed by the neutrinos and ϵ_{grav} the energy rate due to gravitation.

The transport of energy can be rewritten as a function of p ;

$$\frac{d \ln(\bar{T})}{dM_p} = -\frac{GM_p}{4\pi r_p^4} f_p \min \left(\nabla_{ad}, \nabla_{rad} \frac{f_T}{f_p} \right), \quad (2.13)$$

where

$$f_T = \left(\frac{4\pi r_p^2}{S_p} \right)^2 \frac{1}{\langle g_{eff} \rangle \langle g_{eff}^{-1} \rangle}. \quad (2.14)$$

From these structure equations with rotation, we can see these are similar to the

standard structure equations without rotation except the variables are slightly different and some of the equations have additional factors. The numerical scheme to solve these equations is the Henyey method and it can be treated by using one-dimensional code like most stellar evolution codes.

Transport of angular momentum

For shellular rotation and in Lagrangian coordinates, the equation of transport of angular momentum can be written as

$$\rho \frac{\partial}{\partial t} (r^2 \bar{\Omega})_{M_r} = \frac{1}{5r^2} \frac{\partial}{\partial r} (\rho r^2 \bar{\Omega} U_2(r)) + \frac{1}{r^2} \frac{\partial}{\partial r} \left(\rho D_v r^4 \frac{\partial \bar{\Omega}}{\partial r} \right) \quad (2.15)$$

where $\Omega(r)$ is the mean angular velocity at level r , $U(r)$ is the vertical component of meridional circulation velocity and D is the diffusion coefficient due to the sum of various turbulent diffusion processes (convection and shears). The factor $1/5$ comes from the integration in latitude. Note that in case of contraction or expansion of a shell, its angular momentum is conserved. The first term on the right hand side which corresponds to meridional circulation is an advective term. The second term of the right hand side which corresponds to the diffusion processes is a diffusive term. From here we can see that advection and diffusion are different.

The numerical scheme used in the Geneva code to solve the angular momentum transport (Eq. 2.15) is divided into two parts, i.e. advection and diffusion. Each of them is solved separately and alternatively with a time step twice larger. The diffusion equation is simpler and it is solved by an implicit finite difference method. For the advection, it is more difficult to solve. The velocity term, $U(r)$ contains a term of the third order and thus the advection equation is of fourth order which is difficult to solve. In this case, a relaxation method is used as it is done to solve the internal structure equations.

Transport of chemical elements

The transport of chemical elements is identical to Eq. (2.15). The equation of transport for chemical elements is given by:

$$\rho \frac{\partial X_i}{\partial t} + \rho \vec{U} \nabla X_i = \nabla (\rho \overleftrightarrow{D} \nabla X_i) \quad (2.16)$$

where X_i is the mass fraction of the element i , \vec{U} is the velocity field due to the meridional circulation and \overleftrightarrow{D} is the diffusion tensor. However, contrarily to the angular momentum transport equation, the equation can be simplified to a pure diffusion equation (Chaboyer & Zahn, 1992):

$$\rho \frac{\partial \bar{X}_i}{\partial t} = \frac{1}{r^2} \frac{\partial}{\partial r} \left[\rho r^2 (D_v + D_{\text{eff}}) \frac{\partial \bar{X}_i}{\partial r} \right] \quad (2.17)$$

with \bar{X}_i is the mean mass fraction of the element i over the isobar and D_{eff} is the effective diffusion coefficient, which includes the effects of the meridional circulation:

$$D_{\text{eff}} = \frac{(rU_2)^2}{30D_h}. \quad (2.18)$$

We can see that the meridional circulation favors the mixing of chemical elements in the vertical direction while the horizontal turbulence inhibits it.

2.2.2 Nuclear networks

For massive stars, the nuclear reaction networks are important in computing the advanced stages. In massive stars, there are six burning stages, which are hydrogen (H), helium (H), carbon (C), neon (N), oxygen (O) and silicon (Si) burnings. The last four burning stages are also known as the advanced burning stages. In this section, we shall discuss briefly the burning stages occurring in the stars.

Hydrogen burning

During the hydrogen burning, pp chain and CNO cycle tri-cycle are considered by using nuclear rates from NACRE (Angulo et al., 1999). Below are the list of reactions in the pp chain and CNO cycle tri-cycle that are used in this work:

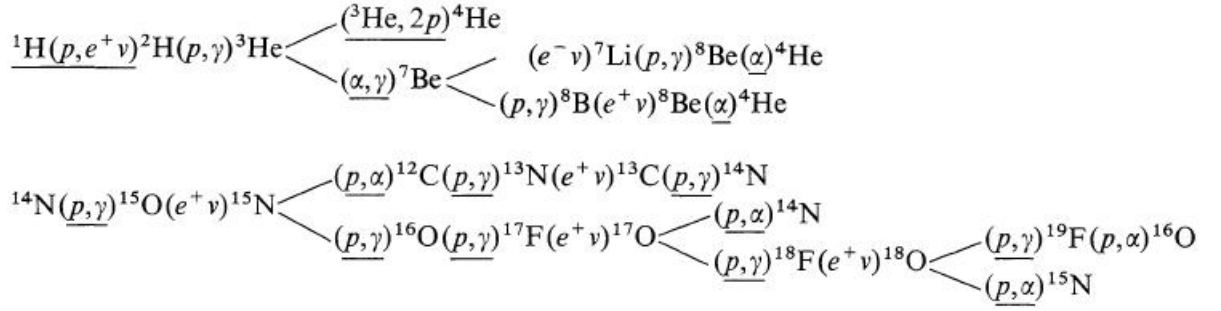


Figure 2.1: The pp chain and CNO tri-cycle diagram. The underline reaction rates are explicitly considered (Maeder, 1983).

Here, the β -decay and ${}^1\text{H}(p, \gamma){}^3\text{He}$ are treated as instantaneous. For the study of massive stars, ${}^7\text{Be}$ and ${}^7\text{Li}$ are not followed but their sum is assumed constant, i.e. $d(X({}^7\text{Be}) + X({}^7\text{Li})/dt = 0)$. The main products for H-burning are ${}^4\text{He}$ and ${}^{14}\text{N}$.

Helium burning

After the H-burning, the most abundant element produced by the star is helium. The following nuclear reactions are considered for helium burning:

- the 3α reaction
- ${}^{12}\text{C}(\alpha, \gamma){}^{16}\text{O}(\alpha, \gamma){}^{20}\text{Ne}(\alpha, \gamma){}^{24}\text{Mg}$
- ${}^{13}\text{C}(\alpha, n){}^{16}\text{O}$
- ${}^{14}\text{N}(\alpha, \gamma){}^{18}\text{F}(\beta, \nu){}^{18}\text{O}(\alpha, \gamma){}^{22}\text{Ne}(\alpha, n){}^{25}\text{Mg}$
- ${}^{17}\text{O}(\alpha, n){}^{20}\text{Ne}$

- $^{22}\text{Ne}(\alpha, \gamma)^{26}\text{Mg}$

The main burning products are ^{12}C , ^{16}O , ^{22}Ne , ^{25}Mg and ^{26}Mg .

Carbon burning

After the He-burning, ^{12}C and ^{16}O are the most abundant elements in the stars. Carbon burning requires central temperature around $\sim 10^9$ K in order to overcome the higher Coulomb barrier. The main thermonuclear reaction process after the He-burning is $^{12}\text{C} + ^{12}\text{C} \rightarrow ^{24}\text{Mg}^*$. Several decay channels are possible for $^{24}\text{Mg}^*$:

- $^{24}\text{Mg} + \gamma$ (Q=13.930 MeV)
- $^{23}\text{Mg} + n$ (Q=-2.605 MeV)
- $^{23}\text{Na} + p$ (Q=2.238 MeV)
- $^{20}\text{Ne} + \alpha$ (Q=4.616 MeV)

Neon burning

Neon burning occurs at the end of C-burning and during this stage, the most abundant elements are ^{20}Ne , ^{24}Mg and ^{23}Na . Even though ^{16}O is also one of the most abundant element produced during He-burning, it is only slightly burnt during C-burning through $^{16}\text{O}(\alpha, \gamma)^{20}\text{Ne}$. The most important reaction in neon burning is $^{20}\text{Ne}(\gamma, \alpha)^{16}\text{O}$ (neon photodisintegration) which takes place when the central temperature, $T_c \simeq 1.2 - 1.3 \times 10^9$ K. The α -particles produce by this reaction are captured by the remaining ^{20}Ne and produces ^{24}Mg through (α, γ) . Most of ^{20}Ne are changed to ^{16}O and ^{24}Mg at the end of Ne-burning stage. Another important reaction for energy generation in this stage is $^{24}\text{Mg}(\alpha, \gamma)^{28}\text{Si}$. Elements produced during this stage are ^{16}O , ^{24}Mg and ^{28}Si .

Oxygen burning

When T_c increases above 2×10^9 K, ^{16}O will start to burn and the O-burning takes place. Interaction between ^{16}O and ^{16}O produces a compound nucleus of $^{32}\text{S}^*$ which decays through the following channels:

- $^{31}\text{Si} + n$ (Q=1.45 MeV)
- $^{31}\text{P} + p$ (Q=7.68 MeV)
- $^{30}\text{P} + d$ (Q=-2.41 MeV)
- $^{28}\text{Si} + \alpha$ (Q=9.59 MeV)

Channels p and α are the most crucial in this stage while channel d can be important at higher central temperature when this endoenergetic channel is open. Other reactions that are important for nucleosynthesis are:

- $^{31}\text{P} = \begin{cases} (\gamma, p)^{30}\text{Si} \\ (p, \gamma)^{32}\text{S} \\ (p, \alpha)^{28}\text{Si}(\alpha, \gamma)^{32}\text{S} \end{cases}$
- $^{28}\text{Si}(\gamma, \alpha)^{24}\text{Mg}(\alpha, p)^{27}\text{Al}(\alpha, p)^{30}\text{Si}$
- $^{32}\text{Si}(n, \gamma)^{33}\text{S}(n, \alpha)^{30}\text{Si}(\alpha, p)^{34}\text{S}$
- $^{28}\text{Si}(n, \gamma)^{29}\text{Si} = \begin{cases} (\alpha, n)^{32}\text{S}(\alpha, p)^{35}\text{Cl} \\ (p, \gamma)^{30}\text{P}(\beta^+)^{30}\text{Si} \\ (n, \gamma)^{30}\text{Si} \end{cases}$
- $^{31}\text{S}(\gamma, p)^{30}\text{P}$
- electron capture:
 - $^{33}\text{S}(e^-, \bar{\nu}_e)^{33}\text{P}(p, n)^{33}\text{S}$
 - $^{35}\text{Cl}(e^-, \bar{\nu}_e)^{35}\text{S}(p, n)^{33}\text{Cl}$

2.2.3 Opacity

Opacity is important in stellar evolution because it determines the energy transport and the radiative gradient, ∇_{rad} . During the evolution, the plasma is fully ionized and the opacity is predominantly due to electron scattering, $\kappa \simeq 0.2(Y_e/0.5)$ (Woosley et al., 2002). In Geneva code, we use opacity tables from the OPAL group (Iglesias & Rogers, 1996) supplemented with low temperature opacities from Ferguson et al. (2005) adapted for the high Ne abundance.

2.2.4 Mass Loss

Mass loss prescriptions used in Geneva code are more focused for hot massive stars which are suitable for this work. There are nine different prescriptions of mass loss that are implemented in the code for various conditions. For this work, we mainly use prescriptions that are suitable to calculate hot massive stars. In this section, all the mass loss prescriptions used in the code are listed and their conditions are described.

Vink et al. (2000, 2001)

Mass loss prescriptions by Vink et al. (2001) are calculated for the stellar winds of massive O and B- type stars as a function of metal abundance, $M = f(Z)$. This method is based on Castor, Abbott and Klein (also known as CAK) theory (Castor et al., 1975) of line-driven winds. This method takes into account the metallicity dependence and the multiple scattering effects. The mass loss rates for massive stars in this method are parameterised as function of wind density $\langle\rho\rangle$, the stellar mass M_\star , luminosity, L_\star , the effective temperature T_{eff} , the metallicity Z and the ratio of terminal flow velocity over the escape velocity v_∞/v_{esc} . This mass loss prescriptions show the existence of bi-stability jump at effective temperature around 25 000 K, 15 000 K and 35 000 K. This existence is due to the ionisation level of iron atoms in the lower part of the winds (Vink et al., 1999).

However, the mass loss prescriptions are divided into two parts, bi-stability around the hot side of $T_{\text{eff}} = 25000$ K and the cool side of this jump. Details of the formulation are given below.

The complete mass loss recipe in this prescription for OB stars is valid for T_{eff} between 50 000 K and 12 000 K and in the range of Z between 1/30 and 3 times Z_{\odot} . The characteristic density $\langle \rho \rangle$ for bi-stability jump around 25 000 K is given by

$$\log \langle \rho \rangle = -14.94(\pm 0.54) + 0.85(\pm 0.10) \log(Z/Z_{\odot}) + 3.2(\pm 2.2)\Gamma_e \quad (2.19)$$

where Γ_e is the luminosity-to-mass ratio. The bi-stability jump is calculated with:

$$\begin{aligned} T_{\text{eff}}^{\text{jump1}} &= 6.12(\pm 4.0) + 2.59(\pm 0.28) \log \langle \rho \rangle \\ T_{\text{eff}}^{\text{jump2}} &= 100 + 6 \log \langle \rho \rangle. \end{aligned} \quad (2.20)$$

The conditions of mass loss in this prescription are based on the effective temperature which are:

1. For the hot side of bi-stability jump $\sim 25\,000$ K or $T_{\text{eff}} > T_{\text{eff}}^{\text{jump1}}$ the mass loss is given by:

$$\begin{aligned} \log \dot{M} &= -6.697(\pm 0.061) + 2.194(\pm 0.021) \log(L_{\star}/10^5) - 1.313(\pm 0.046) \log(M_{\star}/30) \\ &\quad - 1.226(\pm 0.037) \log\left(\frac{v_{\infty}/v_{\text{esc}}}{2.0}\right) + 0.9333(\pm 0.064) \log(T_{\text{eff}}/40000) \\ &\quad - 10.92(\pm 0.90) \log(T_{\text{eff}}/40000)^2 + 0.85(\pm 0.10) \log(Z/Z_{\star}) \end{aligned} \quad (2.21)$$

for $27\,500 < T_{\text{eff}} \leq 50\,000$ K where \dot{M} is in $M_{\odot} \text{ yr}^{-1}$, L_{\star} and M_{\star} are in the solar units and T_{eff} is in Kelvin. In this range, ratio of $v_{\infty}/v_{\text{esc}}$ is 2.6.

2. For the cool side of the bi-stability jump or $T_{\text{eff}}^{\text{jump1}} > T_{\text{eff}} > T_{\text{eff}}^{\text{jump2}}$, the complete

mass loss is:

$$\begin{aligned} \log \dot{M} = & -6.688(\pm 0.080) + 2.210(\pm 0.031) \log(L_*/10^5) - 1.339(\pm 0.068) \log(M_*/30) \\ & - 1.601(\pm 0.055) \log\left(\frac{v_\infty/v_{esc}}{2.0}\right) + 1.07(\pm 0.010) \log(T_{\text{eff}}/20000) \\ & + 0.85(\pm 0.10) \log(Z/Z_*) \end{aligned} \quad (2.22)$$

for $12\,500 < T_{\text{eff}} \leq 22\,500$ K. In this range, ratio of v_∞/v_{esc} is 1.3.

3. If $T_{\text{eff}} < T_{\text{eff}}^{\text{jump}2}$, the mass loss equation is

$$\begin{aligned} \log \dot{M} = & 5.99 + 2.210 \log \log(L_*/10^5) - 1.339 \log(M_*/30) - 1.601 \log\left(\frac{v_\infty/v_{esc}}{2.0}\right) \\ & + 1.07 \log(T_{\text{eff}}/40000) + 0.85 \log(Z/Z_\odot) \end{aligned} \quad (2.23)$$

with ratio of v_∞/v_{esc} is 0.7.

This mass loss prescriptions are applied when the mass of the stars larger is than 15 M_\odot and $\log(T_{\text{eff}})$ greater than 3.9.

de Jager et al. (1998)

The de Jager et al. (1988) prescription covers nearly all Population I stars with spectral line from O to M types stars. This prescription collects mass loss rate for 271 stars which are derived from observable quantities; T_{eff} and L . It covers effective temperature, T_{eff} in the range between $3.3 < \log(T_{\text{eff}}) < 4.8$ and luminosities, L between $2.5 < \log(L/L_\odot) < 6.7$. The mass loss rate from this prescription is given by an analytical expression as the sum of Chebychev polynomials,

$$-\log(\dot{M}) = \sum_{n=0}^N \sum_{i=0, j=n-i}^{n=i} a_{ij} T_i\left(\frac{\log(T_{\text{eff}}) - 4.5}{0.75}\right) \times T_j\left(\frac{\log(L/L_\odot) - 4.6}{0.21}\right) \quad (2.24)$$

with $T_j(x) = \cos(j \arccos(x))$. The coefficients a_{ij} are presented in Table 2.1. In the

Table 2.1: Table of a_{ij} coefficients for fitting in the mass loss prescriptions in de Jager et al. (1988) for Eq. 2.24.

j =	0	1	2	3	4
i = 0	6.34916	-5.04240	-0.83426	-1.13925	-0.12201
1	3.41678	0.15629	2.96244	0.33659	0.57576
2	-1.08683	0.41952	-1.37272	-1.07493	
3	0.13095	-0.09825	0.13025		
4	0.22427	0.46591			
5	0.11968				

code, this prescription is used throughout the whole stellar evolution for mass between $7 M_{\odot}$ and $15 M_{\odot}$, and during the red supergiant (RSG) phase for the more massive ones ($\log T_{\text{eff}} \leq 3.9$).

Gräfener & Hamann (2008)

Gräfener & Hamann (2008) mass loss prescription is computed using Postdam Wolf-Rayet model atmosphere code, which includes non-LTE treatment of the wind, line blanketing and structure of the wind obtained by solving hydrodynamic equations. This prescription takes into account the Fe-line blanketing and clumping effects in the winds. The mass loss rate from this prescription is computed in the domain of effective temperature; $40\,000\text{ K} < T_{\text{eff}} < 70\,000\text{ K}$ and the validity domain in metallicity is restricted to $10^{-3}Z_{\odot} < Z < 2Z_{\odot}$.

This mass loss prescription is a function of stellar parameters; the effective temperature T_{eff} , the luminosity L , surface hydrogen fraction X and the Eddington ratio $\Gamma_{\text{edd}} = L/L_{\text{edd}}$ which is computed with the electron scattering opacity. The mass loss rate is given by:

$$\log \frac{\dot{M}}{M_{\odot} \cdot \text{y}^{-1}} = 3.76 + \beta(Z) \log(\Gamma_{\text{Edd}} - \Gamma_0(Z)) - 3.5(\log(T_{\text{eff}} - 4.65)) \quad (2.25)$$

$$0.42 \left(\log\left(\frac{L}{L_{\odot}}\right) - 6.3 \right) - 0.45(X - 0.4).$$

where $\beta(Z)$ and $\Gamma_0(Z)$ are defined as follows:

$$\beta(Z) = 1.727 + 0.25 \log\left(\frac{Z}{Z_{\odot}}\right) \quad (2.26)$$

$$\Gamma_0(Z) = 0.326 - 0.301 \log\left(\frac{Z}{Z_{\odot}}\right) - 0.045 \log^2\left(\frac{Z}{Z_{\odot}}\right)$$

In Geneva code, this mass loss rate is used for late WN stars with metallicity and effective temperature in the range of allowed values discussed above.

Nugis & Lamers (2000)

In the code, we use Nugis & Lamers (2000) to calculate the mass loss of Wolf-Rayet (WR) stars. Empirical dependence of mass loss rate of WR stars is derived from observed winds of 44 WR stars. The 44 WR star cluster consists of 24 WN stars, 18 WC stars and 2 WO stars. This prescription allows us to determine the mass loss rate for two sub-samples stars which are WN star and WC+WO stars.

For WR subtype determination, the method adopted is the same as in Maeder & Meynet (1994). In the initial original work, the metallicity dependence was not included but it was added later (Eldridge & Vink, 2006). Since WR winds are thought to be mainly driven by line acceleration and the elements which are principally responsible for this dependence are Fe-peak elements, the metallicity used for computing this dependence is not the actual metallicity of the surface Z but the initial metallicity, Z_{ini} . Stellar evolution does not modify the surface abundance of Fe-peak elements, whereas the total

Table 2.2: Values of x_1 and x_2 used in the metallicity scaling relation for the mass loss rate of WR stars.

type	Z_{ini}	x_1	x_2
WN	-	0.85	-
WC	$> Z_{\odot}$	0.4	-
	$0.002 < Z_{ini} < Z_{\odot}$	0.66	-
	< 0.002	0.66	0.35

metallicity Z is increased by mixing process and mass loss which reveals enriched layers of the stellar interior.

The metallicity dependence is accounted for in the following way:

1. for $Z_{ini} > 0.002$:

$$\frac{\dot{M}}{\dot{M}_{\odot}\text{yr}^{-1}} \sim \left(\frac{Z_{ini}}{Z_{\odot}}\right)^{x_1} \quad (2.27)$$

2. for $Z_{ini} < 0.002$:

$$\frac{\dot{M}}{\dot{M}_{\odot}\text{yr}^{-1}} \sim \left(\frac{0.002}{Z_{\odot}}\right)^{x_1} \left(\frac{Z_{ini}}{0.002}\right)^{x_2} \quad (2.28)$$

where the values of x_1 and x_2 are used in the metallicity scaling relation for the mass loss rate of WR stars. Values of x_1 and x_2 are given in Table 2.2.

The mass loss rate for WN star is given by

$$\log \dot{M} = -13.60 + 1.63 \log \left(\frac{L}{L_{\odot}}\right) + 2.22 \log Y + 0.85 \log \left(\frac{Z_{ini}}{Z_{\odot}}\right) \quad (2.29)$$

and for the WC and WO stars, if $Z_{ini} > 0.002$:

$$\log \dot{M} = -8.30 + 0.84 \log \left(\frac{L}{L_{\odot}}\right) + 2.04 \log Y + 1.04 \log Z + x_1 \log \left(\frac{Z_{ini}}{Z_{\odot}}\right) \quad (2.30)$$

if $Z_{ini} < 0.002$:

$$\log \dot{M} = -8.30 + 0.84 \log \left(\frac{L}{L_{\odot}} \right) + 2.04 \log Y + 1.04 \log Z + x_1 \log \left(\frac{0.002}{Z_{\odot}} \right) + x_2 \log \left(\frac{Z_{ini}}{0.002} \right) \quad (2.31)$$

For the use in Geneva stellar evolution code, this prescription is used for the WR stars in the MS which are out of the range of Gräfener & Hamann (2008) prescription and for all the WR stars which are in their He-burning phase.

2.2.5 Equation of State

The equation of state (EOS) for a perfect gas which is totally ionized is simple. The EOS becomes more complex when the gas becomes partially degenerate or partially ionized. This can happen near the surface of the star. In the Geneva evolution code, the equation of state usually used is a general equation of state (see Schaller et al. 1992). The general EOS is perfectly suitable for evolution of massive stars but for the solar-type stars, more specific and realistic EOS is needed. The EOS used for evolution of solar-type stars that are included in the code are: the MHD equation of state (Hummer & Mihalas, 1988; Mihalas et al., 1988; Daeppen et al., 1988) and the OPAL equation of state (Rogers & Iglesias, 1996; Rogers & Nayfonov, 2002).

2.2.6 Convection

In the Geneva code, the stability of a given layer is determined by using the Schwarzschild criterion. A new addition due to Soilberg-Hoiland criterion for convection in the stellar envelope in the Geneva code has been developed by Maeder et al. (2008) which takes rotation into account.

2.2.7 Overshooting

In this code, overshooting is treated using Schwarzschild criterion. The value of overshooting is $d_{over}/H_p = 0.10$ where H_p is the pressure scale height estimated by Schwarzschild boundary.

2.2.8 Neutrino Energy Loss

Most of the energy generated by the nuclear reactions in the central region of the star is carried away by neutrinos during the advanced stages. Neutrinos are produced in weak interactions during the Si-burning but are mainly produced by the following leptonic processes throughout the advanced stages:

- photoneutrino process
- pair neutrino process
- plasmon decay/plasma neutrino
- bremsstrahlung on nuclei
- recombination process

In Geneva code, only the first four processes are included but as an addition to this work, we have updated the neutrino processes in the code and this will be discussed in detail in Chapter 5.

Chapter 3

Main Sequence Phase of Very Massive Stars: Comparison with Observations

3.1 Motivation

Studies in very massive stars are one of the most important areas in modern astrophysics. Although this type of star is relatively small in number in the late-type galaxies, they play a very important role in providing information on their host galaxies and the galaxies themselves. These stars serve as the main source of heating and ionisation of interstellar medium in the galaxies, which determines their evolution. It also provides chemical enrichment in its host galaxy through stellar winds and explosion at the end of their life. In spite of its important role in shaping galactic structure and evolution, the formation of very massive stars is poorly understood.

As discussed earlier in Chapter 1, many theoretical models have been developed and observations have been made to investigate its existence in the past decade. However, many studies of evolution of very massive stars ($> 100 M_{\odot}$) are more focused on the first generation stars (Population III) (see for example Bond et al., 1984, Ekström et al., 2008, Yungelson et al., 2008) because it is thought the first stars in early universe were very



Figure 3.1: A Hubble Space Telescope image of R136 (*left*) and NGC3603 (*right*). In the center of star-forming region 30 Doradus lies a huge cluster of the largest, hottest, most massive stars known as R136 (N. Walborn , STScI). Image of NGC3603 recorded by Hubble’s Advanced Camera for Surveys, the image spans about 17 light-years (NASA, 2007).

massive stars (Bromm et al., 1999). In this work, we calculate main-sequence models for solar, Large Magellanic Cloud (LMC) and Small Magellanic Cloud (SMC) metallicities since very massive stars also exist in the local galaxy and LMC. For very massive star observations, the accepted upper mass limit cut off is around $150 M_{\odot}$ (Massey & Hunter, 1998; Figer, 2005; Weidner & Kroupa, 2006).

The aim of this work is to compare our theoretical models with observational data in order to determine the mass of very massive stars. Evidence supporting the existence of stars more massive than $150 M_{\odot}$ is presented in this chapter where we investigate the effects of rotation, mass loss and metallicity on the evolution of main-sequence phase of the very massive stars. In this work, mass determination of stars in two young star clusters has been done namely R136 and NCG3603. Images of these two star clusters can be found in Fig. 3.1. Stars in these clusters are determined to be more massive than $150 M_{\odot}$.

3.2 Observations

Very massive stars usually exist in young and very bright star clusters. Three of the main star clusters containing these giants are Arches, R136 and NGC3603. Arches and NGC3603 are situated in Milky Way while R136 is situated in the Tarantula nebula (30 Doradus) within Large Margellanic Cloud (LMC).

NGC3603 is a galactic example of young and least evolved star cluster known (Schnurr et al., 2008). It is located about 22,000 light years from our Sun and it provides great detail in the star formation and it is one of the star cluster candidate that contains high mass stars. In NGC3603, three WN 6h systems are known to become the source or candidate of the most massive stars with very high luminosity in excess of $10^6 L_{\odot}$ (de Koter et al., 1997; Crowther & Dessart, 1998).

R136 is a young and massive star cluster in the Local Group of galaxies and has the possibility of containing stars beyond the physical limit of $150 M_{\odot}$. It contains several stars which are classified by the component of "a" and it is believed to be a single star of several thousand of masses (Cassinelli et al., 1981; Savage et al., 1983). This claim has been disproven by speckle interferometric observations (Weigelt & Baier, 1985) and confirmed by Hubble Space Telescope (HST) imaging by Hunter et al. (1995).

Another final candidate known to host very massive stars is Arches cluster. Studies done by Figer (2005) concluded that the mass of stars in this cluster does not exceed $150 M_{\odot}$. Later studies carried out by Martins et al. (2008) confirmed Figer's studies for the brightest stars (late WN) are in the range of $120-150 M_{\odot}$. However, this cluster is not included in this work since the previous studies (Figer, 2005; Martins et al., 2008) has provided the sharp cut-off in the mass limit for this cluster.

The challenge in this work is to use stellar evolution models to verify the mass determination of very massive stars in NGC3603 and R136, which might host stars with mass more than $150 M_{\odot}$. In this work, we determine the mass of very massive stars in R136

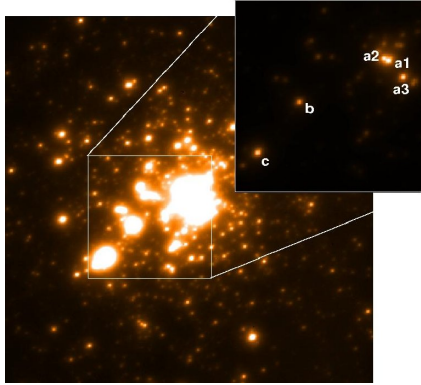


Figure 3.2: VLT MAD K_s -band 12×12 arcsec (3×3 parsec for the LMC distance of 49 kpc) image of R136 (Campbell et al. (2010)) together with a view of the central 4×4 arcsec (1×1 parsec) in which the very massive WN5h stars discussed in this thesis are labeled (component b is a lower mass WN9h star). Relative photometry agrees closely with integral field SINFONI observations (Schnurr et al. 2009).

and NGC3603 star clusters which have been reanalysed recently using spectroscopy data from VLT-FLAMES and HST archive (Crowther et al., 2010). The stars in these two clusters might provide an answer of the possibility that the stars have mass beyond the commonly accepted stellar upper mass limit of $150 M_{\odot}$.

The photometry image of the R136 star cluster discussed in this work is shown in Fig.3.2 using the VLT Multi-Conjugate Adaptive Optics Demonstrator (MAD) imaging. However, we shall not discuss the details of the observation technique since it is beyond the scope of this thesis. In this work, we shall concentrate on the stellar evolution models.

3.3 Main sequence models

For the main sequence model of very massive star, we calculate the evolution of massive stars in the range of $85 M_{\odot}$ to $500 M_{\odot}$. In this work, both non-rotating and rotating models are considered and followed until the end of H-burning. Details of the descriptions of the stellar models are provided in Chapter 2. The study of the post-main sequence star for the same models will be discussed in Chapter 4. The initial metallicities for

these models are set to $Z = 0.006$ (LMC) and 0.014 (solar) (Asplund et al., 2005) which correspond to the metallicity of NGC3603 and R136.

3.3.1 Physics of the models

For our models, we chose the standard mass loss prescription for O-type stars from Vink et al. (2001) for which Mokiem et al. (2007) have provided the empirical evidence. The models enter the Wolf-Rayet (WR) phase when the hydrogen content $X_H < 30\%$ and if the effective temperature, $T_{\text{eff}} \geq 10,000$ K. For the WR phase, we use mass loss prescription from Nugis & Lamers (2000). As the star evolves, the star will lose mass through stellar winds.

We choose a ratio of the initial velocity to critical rotation of $v_{\text{init}}/v_{\text{crit}} = 0.4$ for the rotating models, which corresponds to surface equatorial velocities around 350 km s^{-1} for $85 M_{\odot}$ model and 450 km s^{-1} for the $500 M_{\odot}$ model with the LMC metallicity. The velocity produce from this ratio corresponds to an average velocity of about 220 km s^{-1} on the main sequence (MS) which is closed to the observed average value (see for instance Fukuda, 1982 and Huang & Gies, 2006).

3.3.2 Evolution of the main sequence models

In Fig. 3.3, the evolutionary main sequence models of $120 M_{\odot}$ in the Hertzsprung-Russell diagram is presented. In this figure, we show the rotating and non-rotating models at LMC metallicity and one non-rotating models at solar metallicity. The rotation effect can be seen clearly in the diagram. In the luminosity-temperature plot, the rotating model remains hot longer than the non-rotating model. Additional mixing causes the helium to be mixed out of the core and reduces the opacity in the outer surface of the star. This condition allows the rotating models to stay as high as $45,000$ to $55,000$ K, whereas for the non-rotating model decreases from $20,000$ to $25,000$ K. Thus, we can predict the rapidly

rotating stars will evolve directly to the classical WR phase, whereas the slow rotators are expected to evolve to η Car-like luminous blue variables (see Meynet & Maeder, 2005)

Stars with higher metallicity tend to have lower luminosities (see Langer et al., 2007) due to the additional mixing above the convective core. They are also losing their mass much faster than their low-metallicity star counterpart. This can also be seen in luminosity-temperature plot in Fig. 3.3 for $120 M_{\odot}$ non-rotating model for LMC and solar. The stars with LMC metallicity have higher luminosity compared to stars with solar metallicity.

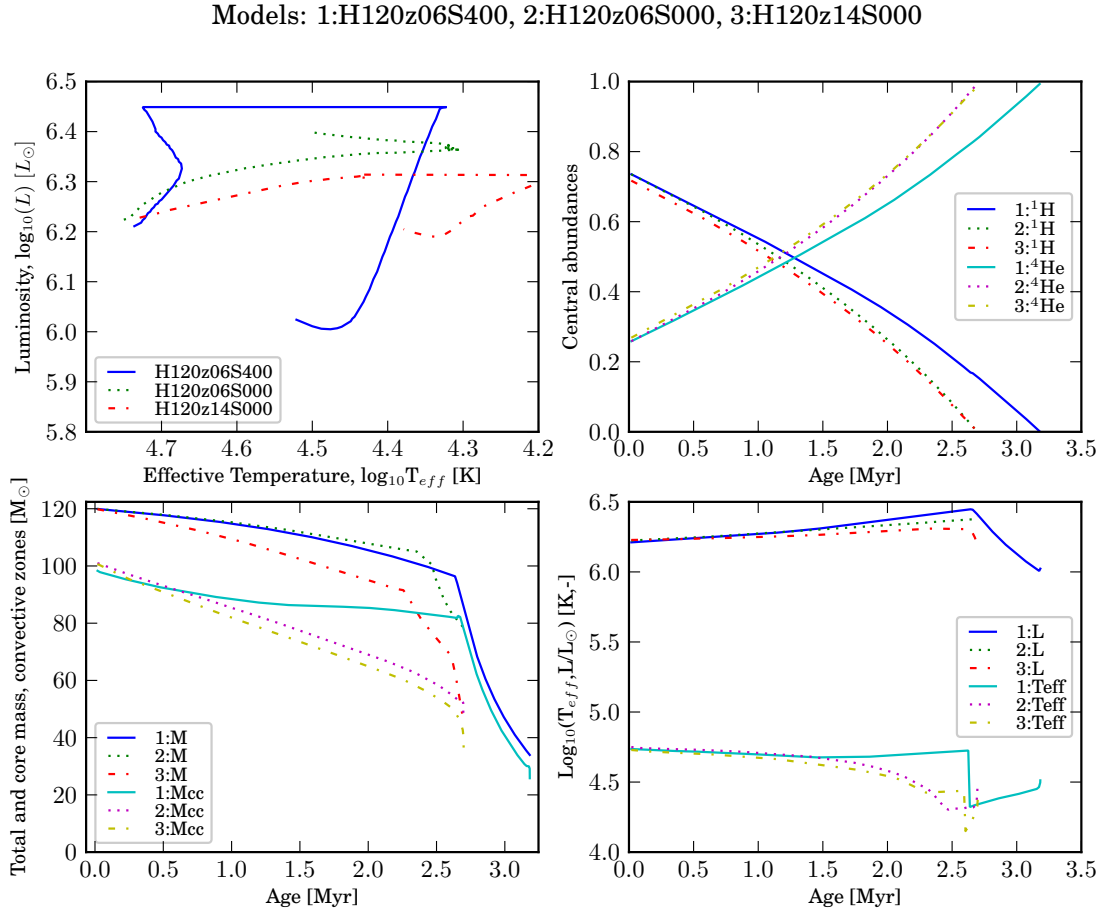


Figure 3.3: Comparison between main sequence evolutionary predictions for both rotating ($Z = 0.006$:H120z06S400) and non-rotating ($Z = 0.006$:H120z06S000, $Z = 0.014$:H120z14S000) $120 M_{\odot}$ models. For model H120z06S400, the horizontal lines in the top left-hand panel correspond to the transition to the WR phase, phase during which the photosphere is in the wind rather than at the surface of the star.

Models: 1:H120z14S000, 2:H120z06S400

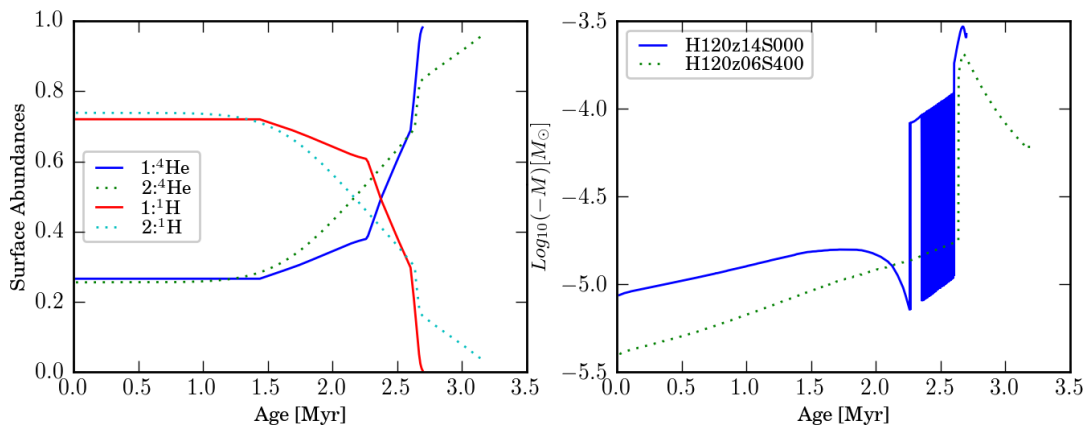


Figure 3.4: Comparison between surface abundances and mass loss rate for both rotating ($Z = 0.006$: H120z06S400) and non-rotating ($Z = 0.006$:H120z06S000, $Z = 0.014$: H120z14S000) $120 M_{\odot}$ models.

The surface abundances and the mass loss rates of these models are plotted in Fig. 3.4. At the end of the main sequence, most of the hydrogen at the surface is depleted. Solar metallicity models suffer the highest depletion rate compared to LMC models. Rotation also enhances depletion of hydrogen at the surface and it can be seen clearly in the diagram where the $120 M_{\odot}$ rotating model at LMC metallicity losses hydrogen layer faster than its non-rotating model.

For the mass loss rate, the non-rotating models suffer from the bi-stability jumps and oscillate from the jump at $T_{\text{eff}} = 25,000$ K to the additional bi-stability jumps around $T_{\text{eff}} = 15,000$ and $35,000$ K (see Fig 3.4 left panel) which are described by Vink et al. (2001) mass loss prescription (see Sect. 2.2.4 for details) At this point, the mass loss increases drastically and it can be seen from Fig. 3.3 (lower left panel) where the models lose mass around 20-50 %. Rotating model in the same diagram does not suffer from the oscillation in the bi-stability jumps. Although the mass loss rate for the solar metallicity models is higher than the LMC metallicity models, the lifetime is longer for the LMC metallicity models. This explains why solar metallicity models lose more mass than the LMC models. Comparing with rotating model and non-rotating model at LMC

metallicity, at age around 2.5 Myr, the non-rotating model has higher mass loss rate than rotating model and at age around 2.7 Myr, the rotating model mass loss rate supersedes the mass loss rate of the non-rotating model. This corresponds to the entrance of the rotating model to the WR phase. At this point, the rotating model sheds its hydrogen surface much stronger than its non-rotating model. From these stellar models, the surface properties: luminosity, T_{eff} and their surface abundances are used to compare with the surface properties of an observed star.

In the next section, we shall discuss the comparison of our models with the observed stars. The results from our models will be used to compare the surface properties of the stars in NGC3603 and R136 clusters.

3.4 Mass determination of the most massive stars

The results from the stellar evolution models are compared with spectroscopic analyses of two young star clusters, i.e. NGC3603 and R136. Details of the spectroscopic analyses can be found in Crowther et al. (2010). In the next subsection, we shall discuss in detail the stellar models used for this purpose and we compare the evolutionary models of solar metallicity with the observational properties of NGC3603 WN R136 stars. In order to compare values from observations and theoretical calculation, we need to know three parameters: surface abundances, effective temperature (T_{eff}) and luminosity (L/L_{\odot}). For this work, we choose the hydrogen surface abundance, X_H for the surface abundance.

3.4.1 Verification of the mass determination : NGC3603

Observational properties of four stars in NGC3603, namely A1a, A1b, C and B are used in the comparison with solar metallicity model. Stars B and C are confirmed binary (Schnurr et al., 2008) whereas A1a and A1b are presumed to be single. For these stars, we compare the observational properties (L/L_{\odot} , T_{eff} , X_H) with solar metallicity models.

The comparison with stellar models and observations is shown in Fig. 3.5. Both rotating and non-rotating models are plotted in Fig. 3.5 in order to compare with the observational properties.

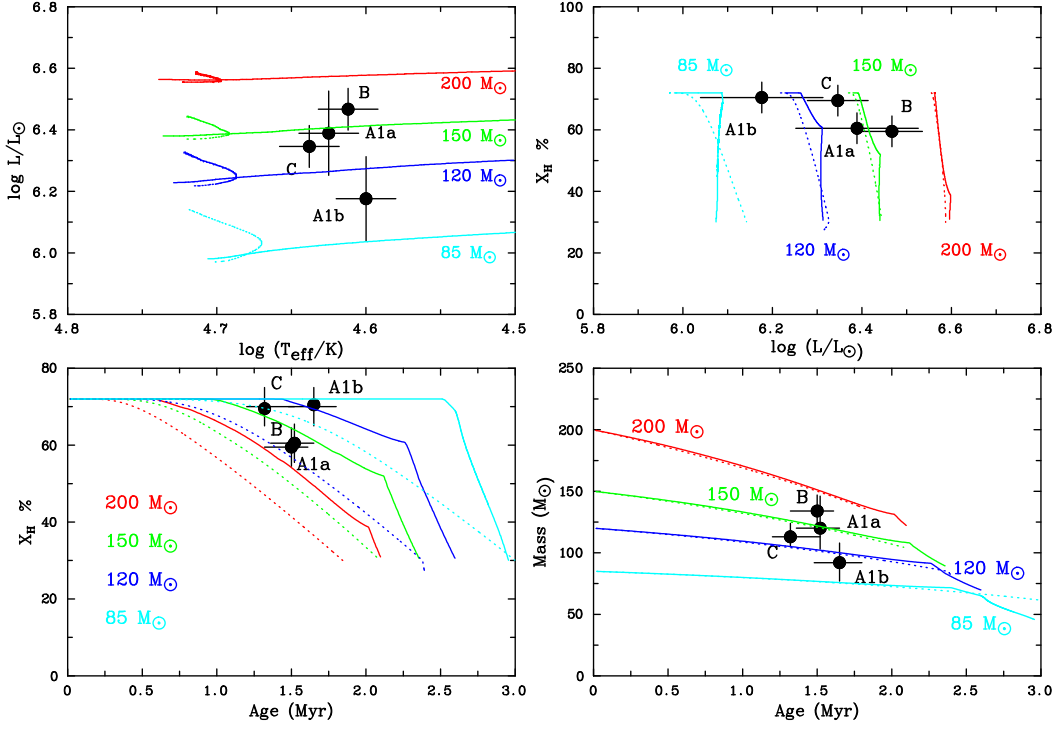


Figure 3.5: Comparison between solar metallicity ($Z = 1.4\%$) models calculated for the main-sequence evolution of 85 - 200 M_{\odot} stars (initially rotating at $V_{\text{init}}/v_{\text{crit}} = 0.4$ [dotted] and 0 [solid]), and the physical properties derived from spectroscopic analysis of NGC 3603 WN6h stars.

From Fig. 3.5, we have plotted the HR diagram (L/L_{\odot} vs T_{eff}), X_H in terms of L/L_{\odot} , X_H in terms of age of the model and finally we determine the mass from the mass vs age of the model plot. From the result, we find that A1a, A1b, C and B lies between around 85-200 M_{\odot} in the HR diagram. Using rough estimate from Fig. 3.5 (upper left panel), A1a lies near to the 150 M_{\odot} model, A1b close to 100 M_{\odot} , B close to 180 M_{\odot} and C close to 140 M_{\odot} . Since spectroscopy can produce hydrogen surface abundance of these stars,

we plot these observed values using X_H in terms of L/L_\odot (upper right panel). A1a gives the closest match with the $150 M_\odot$ grid. When comparing X_H with age, we can estimate the current age of these stars. The current age estimates for these stars are $\sim 1.25 - 1.75$ Myr.

Finally we deduce the mass of the stars with respect to age. Non-rotating models predict the current masses of 120_{-17}^{+26} and $92_{-15}^{+16} M_\odot$ for A1a and A1b respectively at an age of $\sim 1.5 \pm 0.1$ Myr. Independent age estimates using pre-main sequence isochrones of low-mass stars also favour low 1 ± 1 Myr ages (Sung & Bessell, 2004), while Crowther et al. (2006) estimated 1.3 ± 0.3 Myr for NGC3603 from a comparison between massive O stars and theoretical isochrones (Lejeune & Schaerer, 2001).

The initial mass for these two components are suggested to be around $140 M_\odot$ and $106 M_\odot$ respectively. These results give an excellent agreement with dynamical mass determination of 116 ± 31 and $89 \pm 16 M_\odot$ for the primary and secondary A1 components (Schnurr et al., 2008). Current mass-loss rate matches the solar metallicity model predictions (Vink et al., 2001) to within 0.2 dex. Table 3.1 presents the physical properties of NGC3603 WN 6 stars from the observations containing the initial and current stellar mass estimates.

The successful comparison of this known star shows that our method is reliable in determining the mass of very massive stars. We shall use the same treatment here to determine the most massive star in R136 star cluster.

Table 3.1: Physical Properties of NGC 3603 WN6h stars.

Name	A1a	A1b	B	C
T_* (kK) ^a	42 ± 2	40 ± 2	42 ± 2	44 ± 2
$\log(L/L_\odot)$	6.39 ± 0.14	6.18 ± 0.14	6.46 ± 0.07	6.35 ± 0.07
$R_{\tau=2/3}$ (R_\odot)	$29.4^{+10.1}_{-4.3}$	$25.9^{+7.2}_{-3.1}$	$33.8^{+2.7}_{-2.5}$	$26.2^{+2.1}_{-2.0}$
N_{LyC} (10^{50} s^{-1})	$1.6^{+0.8}_{-0.4}$	$0.85^{+0.54}_{-0.23}$	$1.9^{+0.3}_{-0.3}$	$1.5^{+0.3}_{-0.3}$
\dot{M} ($10^{-5} M_\odot \text{ yr}^{-1}$)	$3.2^{+1.2}_{-0.6}$	$1.9^{+0.9}_{-0.4}$	$5.1^{+0.6}_{-0.6}$	$1.9^{+0.2}_{-0.2}$
$\log \dot{M} - \log \dot{M}_{\text{Vink}}^c$	+0.14	+0.24	+0.22	-0.04
V_∞ (km s^{-1})	2600 ± 150	2600 ± 150	2300 ± 150	2600 ± 150
X_H (%)	60 ± 5	70 ± 5	60 ± 5	70 ± 5
M_{init} (M_\odot) ^b	148^{+40}_{-27}	106^{+23}_{-20}	166^{+20}_{-20}	137^{+17}_{-14}
M_{current} (M_\odot) ^b	120^{+26}_{-17}	92^{+16}_{-15}	132^{+13}_{-13}	113^{+11}_{-8}
M_{K_s} (mag) ^d	-7.0 ± 0.3	-6.6 ± 0.3	-7.5 ± 0.1	-6.7 ± 0.1

(a) Corresponds to the radius at a Rosseland optical depth of $\tau_{\text{Ross}} = 10$

(b) Component C is a 8.9 day period SB1 system (Schnurr et al. 2008a)

(c) dM/dt_{Vink} relates to Vink et al. (2001) mass-loss rates for $Z = Z_\odot$

(d) $M_{K_s} = -7.57 \pm 0.12$ mag for A1, for which we adopt $\Delta m = m_{\text{A1a}} - m_{\text{A1b}} = -0.43 \pm 0.30$ mag (Schnurr et al. 2008a). The ratio of their luminosities follows from their dynamical mass ratios together with $L \propto \mu M^{1.5}$ (and is supported by NICMOS photometry from Moffat et al. 2004).

3.4.2 Mass determination of the most massive star: R136a1

From our results for NGC3603, the same method is applied to determine the mass of the stars in R136 cluster. In this cluster, four very massive stars are identified, indicated as R136a1, R136a2, R136a3 and R136c. Since R136 is located within the LMC, we use stellar models with LMC metallicity in order to determine its surface properties.

In Fig. 3.6, comparison between the properties of R136a1, R136a2, R136a3 and R136c with stellar models with LMC metallicities with the assumption that these stars are single although R136c is a probable binary (Schnurr et al., 2009). From the results, we imply the current mass of components a1, a2 and a3 are $265 M_{\odot}$, $195 M_{\odot}$ and $165 M_{\odot}$ respectively at age of 1.7 ± 0.2 Myr with strong rotational rate. Therefore, the initial mass of the largest current mass, component a1 is around $320 M_{\odot}$ which is beyond the suggested upper limit of the star (Figer, 2005). As in NGC3603, we find the the current mass-loss rates match the LMC-metallicity theoretical predictions (Vink et al., 2001) to within 0.2 dex.

The rotation effect will reproduce the observed surface hydrogen content of 30-40 % by mass. The physical properties of the observed R136 stars are shown in Table 3.2 which include the initial and current stellar mass estimates. Differences in age estimates show variations in initial rotation rates. Nevertheless, equatorial rotation rate of $v_e \sim 200$ (300) km s^{-1} is predicted after ~ 1.75 Myr for $300 M_{\odot}$ and 2.75 Myr for $150 M_{\odot}$.

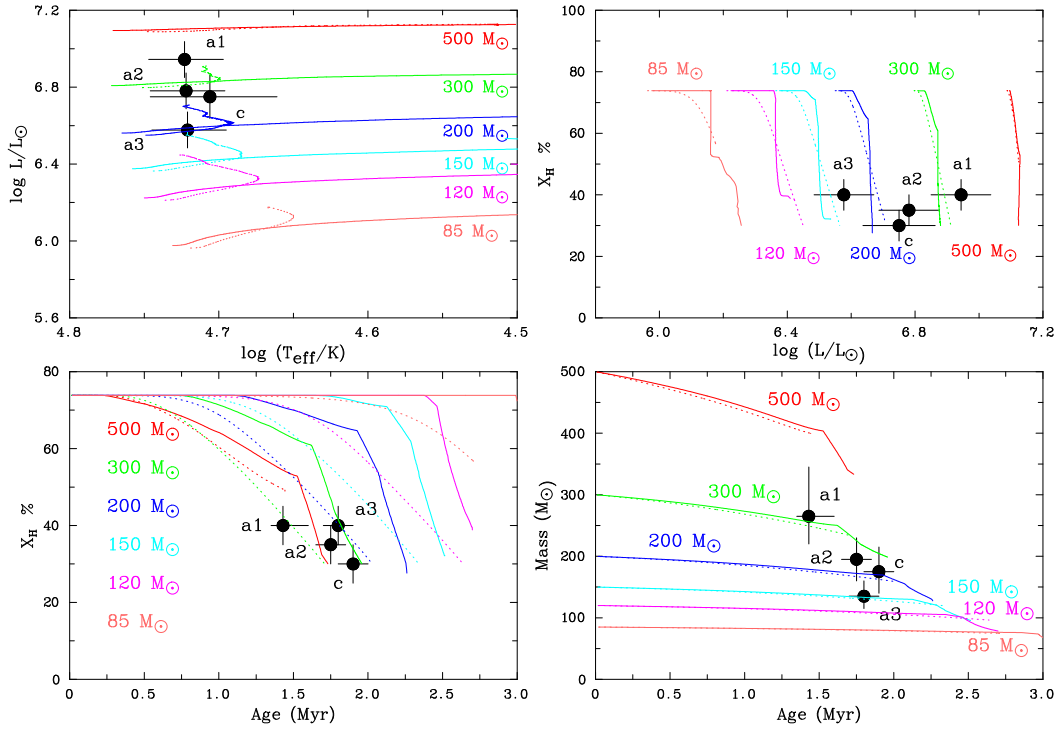


Figure 3.6: Comparison between LMC-metallicity models calculated for the main-sequence evolution of 85 - 500 M_{\odot} stars, initially rotating at $v_{\text{init}}/v_{\text{crit}} = 0.4$ (dotted) or 0 (solid) and the physical properties derived from our spectroscopic analysis.

Table 3.2: Physical Properties of R136 WN5h stars.

Name	a1	a2	a3	c
BAT99	108	109	106	112
T_* (kK) ^a	53 ± 3	53 ± 3	53 ± 3	51 ± 5
$\log(L/L_\odot)$	6.94 ± 0.09	6.78 ± 0.09	6.58 ± 0.09	6.75 ± 0.11
$R_{\tau=2/3}$ (R_\odot)	$35.4^{+4.0}_{-3.6}$	$29.5^{+3.3}_{-3.0}$	$23.4^{+2.7}_{-2.4}$	$30.6^{+4.2}_{-3.7}$
N_{LyC} (10^{50} s^{-1})	$6.6^{+1.6}_{-1.3}$	$4.8^{+0.8}_{-0.7}$	$3.0^{+0.5}_{-0.4}$	$4.2^{+0.7}_{-0.6}$
\dot{M} ($10^{-5} M_\odot \text{ yr}^{-1}$)	$5.1^{+0.9}_{-0.8}$	$4.6^{+0.8}_{-0.7}$	$3.7^{+0.7}_{-0.5}$	$4.5^{+1.0}_{-0.8}$
$\log \dot{M} - \log \dot{M}_{\text{Vink}}^c$	+0.09	+0.12	+0.18	+0.06
V_∞ (km s^{-1})	2600 ± 150	2450 ± 150	2200 ± 150	1950 ± 150
X_H (%)	40 ± 5	35 ± 5	40 ± 5	30 ± 5
M_{init} (M_\odot) ^b	320^{+100}_{-40}	240^{+45}_{-45}	165^{+30}_{-30}	220^{+55}_{-45}
M_{current} (M_\odot) ^b	265^{+80}_{-35}	195^{+35}_{-35}	135^{+25}_{-20}	175^{+40}_{-35}
M_{K_s} (mag)	-7.6 ± 0.2	-7.3 ± 0.2	-6.9 ± 0.2	-7.4 ± 0.2

(a) Corresponds to the radius at a Rosseland optical depth of $\tau_{\text{Ross}} = 10$

(b) Component R136c is probably a colliding-wind massive binary. For a mass ratio of unity, initial (current) masses of each component would correspond to $\sim 160 M_\odot$ ($\sim 130 M_\odot$)

(c) dM/dt_{Vink} relates to Vink et al. (2001) mass-loss rates for $Z = 0.43 Z_\odot$

3.5 Summary

From this work, we are able to determine the mass of the most massive star, R136a1 which is $320 M_\odot$ larger than our present Sun. This finding annuls the idea that the upper limit of stars is around $150 M_\odot$ (Figer, 2005). This shows that very massive stars do exist in nearby galaxies although it is very rare.

Our next chapter aims to investigate the behavior and fate of these stars after the main sequence. This is interesting because stars with initial mass between 140 to $260 M_\odot$ is believed to end their life as pair creation supernova (PCSN) (Heger & Woosley, 2002).

Chapter 4

Post Main Sequence and Fate of Very Massive Stars

4.1 Introduction

Further to the discussion on the most massive stars on the MS, we want to study the structure and evolution of very massive stars with mass ranging from 120-500 M_{\odot} and discuss their fate beyond the main sequence.

The fate of these stars depends on their mass, composition and rotational rate. Massive stars with an initial mass in the range 10-140 M_{\odot} produce a central iron core and eventually collapse (Heger et al., 2003; Langer, 2009). This type of collapse will result in a core collapse supernova (SN) of Type II, Ib or Ic. The classification of these type of supernova depends on the existence of the hydrogen envelope in the star. Stars that undergo core collapse at the end of their evolution will become either neutron stars or black holes. For massive stars with initial mass in the range of 140-260 M_{\odot} , their fate depends on their metallicity. If the stars are Pop III stars they are expected to become pair creation supernova. For very massive stars that experience mass loss (Pop I and Pop II), for the same initial mass they are expected to collapse and become black holes or

Table 4.1: Final evolution of the stars depending on their initial mass at ($Z \equiv 0$) (Heger et al., 2003; Woosley et al., 2007).

Mass (M_{\odot})	Remnant	Event
10-95	Black hole/Neutron stars	Ordinary supernovae
95-135	Black hole/Neutron stars	Pulsation instability supernovae
140-260	Explosion/No remnants	Pair creation supernovae
>260	Supermassive black hole	Unknown

neutron stars depending on their mass loss rate. For non-rotating massive stars in Pop III ($Z \equiv 0$), the classifications of the fate depending on their initial mass are listed in Table 4.1.

Although theory predicts very massive stars in Pop III will end up as PCSNe, this prediction is still debated since no chemical signature is observed in the extremely metal-poor (EMP) (Nomoto et al., 2003; Frebel et al., 2005) stars. Alternatively, if the first generation stars were not very massive, Pop III PCSNe would not occur (Stacy et al., 2010).

Two PCSN candidates have been observed in the local galaxies, which are SN 2006gy and SN2007bi. SN 2006gy (Smith et al., 2007) and SN 2007bi (Gal-Yam et al., 2009) which both have an enormous luminosity and release great amount of energies from their explosion are believed to be PCSN candidates. SN 2006gy is thought to be PCSN candidate as suggested by Smith et al. (2007) because a huge amount of ^{56}Ni ($>10 M_{\odot}$) is required to explain the peak luminosity. However, there is no clear agreement between theoretical and observations in order to explain whether SN2006gy is a PCSN candidate (see Kawabata et al., 2009). SN 2007bi is the most promising candidate since it shows consistency with the observed light curve (LC) and the nebular spectra of SN 2007bi (Gal-Yam et al., 2009). Theoretical prediction of PCSN model deduce a large amount of ^{56}Ni , high total mass and kinetic energy, slow expansion velocity and luminosity that fit very well with SN 2007bi observation data (Langer, 2009).

Attempts to build progenitor models to describe this type of supernova using a very

low metallicity (Population III) have been done extensively by several authors (Heger & Woosley, 2002; Langer, 2009; Moriya et al., 2010; Yoshida & Umeda, 2011). Their models were mostly evolved until the end of helium burning and the prediction of the fate of the star is done by estimating the mass of the carbon-oxygen core at the end of the calculation.

In this work, we evolve grids of models with different metallicities in order to investigate which models will end up as PCSNe. Since very massive stars and PCSN candidates have been observed in local galaxies, we attempt to provide the grid of very massive stars with the same metallicity in the local galaxies in order to test our prediction.

Stellar models of 120-500 M_{\odot} at solar, LMC and SMC metallicities with $v_{ini}/v_{crit} = 0.4$ and $v_{ini}/v_{crit} = 0$ have been calculated. These models are the extension from Chapter 3 where we evolve the models past the main sequence stage. In this work, we did not include the non-rotating SMC metallicity models due to computational difficulties in the LBV phase. All models (both rotating and non-rotating) start at ZAMS. Most of the rotating models are computed until the end of oxygen burning while for the non-rotating models, most models with solar metallicity are computed until the end of oxygen burning whereas all the LMC metallicity models, ended at the end of the helium burning.

A short introduction of Wolf Rayet type stars and supernova (SN) classifications are explained in this chapter before we proceed to the results.

4.2 Wolf-Rayet stars

Wolf-Rayet (WR) stars were first discovered in 1867 by the astronomers Charles Wolf and Georges Rayet, who observed broad spectral emission in three stars in Cygnus. This type of stars are massive stars (with mass larger than 25 M_{\odot}) and it ejects matter at high velocities through stellar winds. WR stars can be classified into two categories:

- WN : stars with a spectrum dominated by He and N lines

- WC : stars with a spectrum showing strong He, C and O lines

4.2.1 Observational classification for WR stars

The current classification scheme is based on relative strength of the emission lines and distinguishes between the following subtypes (see Crowther, 2007).

- **WN subtypes**

It is based on the ratios of $N_{\text{III-IV}}$ and $\text{He}_{\text{I-II}}$ lines. This class is divided into 10 subtypes, ranging from WN2 to WN11. The WN2 to WN5 stars are grouped under the generic name “early” WN stars (WNE), and WN7 to WN9 as “late” WN stars (WNL). WN6 stars are transition between WNE and WNL types. WN10 and WN11 classes include the WR stars with spectrum very similar to the spectrum of O-type stars.

- **WC subtypes**

These stars are distinguished on the basis of line ratios (C_{III} and C_{IV}) and the appearance of $O_{\text{III-IV}}$ lines. The subtypes range from WC4 to WC9, with WC4-WC6 are the “early” stars (WCE) and WC7-WC9 are referred as the “late” type.

- **WO subtypes**

This is the subtypes for rare WR stars with strong O_{IV} lines. It ranges from WO1 to WO4, depending on the relative strength of the $O_{\text{V-VI}}$ and C_{IV} lines.

- **WN/C subtypes**

These stars are considered to be an intermediate stage between WN and WC types.

4.2.2 Classification scheme applicable to Geneva stellar evolution code

WR star (sub-)types classification is based on the spectrum of the star and it is easy to apply into the stellar models due to the simple treatment of the atmosphere in the code. Therefore, we adapt the observational criteria that can be applied to stellar models. The following criteria are based on the surface properties (Meynet & Maeder, 2005):

- **WR star**

A star become a WR star when $\log T_{\text{eff}} > 4$ with mass fraction of hydrogen, $X_s < 0.3$. Otherwise, it is a standard O-type star (on the MS).

- **eWNL phase**

A WR star is said to be of the eWNL type when the mass fraction of hydrogen at the surface is larger than 10^{-5} , The small “e” in front of WNL is adopted from Foellmi et al. (2003) for WNL and WNE phases are based on stellar evolution criteria instead of spectroscopy.

- **eWNE stars**

A star with depleted hydrogen surface ($X_s < 10^{-5}$) and with a surface carbon abundance smaller than nitrogen abundance is a eWNE star.

- **WC or WO phase**

WR stars without hydrogen in their surface with carbon abundance greater than nitrogen abundance are in WC or WO phase. To differentiate between these two subtypes, we use the number ratio $\frac{\text{C}+\text{O}}{\text{He}}$. If this ratio smaller than 1, we have a WC star, otherwise we have a WO star.

These criteria allow us to determine the type and phase of WR stars by using only the surface properties computed by the stellar code.

4.3 Supernova classification

Almost all massive and very massive stars are predicted to explode as supernovae at the end of their life. These stars will undergo core-collapse phase before becoming supernovae. Supernovae can be classified in various types and subtypes according to their spectra and light curve properties (shown in Fig. 4.1). The first distinction in the classification of SNe is the existence of hydrogen lines in their spectra. SNe without hydrogen lines are classified as SN Type I while those with hydrogen lines as Type II. These two types of SNe can be divided into other sub-types according to the presence of He and Si in their spectra. Here we list out their subtypes:

- **Type I:** No hydrogen lines in their spectra
 - Type Ia : The spectra contain silicon (SiII) lines.
 - Type Ib : The spectra do not contain silicon (SiII) lines but contain helium (HeI) lines
 - Type Ic : The spectra do not contain both silicon (SiII) and helium (HeI) lines.

The progenitor of SN Type Ia is from the thermonuclear explosion of carbon white dwarf (WD) stars (Hoyle & Fowler, 1960).

SN Type Ib/c is associated with the core collapse of massive stars which have lost their hydrogen rich envelope (Type Ic) or both their hydrogen and helium rich envelopes (Ic) through mass loss. It is thus directly related to WR stars.

- **Type II:** Hydrogen lines exist in their spectra.
 - Type IIb: This type of SN has initially the spectrum of type II SN but it turns into Type Ib. SN Type IIb is the link between stars which have retained their external hydrogen-rich layers, and those which lost it.

- Type IIL and IIP: L is for “linear” and P is for “plateau”. This classification is made based on the shape of the light curve (luminosity of the SN as a function of time). Type IIL has a linearly decreasing light curve while Type IIP produces plateau in the light curve.
- Type IIn: This type of SN has narrow lines in its spectrum which is usually produced by the interaction between the ejecta and circumstellar medium (CSM).

Massive stars in the range of 8-130 M_{\odot} undergo core-collapse at the end of their evolution and become Type Ib/c and Type II supernovae unless the entire star collapses into a black hole with no mass ejection. These Type Ib/c and II supernovae (as well as Type Ia supernovae) release large explosion energies and eject explosive nucleosynthesis materials, thus having strong dynamical, thermal, and chemical influences on the evolution of interstellar matter and galaxies.

If the core of the star encounters the electron-positron instability it will lead to the ignition of explosive oxygen burning and it completely unbind the star. This phenomena is called pair creation SN (PCSN) and it is predicted the energy released is nearly 10^{53} ergs. Progenitors of PCSN are believed to be massive stars in the range of 140-260 M_{\odot} . Recently, two very energetic supernovae Type IIn and Type Ic are detected and one of them is probably a candidate of PCSN. In the section 4.3.1 and section 4.3.2, we briefly explain the nature of these two supernovae.

4.3.1 SN2006gy

SN2006gy is a SN Type IIn located near the center of host galaxy NGC1260. Its absolute magnitude is around 22 mag and it is more luminous than Type Ia SN by a factor of 10 (Smith et al., 2007; Kawabata et al., 2009). SN 2006gy releases total kinetic energy, $E_k \simeq 10^{51}$ erg. It is still unclear about the mechanisms that produce this enormous

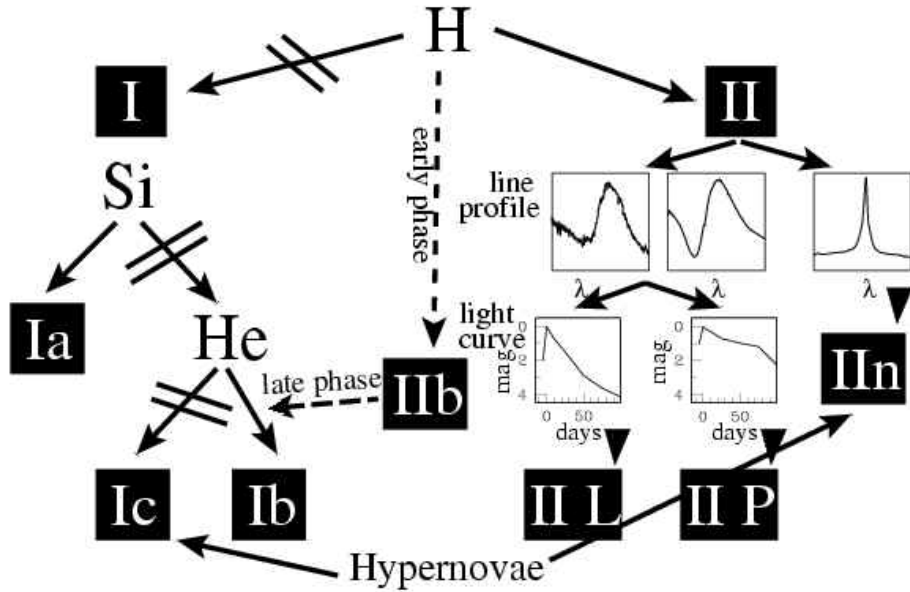


Figure 4.1: SNe classification (Turatto, 2003)

energy. Several mechanisms have been proposed and these are thermal emission from hydrogen recombination front, interaction between CSM and SN ejecta and radioactive decay of ^{56}Ni .

Smith et al. (2007) suggested radioactive decay of ^{56}Ni is the most probable mechanism that power its enormous energy because only weak soft X-ray was detected from this SN (suggesting CSM is not strong) and the observed expansion velocity of hydrogen envelope was unusually slow. The authors also suggested that SN2006gy is a PCSN because a huge amount of ^{56}Ni is required to explain the peak luminosity.

4.3.2 SN2007bi

SN2007bi is an extremely luminous Type Ic supernova. The measured light curve of SN2007bi gives absolute magnitude of ~ 21.3 mag and it is consistent with the decay rate of radioactive ^{56}Co . This supernova releases a great amount of kinetic energy, $E_k \sim 10^{53}$ erg which is comparable to those derived for the most energetic γ -ray bursts, placing

this event among the most extreme explosions known (Gal-Yam et al., 2009). This SN is located within a dwarf galaxy ($\sim 1\%$ the size of Milky Way).

Gal-Yam et al. (2009) measured the exploding core mass and predicted to be likely $\sim 100 M_{\odot}$. They compared the theoretical light curve of PCSN models (Heger & Woosley, 2002; Kasen et al., 2008) with the light curve data obtained from the observation (see Fig. 4.2). The comparison gives a very good agreement, suggesting it is a star exploding with helium core mass around $\sim 100 M_{\odot}$.

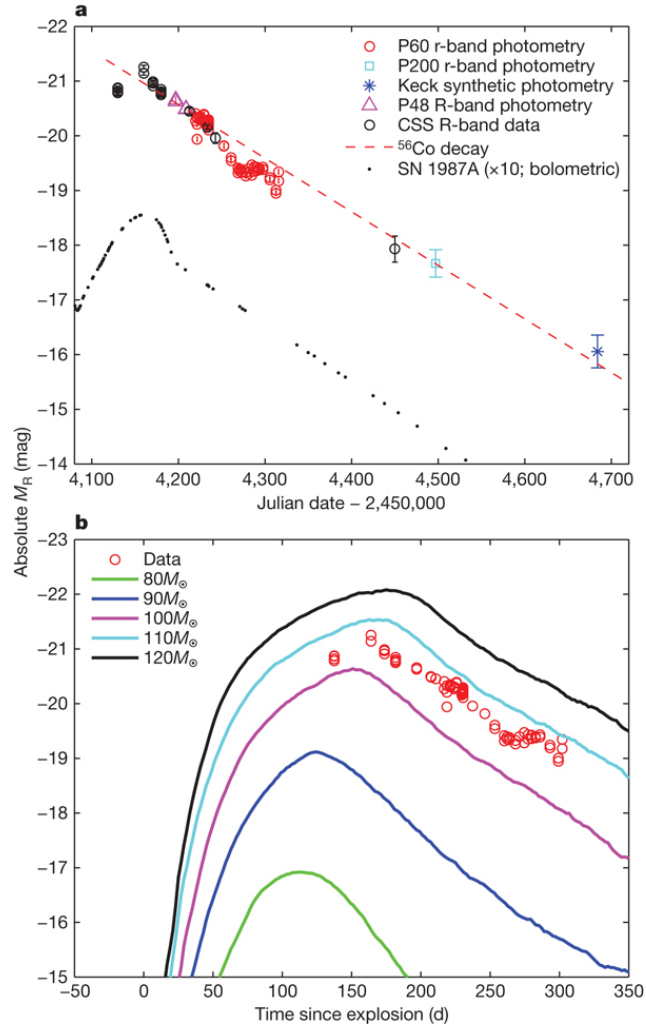


Figure 4.2: a: The R-band light curve of SN2007bi. b: Comparison with theoretical light curve of PCSN model with SN2007Bi observation (Gal-Yam et al., 2009).

4.4 Physics of the models

GENEC or Geneva stellar evolution code is used in calculating these VMS models. The details of the physical ingredients of the models are similar as described by Ekström et al. (2012). We list out the main features here:

- The initial abundances for these models are listed in Table 4.2. We have adopted three different metallicities, which are solar, Large Magellanic Cloud (LMC) and Small Magellanic Cloud (SMC) metallicities. The mixture of heavy elements is taken from Asplund et al. (2005) except for the Ne abundances where we have adopted from Cunha et al. (2006).
- Nuclear reactions are generated by NetGen tools where they take most of the data from NACRE (Angulo et al., 1999). The current NACRE data have been re-determined and updated and some of the comparison to NACRE values and a short description of the effects on stellar evolution has been described in Ekström et al. (2012).
- Neutrino energy loss in plasma, pair and photoneutrino processes are taken from Itoh et al. (1989) and Itoh et al. (1996).
- The opacities are taken from OPAL (Iglesias & Rogers, 1996) and completed with low temperature opacities from Ferguson et al. (2005) which are adapted for the high Ne abundance.
- The convective core is extended with an overshoot parameter $d_{\text{over}}/H_P = 0.10$ starting from the Schwarzschild limit.
- Since models calculated are $> 100M_{\odot}$, the outer convective zone is treated according to the mixing length theory, $\alpha_{\text{MLT}} = 1.0$. This is because for the most luminous models, the turbulence pressure and acoustic flux are needed to be included in the

Table 4.2: Hydrogen (X), helium (Y) and metal (Z) mass fractions for the chemical abundances in our models.

	X	Y	Z
Solar	0.7200	0.2659	0.014
LMC	0.7381	0.2559	0.006
SMC	0.7471	0.2508	0.002

treatment of the envelope. The choice of the outer convective zone for difference initial mass has been described in detail in Ekström et al. (2012).

- The treatment of rotation in these models has been discussed extensively by Maeder & Meynet (2000) and references therein. For the rotating models we use $v_{\text{ini}}/v_{\text{crit}} = 0.4$. This will correspond to the 97 km s^{-1} for $120 M_{\odot}$ and 141 km s^{-1} for $500 M_{\odot}$ at the main sequence.
- We have adopted mass loss for the hot O stars from Vink et al. (2001). When the models reach the Wolf-Rayet (WR) transition, $X_s = 0.3$ we use the mass loss rate of WR from Nugis & Lamers (2000) or Gräfener & Hamann (2008) depending on which effective temperature is reached by the models. For the temperature domains not covered by Vink et al. (2001) and Nugis & Lamers (2000) or Gräfener & Hamann (2008), mass loss prescription from de Jager et al. (1988) is used.
- For rotating models, we applied to the radiative mass-loss rate the correction factor described in Maeder & Meynet (2000)

$$\dot{M}(\Omega) = F_{\Omega} \cdot \dot{M}(\Omega = 0) = F_{\Omega} \cdot \dot{M}_{\text{rad}}$$

$$\text{with } F_{\Omega} = \frac{(1 - \Gamma)^{\frac{1}{\alpha} - 1}}{\left[1 - \frac{\Omega^2}{2\pi G \rho_m} - \Gamma\right]^{\frac{1}{\alpha} - 1}}, \quad (4.1)$$

where $\Gamma = L/L_{\text{Edd}} = \kappa L/(4\pi cGM)$ is the Eddington factor (κ is the electron-scattering opacity), and α the force multiplier parameter depending on T_{eff} .

Most of the models reach the end of He-burning and some of the models evolved as far as the end of O-burning. After He-burning, the evolution of the core and the surface are separated since the core evolves very fast due to the neutrino emission. From this stage onwards, we can safely assume the surface properties are not significantly changed until the end of the evolution. In particular, the total mass will not change by more than a few solar mass, thus not changing the fate of the models.

4.5 Hertzsprung-Russell (HR) lifetimes and diagrams

4.5.1 Lifetimes and surface properties

The key properties of the models are summarised in Tables 4.3, 4.4 and 4.5 at the end of hydrogen, helium burning and the final model respectively. For the lifetime calculation, the start of a burning stage is chosen when 0.3% in mass fraction of the main burning fuel is burnt. A burning stage is completed when the mass fraction of the main fuel is lower than 10^{-5} . In Tables 4.3, 4.4 and 4.5, we have listed the lifetimes for hydrogen burning, helium burning and the total lifetimes.

In Tables 4.3, 4.4 and 4.5 we list the initial mass, current mass, surface abundance profiles (H (hydrogen), He (helium), C (carbon), N (nitrogen), O (oxygen) and Eddington factor (Γ_{Edd}). In Table 4.3, we add ratio of initial velocity over critical velocity ($v_{\text{ini}}/v_{\text{crit}} = 0.4$), Eddington factor at initial mass ($\Gamma_{\text{Edd,init}}$), lifetime at the end of main sequence (τ_H) and lifetime at the end of hydrogen burning and the duration the star spend as an O-type star (τ_o). For Table 4.3, we include the average main sequence velocity, $\langle v_{MS} \rangle$ while for Table 4.4 and Table 4.5 we present the average velocity, $\langle v_{eq} \rangle$.

Duration of the O-star, end of H-burning, He-burning and total mass are indicated in Tables 4.3, 4.4 and 4.5. There are different patterns affecting the lifetimes:

1. O-star lifetimes and end of H-burning lifetimes: τ_o and τ_H are influenced by rotation.

The difference in the lifetimes between different metallicity for the same initial mass is very small. Difference in the end of H-burning lifetimes for rotating and non-rotating models of $150 M_{\odot}$ at solar metallicity models is $\sim 14\%$. The same result is obtained for the same initial mass for both rotating and non-rotating at LMC metallicity.

2. End of He-burning and final models: τ_{He} and total lifetimes are influenced by metallicity and mass loss. From Table 4.4, we can see clearly the difference for example, for the $150 M_{\odot}$, non-rotating model at solar and LMC metallicities. The solar metallicity model has a longer He-burning lifetime compared to the LMC metallicity models. This is due to the higher mass loss rate at solar metallicity which lowers the luminosity of the models.

Table 4.3: Key properties of stellar models at the end of H-burning phase. The mass are in solar mass, $\Gamma_{\text{Edd}_{\text{init}}}$ is the initial Eddington factor, the lifetimes are in 10^6 years, the main sequence velocity are in km s^{-1} and the abundances are mass fraction abundances.

M_{ini}	Z	$\frac{v_{\text{ini}}}{v_{\text{crit}}}$	$\Gamma_{\text{Edd}_{\text{init}}}$	τ_H	τ_o	M_{current}	$\langle v_{\text{MS}} \rangle$	H	He	C	N	O	Γ_{Edd}
120	0.014	0.0	0.376	2.671	2.671	63.7	0.000	2.042e-01	7.821e-01	8.583e-05	8.152e-03	1.055e-04	0.625
150	0.014	0.0	0.426	2.497	2.424	76.3	0.000	1.354e-01	8.509e-01	9.257e-05	8.148e-03	9.909e-05	0.652
200	0.014	0.0	0.489	2.323	2.164	95.2	0.000	7.511e-02	9.112e-01	9.930e-05	8.144e-03	9.235e-05	0.686
300	0.014	0.0	0.572	2.154	1.847	65.2	0.000	1.286e-03	9.850e-01	1.304e-04	8.110e-03	7.932e-05	0.594
500	0.014	0.0	0.666	1.990	1.540	56.4	0.000	2.242e-03	9.841e-01	1.256e-04	8.116e-03	8.029e-05	0.568
120	0.014	0.4	0.374	3.137	2.563	34.6	96.934	1.562e-03	9.848e-01	1.330e-04	8.101e-03	8.477e-05	0.463
150	0.014	0.4	0.417	2.909	2.383	37.1	105.078	1.812e-03	9.845e-01	1.304e-04	8.106e-03	8.412e-05	0.478
200	0.014	0.4	0.479	2.649	2.073	40.0	142.162	1.406e-03	9.849e-01	1.333e-04	8.102e-03	8.299e-05	0.495
300	0.014	0.4	0.564	2.376	1.832	43.2	166.165	1.850e-03	9.845e-01	1.326e-04	8.104e-03	8.226e-05	0.511
500	0.014	0.4	0.717	2.132	1.647	48.1	141.403	1.239e-03	9.851e-01	1.383e-04	8.097e-03	8.079e-05	0.532
120	0.006	0.0	0.376	2.675	2.699	79.0	0.000	4.034e-01	5.907e-01	3.291e-05	3.499e-03	4.473e-05	0.671
150	0.006	0.0	0.426	2.492	2.515	96.1	0.000	3.275e-01	6.666e-01	3.577e-05	3.497e-03	4.254e-05	0.708
500	0.006	0.0	0.670	1.904	1.694	239.0	0.000	2.584e-02	9.683e-01	5.113e-05	3.485e-03	3.178e-05	0.820
120	0.006	0.4	0.365	3.140	2.703	64.0	121.407	1.712e-03	9.924e-01	6.053e-05	3.472e-03	3.043e-05	0.597
150	0.006	0.4	0.425	2.873	2.384	71.3	138.769	9.907e-04	9.931e-01	6.325e-05	3.469e-03	2.970e-05	0.615
200	0.006	0.4	0.477	2.590	2.115	80.7	170.680	1.217e-03	9.929e-01	6.291e-05	3.469e-03	2.946e-05	0.638
300	0.006	0.4	0.560	2.318	1.846	85.8	232.656	1.332e-03	9.928e-01	6.295e-05	3.469e-03	2.933e-05	0.650
500	0.006	0.4	0.666	2.077	1.638	101.7	234.756	1.373e-03	9.927e-01	6.373e-05	3.469e-03	2.888e-05	0.676
150	0.002	0.4	0.4263	2.921	2.675	128.8	227.558	1.672e-03	9.964e-01	2.128e-05	1.157e-03	8.088e-06	0.720
200	0.002	0.4	0.4766	2.612	2.313	152.3	287.475	1.321e-03	9.967e-01	2.257e-05	1.156e-03	7.823e-06	0.743
300	0.002	0.4	0.5572	2.315	1.957	176.3	387.527	1.108e-03	9.969e-01	2.320e-05	1.155e-03	7.680e-06	0.763

Table 4.4: Key properties of stellar models at the end of He-burning. The mass is in solar mass, the lifetimes in 10^6 years, equatorial velocity $\langle v_{eq} \rangle$ are in km s^{-1} and the surface abundances are mass fraction abundances.

M_{ini}	Z	v_{init}/v_{crit}	τ_{He}	$M_{current}$	$\langle v_{eq} \rangle$	H	He	C	N	O	Γ_{Edd}
120	0.014	0.0	0.308	30.9	0.00	0.00	2.423e-01	4.579e-01	6.149e-19	2.814e-01	0.651
150	0.014	0.0	0.291	41.3	0.00	0.00	2.339e-01	4.356e-01	1.063e-18	3.120e-01	0.707
200	0.014	0.0	0.273	49.4	0.00	0.00	2.072e-01	4.084e-01	2.601e-18	3.656e-01	0.737
300	0.014	0.0	0.297	38.2	0.00	0.00	2.337e-01	4.427e-01	7.306e-19	3.051e-01	0.692
500	0.014	0.0	0.307	29.8	0.00	0.00	2.611e-01	4.636e-01	3.713e-18	2.570e-01	0.641
120	0.014	0.4	0.353	18.8	1.58	0.00	2.920e-01	4.920e-01	1.994e-18	1.979e-01	0.534
150	0.014	0.4	0.345	20.3	1.18	0.00	2.859e-01	4.882e-01	1.117e-18	2.077e-01	0.552
200	0.014	0.4	0.337	22.0	0.50	0.00	2.770e-01	4.839e-01	2.334e-18	2.208e-01	0.570
300	0.014	0.4	0.329	24.0	0.13	0.00	2.696e-01	4.787e-01	3.732e-19	2.335e-01	0.590
500	0.014	0.4	0.321	25.9	0.03	0.00	2.693e-01	4.731e-01	4.892e-19	2.394e-01	0.607
120	0.006	0.0	0.295	54.2	0.00	0.00	2.286e-01	3.911e-01	3.101e-05	3.722e-01	0.753
150	0.006	0.0	0.331	59.7	0.00	0.00	2.413e-01	3.702e-01	2.360e-16	3.804e-01	0.768
500	0.006	0.0	0.262	94.7	0.00	0.00	2.509e-01	3.919e-01	2.427e-17	3.490e-01	0.834
120	0.006	0.4	0.294	39.3	6.84	0.00	2.942e-01	4.570e-01	3.298e-22	2.409e-01	0.692
150	0.006	0.4	0.287	45.7	3.67	0.00	3.103e-01	4.506e-01	1.074e-16	2.312e-01	0.719
200	0.006	0.4	0.282	51.1	1.33	0.00	3.027e-01	4.440e-01	4.966e-20	2.455e-01	0.738
300	0.006	0.4	0.278	54.1	0.35	0.00	2.913e-01	4.391e-01	1.271e-17	2.617e-01	0.748
500	0.006	0.4	0.264	74.9	0.13	0.00	3.302e-01	4.252e-01	2.019e-17	2.367e-01	0.798
150	0.002	0.4	0.251	106.7	64.94	0.00	8.092e-01	1.532e-01	1.555e-06	3.504e-02	0.841
200	0.002	0.4	0.245	129.3	29.88	0.00	8.798e-01	1.086e-01	5.038e-11	9.012e-03	0.863
300	0.002	0.4	0.241	149.8	5.10	0.00	9.376e-01	5.837e-02	8.671e-10	1.413e-03	0.880

Table 4.5: Key properties at the end of the stellar models. The mass are in solar mass, the lifetimes are in million years equatorial velocity $\langle v_{eq} \rangle$ are in km s¹ and the abundances in mass fraction.

M_{ini}	Burning stage	Z	v_{init}/v_{crit}	$M_{current}$	$\langle v_{eq} \rangle$	H	He	C	N	O	Γ_{Edd}	total lifetime
120	end O-burning	0.014	0.0	30.8	0.00	0.00	2.376e-01	4.568e-01	5.234e-19	2.872e-01	0.892	3.007
150	end C-burning	0.014	0.0	41.2	0.00	0.00	2.268e-01	4.332e-01	8.311e-19	3.215e-01	0.969	2.813
200	end C-burning	0.014	0.0	49.3	0.00	0.00	1.949e-01	4.014e-01	1.727e-18	3.849e-01	0.955	2.625
300	end O-burning	0.014	0.0	38.2	0.00	0.00	2.309e-01	4.418e-01	6.659e-19	3.089e-01	0.966	2.473
500	end O-burning	0.014	0.0	29.8	0.00	0.00	2.562e-01	4.629e-01	3.169e-18	2.626e-01	0.875	2.318
120	end O-burning	0.014	0.4	18.7	15.18	0.00	2.858e-01	4.925e-01	1.572e-18	2.035e-01	0.664	3.517
150	end O-burning	0.014	0.4	20.2	0.78	0.00	2.797e-01	4.884e-01	8.785e-19	2.138e-01	0.692	3.295
200	end Ne-burning	0.014	0.4	21.9	1.88	0.00	2.712e-01	4.838e-01	1.882e-18	2.268e-01	0.714	3.025
300	end O-burning	0.014	0.4	23.9	22.81	0.00	2.650e-01	4.784e-01	3.195e-19	2.385e-01	0.731	2.737
500	end Ne-burning	0.014	0.4	25.8	0.03	0.00	2.643e-01	4.726e-01	4.022e-19	2.449e-01	0.751	2.507
120	end He-burning	0.006	0.0	54.2	0.00	0.00	2.286e-01	3.911e-01	3.101e-05	3.722e-01	0.753	2.997
150	end He-burning	0.006	0.0	59.7	0.00	0.00	2.413e-01	3.702e-01	2.360e-16	3.804e-01	0.768	2.848
500	end He-burning	0.006	0.0	94.7	0.00	0.00	2.509e-01	3.920e-01	2.427e-17	3.490e-01	0.834	2.185
120	end O-burning	0.006	0.4	39.2	27.47	0.00	2.889e-01	4.567e-01	2.738e-22	2.465e-01	0.832	3.476
150	end Ne-burning	0.006	0.4	45.6	8.39	0.00	3.057e-01	4.505e-01	9.168e-17	2.360e-01	0.852	3.167
200	end O-burning	0.006	0.4	51.0	25.36	0.00	2.982e-01	4.436e-01	4.256e-20	2.503e-01	0.869	2.907
300	end O-burning	0.006	0.4	54.0	0.17	0.00	2.856e-01	4.383e-01	1.031e-17	2.681e-01	0.879	2.629
500	end O-burning	0.006	0.4	74.8	0.28	0.00	3.220e-01	4.249e-01	1.494e-17	2.452e-01	0.929	2.390
150	end O-burning	0.002	0.4	106.5	160.57	0.00	7.922e-01	1.634e-01	1.351e-06	4.177e-02	0.932	3.196
200	end O-burning	0.002	0.4	129.2	187.90	0.00	8.730e-01	1.131e-01	4.089e-11	1.138e-02	0.956	2.889
300	end O-burning	0.002	0.4	149.7	10.72	0.00	9.362e-01	5.969e-02	8.295e-10	1.487e-03	0.959	2.587

4.5.2 Hertzsprung Russell diagrams

Tracks of Hertzsprung Russell (HR) diagrams of the $150 M_{\odot}$ models for all metallicities in this work are presented in Fig. 4.4 for both rotating and non-rotating models. Note that the HR diagram that are used in this figure is with the uncorrected T_{eff} . We choose this initial mass because we have calculated all metallicities for both rotating and non-rotating models except for SMC model where only the rotating model is available.

The evolution of the models are mostly affected by rotation and mass loss.

1. Mass Loss

As we go to the lower metallicities, lower mass loss occurs during the evolution. Lower metallicity models tend to have higher luminosity and this can be clearly seen in Fig. 4.3 bottom left. Models with higher mass loss will enter the WR phase faster due to the removal of hydrogen surface by the stellar winds. Mass loss effects can be studied through the sub-type of WR star during the evolution. Models with higher mass loss rate evolve to the WNE, WC/WO stars compared to the lower mass loss rate models. For example, the rotating solar metallicity model reaches the eWNE phase shortly after it enters the WR phase which means the surface hydrogen content is being removed completely during the evolution. Rotation also enhances the mass loss rate and this will be discussed in the next part.

2. Rotation

Rotating effects increase the lifetimes of the models in their HRD tracks. Rotating models experience longer H-burning phase due to the internal mixing during the evolution. Rotating models also evolve only at the hotter region and stay hotter compared to the non-rotating models due to the mixing of helium into the outer layers.

Rotation also enhances the mass loss rate of the models. This can be seen that when rotating models enter the WR phase during the H-burning while non-rotating

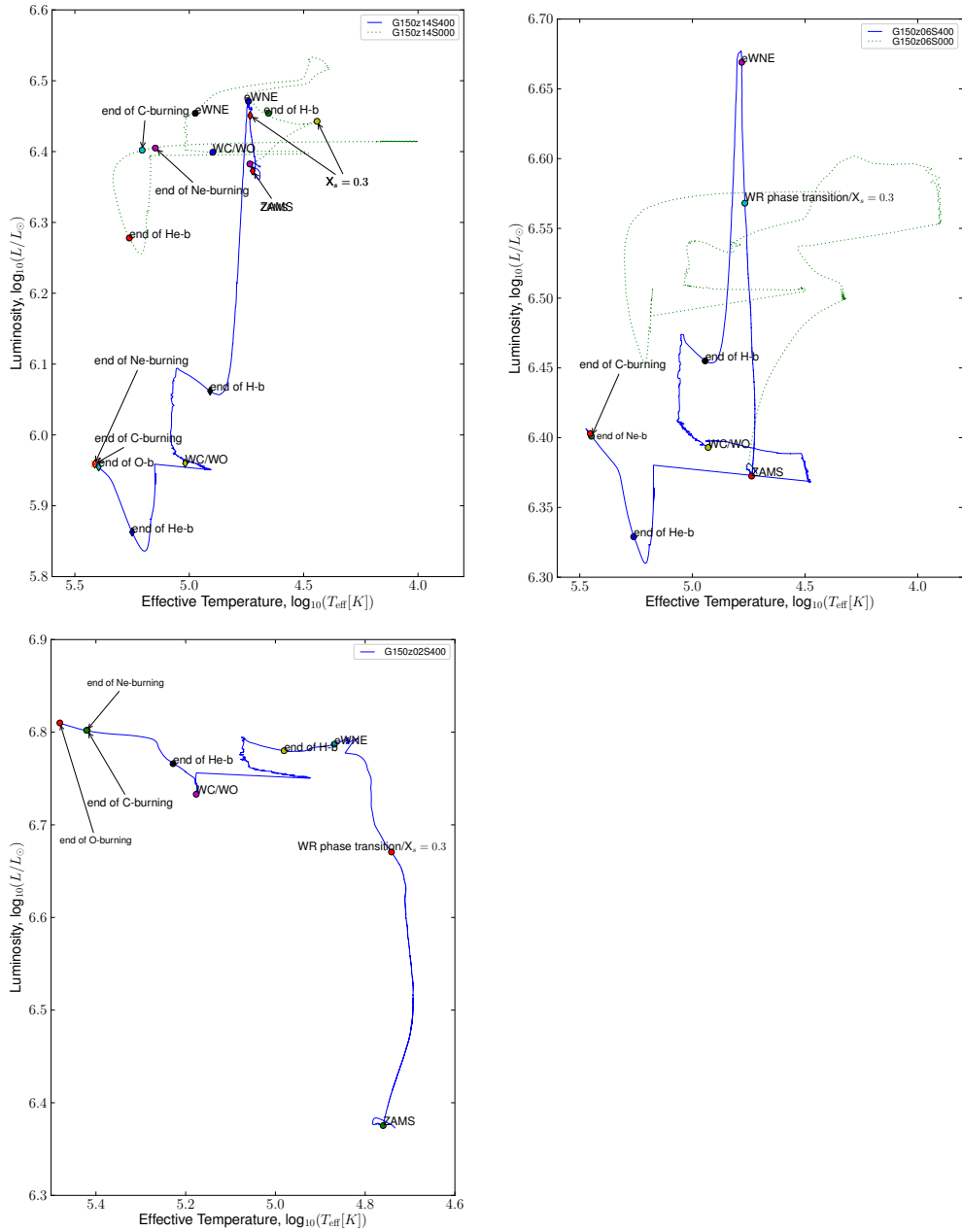


Figure 4.3: HR diagrams of rotating solar, LMC and SMC metallicities.

models enter WR phase they are near to the central hydrogen exhaustion (in solar metallicity case) and during He-burning (for LMC metallicity model). Finally, the rotating models evolve to higher T_{eff} towards the end of the evolution in the HR track while the non-rotating models will evolve to cooler region possibly to the red giant region.

4.6 Eddington limit

In this section, we shall discuss the relationship between Eddington limit, Γ_{Edd} with luminosity and mass loss rate. Eddington factor is given by

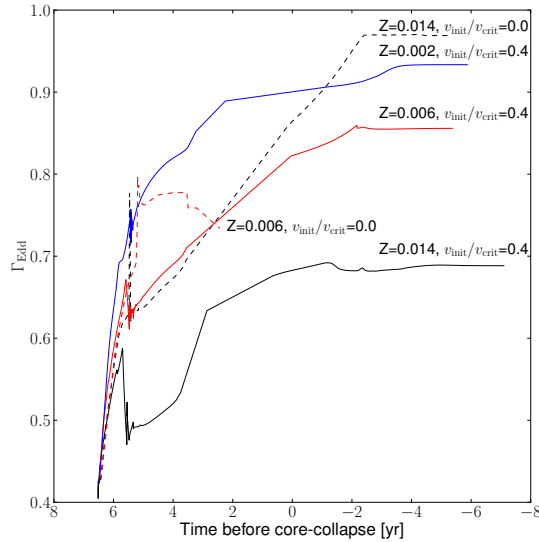


Figure 4.4: Γ_{Edd} of $150 M_{\odot}$ in solar, LMC and SMC metallicities as a function of time before core-collapse. Solid line represents rotating models and dashed line represents non-rotating models.

$$\Gamma_{\text{Edd}} = \frac{\kappa L}{4\pi c G M} \quad (4.2)$$

where M is the mass of the star, G the gravity and L the luminosity of the star. This factor is defined as the ratio to the Eddington luminosity, $L = L_{\text{Edd}}$. The limit for Γ_{Edd}

is 1. In Geneva code, the value of Γ_{Edd} in Tables 4.3, 4.4 and 4.5 is the taken at the surface of the models. The value of Γ_{Edd} depends on several factors, i.e metallicity, mass loss and rotation.

In Fig. 4.4, we present this factor as a function of time before core collapse and the mass loss rate of $150 M_{\odot}$ both rotating and non-rotating models as a function of time. For the rotating models, the Γ_{Edd} depends on the metallicity, Z . As we go to the higher Z , the value of Γ_{Edd} becomes lower. This shows that models with low Z easily become unstable where the outer layers of the models are no longer bound. However, comparing between rotating and non-rotating models at solar metallicity, we found that the non-rotating models have higher Γ_{Edd} at the end of the evolution. The Γ_{Edd} final value for $150 M_{\odot}$ non-rotating models at solar metallicity is around ~ 0.97 which is extremely high.

We investigate this value and we found that it is affected by the mass loss rate. Fig. 4.5 (left panel) shows the mass loss for non-rotating models peaked at the start of O-burning where the surface temperature or effective temperature starts to decline rapidly (see Fig. 4.5, right panel).

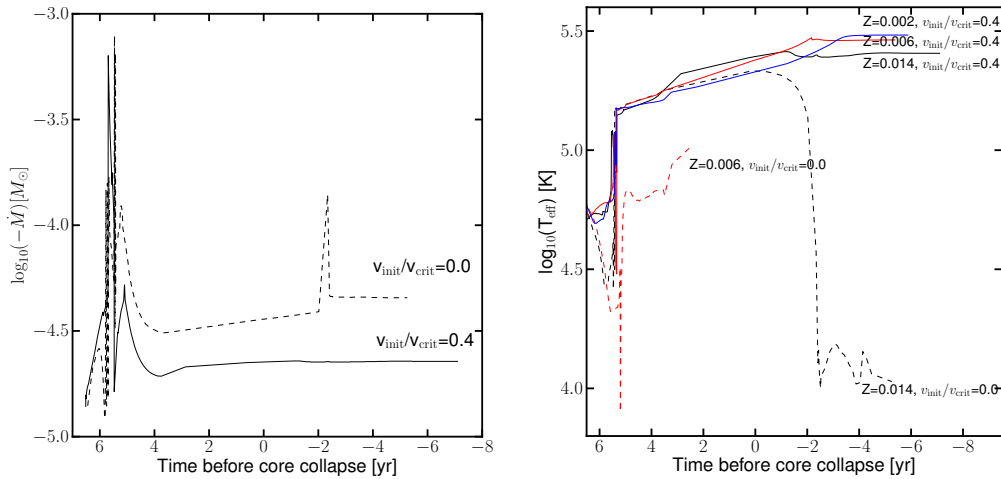


Figure 4.5: Mass loss rate of $150 M_{\odot}$ in solar metallicity both rotating and non-rotating models as a function of mass loss. Right panel: Effective temperature of $150 M_{\odot}$ in solar, LMC and SMC metallicities as a function of time before core collapse.

4.7 Internal structure evolution

4.7.1 Central evolution

In this section, the central evolution of the models will be discussed. Evolutionary tracks in the central temperature vs central density plane ($\log T_c$ - $\log \rho_c$ diagram) of solar, LMC and SMC metallicities models are represented in Figs. 4.6 and 4.8.

These tracks explain the movement of the stars at each burning stages. It is meaningful to compare these tracks with the Kippenhahn diagram (see Sect. 4.7.2) in order to understand the movements in the tracks. Mass loss and rotation play dominant role in the central evolution.

In Fig. 4.6, the evolutionary tracks at solar metallicity show the tracks evolve far from the pair creation instability region, $\Gamma < 4/3$. This shows that models at solar metallicity do not suffer from stability issue. However, the details of these tracks need to be investigated further by analyzing the Kippenhahn diagram and the carbon core of the models. In this section we describe the prediction of which models will enter the region presented in the gray shaded area.

Fig. 4.6 (right panel) shows the evolutionary tracks for 150, 200, 300 and 500 M_\odot models zoomed in advanced stages. 150 M_\odot non-rotating model gives the highest tracks while 500 M_\odot rotating model gives at the lowest tracks. These situations are due to the higher mass loss rate occurring in the 500 M_\odot rotating model.

For LMC metallicity models, the evolutionary tracks are presented in Fig. 4.8. The zoomed tracks, rotating models evolve until the end of O-burning. 150 M_\odot rotating model moves closer towards the stability limit compared to other more massive rotating models. However, the 150 M_\odot non-rotating model is expected to move even closer compared to its rotating model although in the tracks the non-rotating model stops at C-burning. If this model evolves further, it might enter this instability region.

The final figure (Fig. 4.8) in this section is the SMC metallicity models. The evolu-

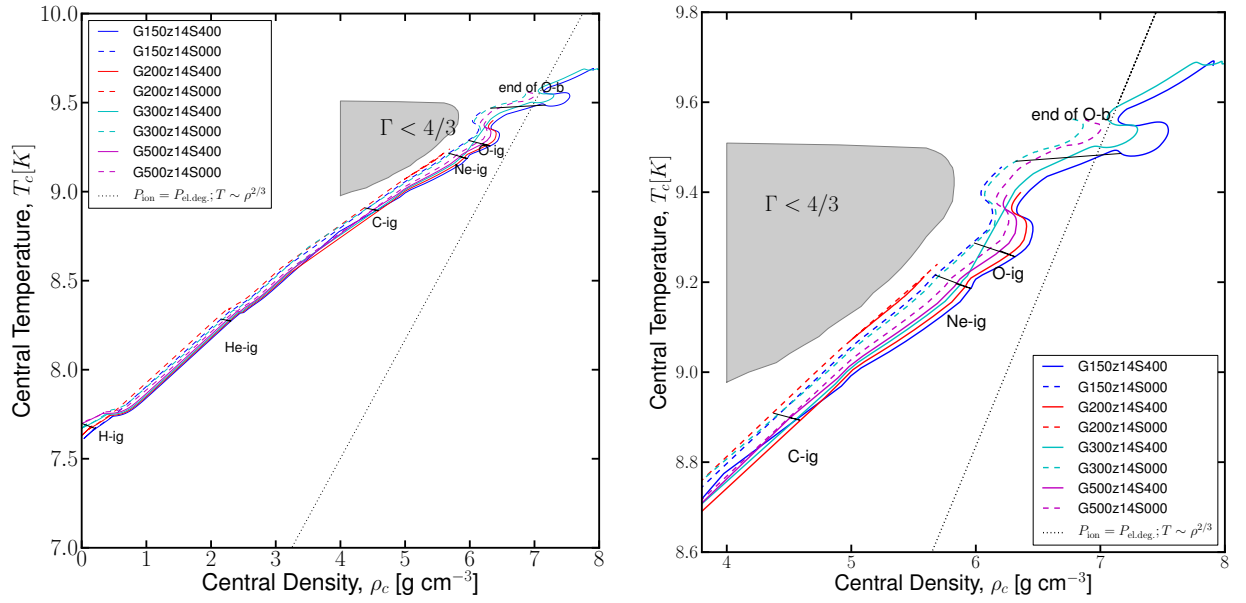


Figure 4.6: Log T_c vs Log ρ_c diagrams: Evolutionary tracks for 150-500 M_\odot models for solar metallicity (left panel) and the evolutionary tracks zoomed in the advanced stages for 150-500 M_\odot models (left panel). The additional dotted line corresponds to the limit between non-degenerate and degenerate electron gas ($P_{\text{el,perfectgas}} = P_{\text{el,degenerategas}}$). The gray shaded area is the pair instability region.

tionary tracks clearly show all the models enter instability region. However, this analysis is not completed without investigating the carbon-oxygen core mass, M_{CO} which will be discuss in next section.

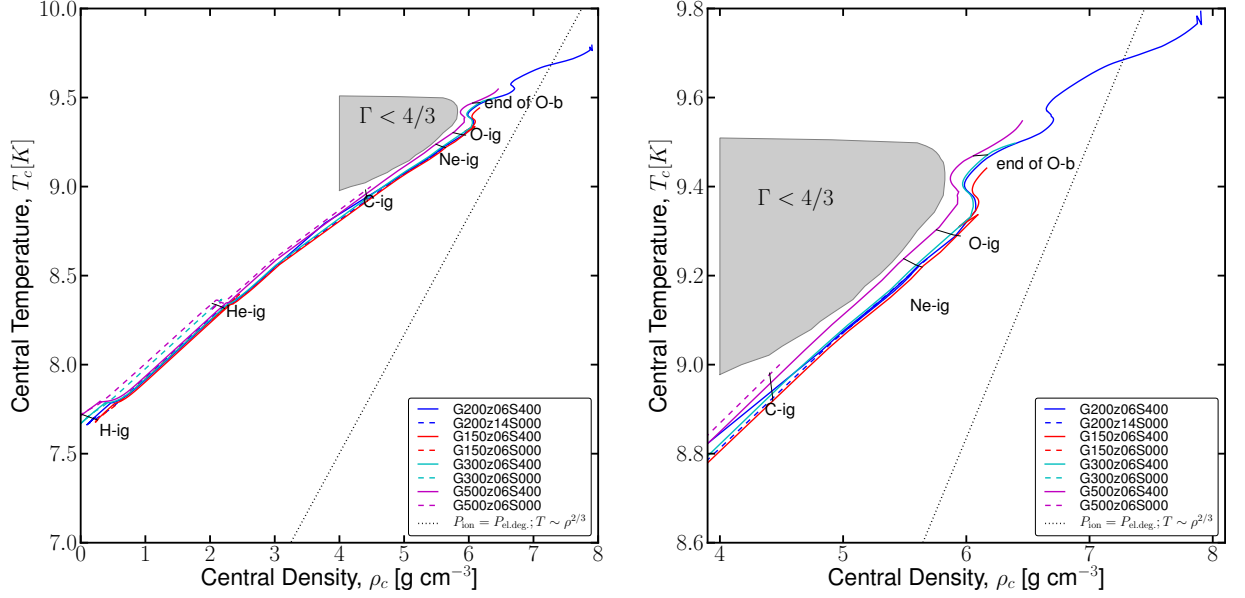


Figure 4.7: Log T_c vs Log ρ_c diagrams: Evolutionary tracks for 150-500 M_{\odot} models for LMC metallicity. The additional dotted line corresponds to the limit between non-degenerate and degenerate electron gas ($P^{\text{el,perfectgas}} = P^{\text{el,degenerategas}}$). The gray shaded area is the instability region.

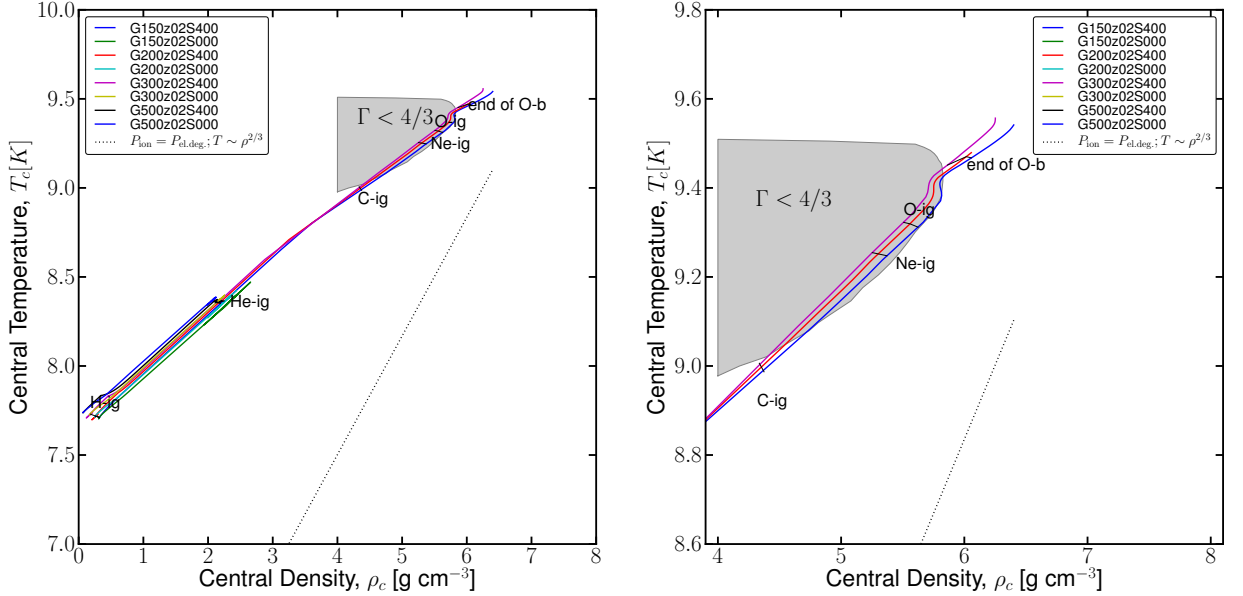


Figure 4.8: Log T_c vs Log ρ_c diagrams: Evolutionary tracks for 150-500 M_\odot models for SMC metallicity. The additional dotted line corresponds to the limit between non-degenerate and degenerate electron gas ($P_{\text{ion}}^{\text{perfectgas}} = P_{\text{el,deg}}^{\text{degenerategas}}$). The gray shaded area is the instability region.

4.7.2 Kippenhahn diagrams

Figs. 4.9 and 4.10 show the Kippenhahn diagrams for 150 M_\odot model for solar, LMC and SMC metallicity models. In Fig. 4.9 we have plotted the diagrams in terms of the age of the models and in Fig. 4.10 in terms of time before core-collapse. In the Kippenhahn diagrams, we can also see the effects of mass loss and rotation during the evolution.

Effects of mass loss can be seen in the rotating models for different metallicities. The models start to lose their hydrogen rich envelope when entering the eWNE phase and we observe drastic mass loss occurs during this phase in our models. As we go to the lower metallicity, the models shred very slowly their hydrogen envelope and the models manage to retain their mass until the end of the evolution. This can be seen by the eWNE region that we have mapped in Fig. 4.9.

The rotation effects can be seen from the comparison of rotating and non-rotating models. Rotating models have longer lifetimes compared to the non-rotating models.

This has been explained in Section 4.5.1. Rotation enhances the mass loss rate which reduce the final mass of the models compared to non-rotating models. From Fig. 4.9, rotating models experience shorter eWNE phase compared to their non-rotating models which explains the smaller mass loss rates in the non-rotating models.

The next figure, Fig. 4.10, we present the Kippenhahn diagrams in terms of time before core-collapse. We want to study which burning phase occur in each models that we have presented in Fig. 4.9. The evolution of total mass of the stars can be seen clearly in this figure. As we go to lower metallicities, the total mass of the models reduces through mass loss due to stellar winds. We also find the low metallicities models have larger convective zone for the He core. After the core convective zone of He-core shrinks, the shell helium burning starts. The effect of mass loss for the begining of He shell burning where higher metallicities models tends to start the burning earlier than low metallicities models. During the He shell burning, the core contracts and carbon core burning starts. In the models, we also observe that the C shell also starts to burn at the same time as the C-burning ignition.

As for the rotating effect, the non-rotating models are expected to lose much less mass than their rotating counterpart. Rotation also increases the mixing in the core where it transports more helium to the surface for the rotating solar metallicity model. Due to this reason, larger convective core can be seen in the rotating models. As for the solar non-rotating models less efficient mixing is responsible for the slow starting of He shell burning.

4.8 Fate of very massive stars

In this section, we shall present the fate of very massive stars. As we discuss earlier in this chapter, we want to study which models will end up as PCSN. For this purpose, we have to study and analyse the final and core mass of the models and compare with

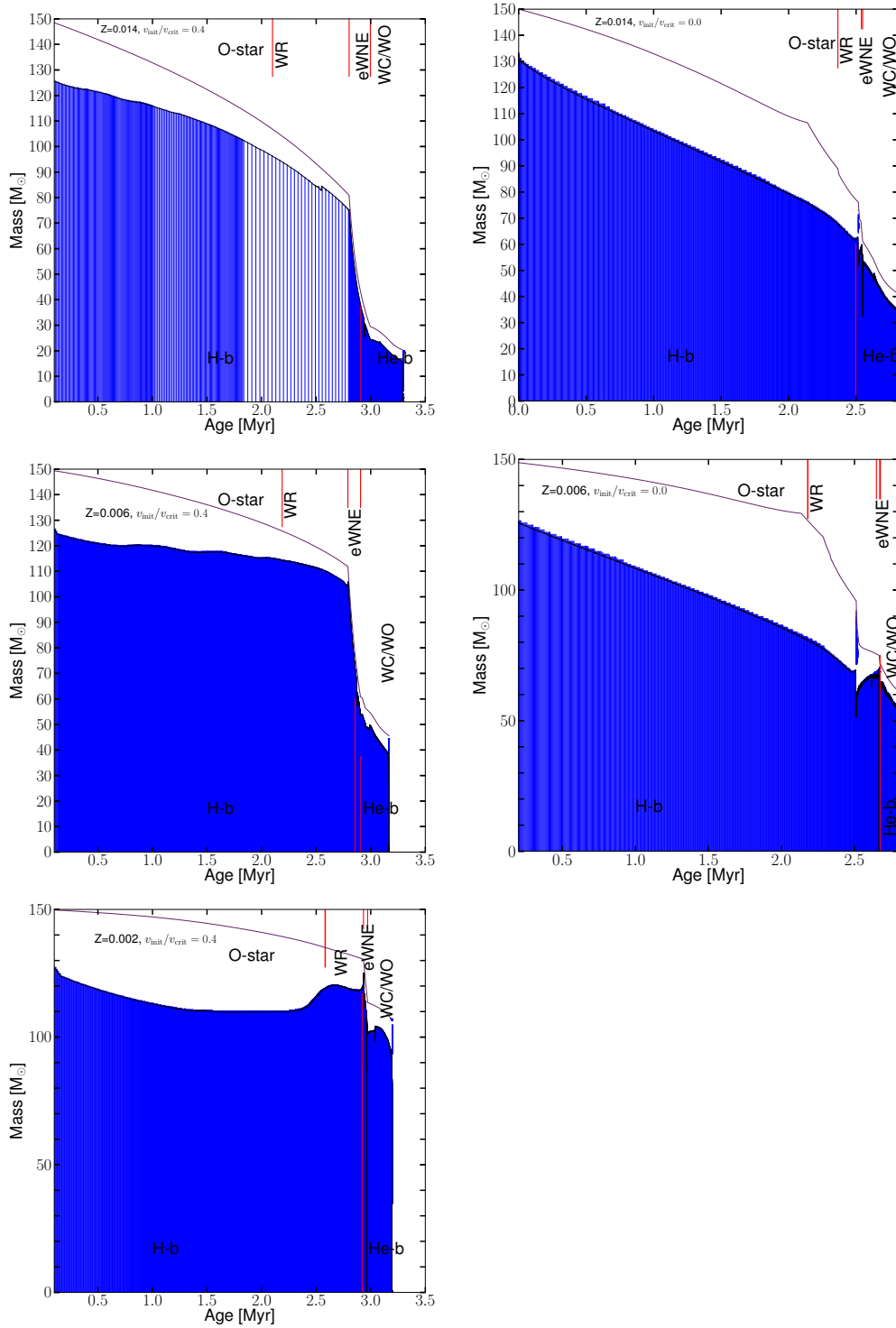


Figure 4.9: Kippenhahn diagrams for non-rotating and rotating $150 M_{\odot}$ model with solar, LMC and SMC metallicities in terms of age. The blue zones represent the convective regions.

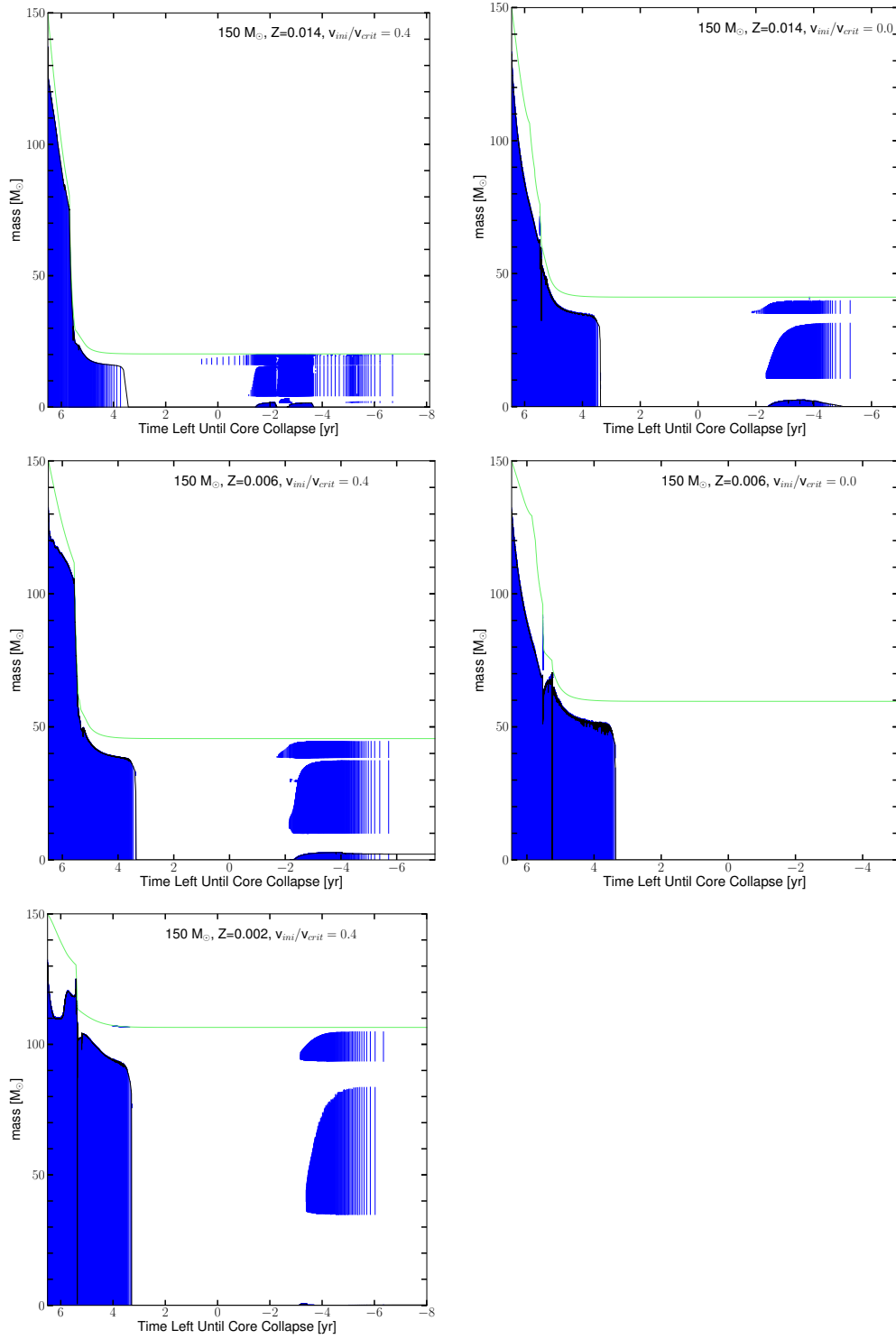


Figure 4.10: Kippenhahn diagrams for non-rotating and rotating $150 M_{\odot}$ model with solar, LMC and SMC metallicities in terms of time before core collapse. The blue zones represent the convective regions.

the values estimated for the PCSN. Factors like rotation induced mixing, mass loss and probably microphysics in the models determine the fate of our models.

4.8.1 Final mass and mass of carbon-oxygen core

Fig. 4.11 shows the final mass of 120, 150, 200, 300 and 500 M_{\odot} models for all metallicities calculated in this work. The 150 and 200 M_{\odot} non-rotating models for solar metallicities have higher final mass due to the lower mass loss than in the rotating models. Since our models have zero hydrogen content, our final mass, M_f is equivalent to the mass of helium core, M_{α} . For the analysis of the fate of very massive stars, we use mass of carbon-oxygen core but as can be seen in Figs. 4.11 and 4.12 they are very similar. M_{α} and M_{co} do not give much difference.

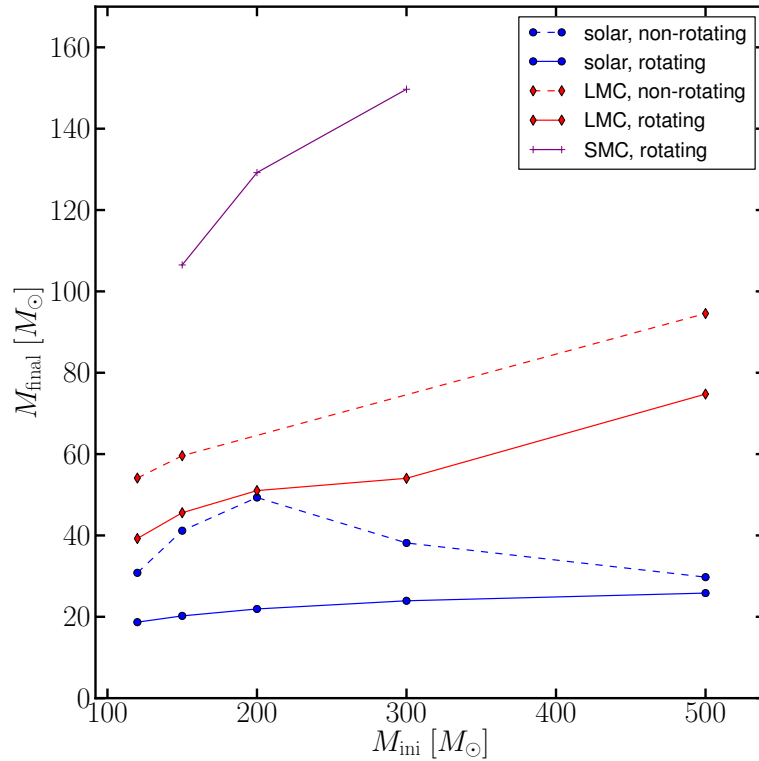


Figure 4.11: Final mass of 120, 150, 200, 300 and 500 M_{\odot} for solar, LMC and SMC metallicities for both rotating and non-rotating models.

We have calculated a series of carbon-oxygen mass from our grid models. In most literature, the fate of massive stars is calculated using the M_α (see Heger & Woosley (2002) for instance). Heger & Woosley (2002) proposed that the M_α should be around $60M_\odot \leq M_\alpha \leq 130M_\odot$. Since there is not much difference between M_α and M_{co} , we use the M_{co} to give more reliable analysis. M_{co} is important for the exploding mechanism for SN2007bi (Yoshida & Umeda, 2011).

In this work, we consider M_α as the mass at the core where the mass of ^4He is higher than 75% while M_{co} is mass at the core where the fraction of mass of carbon plus the oxygen core is greater than 75%. From Fig. 4.12, only four models end their life as PCSN. These are 500 M_\odot LMC metallicity models (both rotating and non-rotating) and 150 and 200 M_\odot SMC metallicity rotating models. Other models end their lives as core-collapse SN and black hole.

The models that end up as PCSN are stars that have very massive initial mass for LMC and the lower end initial mass for SMC. These models experience very small mass loss compared to other models that end up as black hole or core-collapse supernova. Table of the initial mass, total He mass in the envelope, M_{co} , M_{final} and their fate is tabulated in Table 4.6.

4.8.2 Surface He abundance for SNe Ib/Ic

The distinctive feature SNe Ic is the absence of HeI lines in their spectra. However, it is very difficult to distinguish between SNe Ic and Ib since there is no establish theoretical criterion to differentiate them.

The regular standard methods to distinguish SN Ic and Ib are based on total He mass in the envelope (Wellstein & Langer, 1999; Georgy et al., 2009; Yoon et al., 2010) or the He mass fraction at the surface (Yoon et al., 2010).

The first method is based on the total He mass in the envelope. We use the value

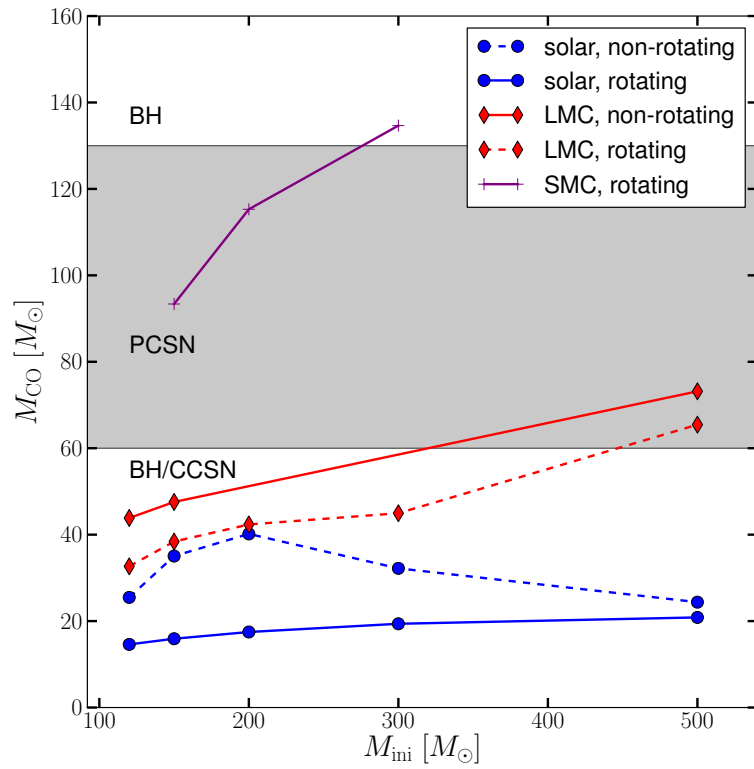


Figure 4.12: Mass of carbon-oxygen core of 120, 150, 200, 300 and 500 M_{\odot} for solar, LMC and SMC metallicities for both rotating and non-rotating models. The shaded area represents the range when the final mass of the models will end up as PCSN.

Table 4.6: Mass range of initial mass, total He envelope, mass of carbon-oxygen core, final mass and the final fate.

M_{ini}	$M_{He_{env}}$	non-rotating			rotating			
		M_{co}	M_{final}	Fate	$M_{He_{env}}$	M_{co}	M_{final}	Fate
Z=0.014								
120	0.4874	25.478	30.8	CCSN/BH	0.5147	18.414	18.7	CCSN/BH
150	0.6142	35.047	41.2	CCSN/BH	0.5053	19.942	20.2	CCSN/BH
200	0.7765	42.781	49.3	CCSN/BH	0.5101	21.601	21.9	CCSN/BH
300	0.3467	32.204	38.2	CCSN/BH	0.4974	19.468	23.9	CCSN/BH
500	0.3119	24.380	29.8	CCSN/BH	0.5675	20.993	25.8	CCSN/BH
Z=0.006								
120	1.2289	43.851	54.2	CCSN/BH	0.5665	32.669	39.2	CCSN/BH
150	1.1041	47.562	59.7	CCSN/BH	0.7845	38.436	45.6	CCSN/BH
200	-	-	-	CCSN/BH	0.5055	42.357	51.0	CCSN/BH
300	-	-	-	CCSN/BH	0.5802	44.959	54.0	CCSN/BH
500	1.6428	92.547	94.7	PCSN	0.7865	73.145	74.8	PCSN
Z=0.002								
150	-	-	-	-	2.3353	93.468	106.5	PCSN
200	-	-	-	-	3.3022	124.329	129.2	PCSN
300	-	-	-	-	5.5018	134.869	149.7	BH

considered in Yoshida & Umeda (2011) where the He envelope mass limit for SN Ib/Ic is between 0.5 and $1.5 M_{\odot}$. For the choice of He mass limit for SN Ic, (Wellstein & Langer, 1999) and (Yoon et al., 2010) it is set at $0.5 M_{\odot}$ while Georgy et al. (2009) proposed $0.6 M_{\odot}$ as their limit. However, Georgy et al. (2009) also reported that the choice of He mass limit between 0.6 and $1.5 M_{\odot}$ hardly affects the mass of main sequence ranges for SN Ib/Ic. Most of our models end up as SN Ic and SN Ib/Ic except for $500 M_{\odot}$ LMC non-rotating models and the SMC models which end up as SN Ib.

The second method is by using the helium surface mass fraction, X_{He}^{surface} . The value of $X_{He}^{\text{surface}} = 0.5$ is set according to Yoshida & Umeda (2011) and Yoon et al. (2010). Yoon et al. (2010) reported that the He lines may not be seen in early time spectra even though the total He mass is as large as $1.0 M_{\odot}$ if He is well mixed with CO material having $X_{He}^{\text{surface}} = 0.5$. Using this criterion, we find that all our models except the SMC models end up as SN Ic. Although there is no clear evidence of very massive stars in low metallicity ending up as SN Ib, our calculation shows models with SMC models are expected to become one.

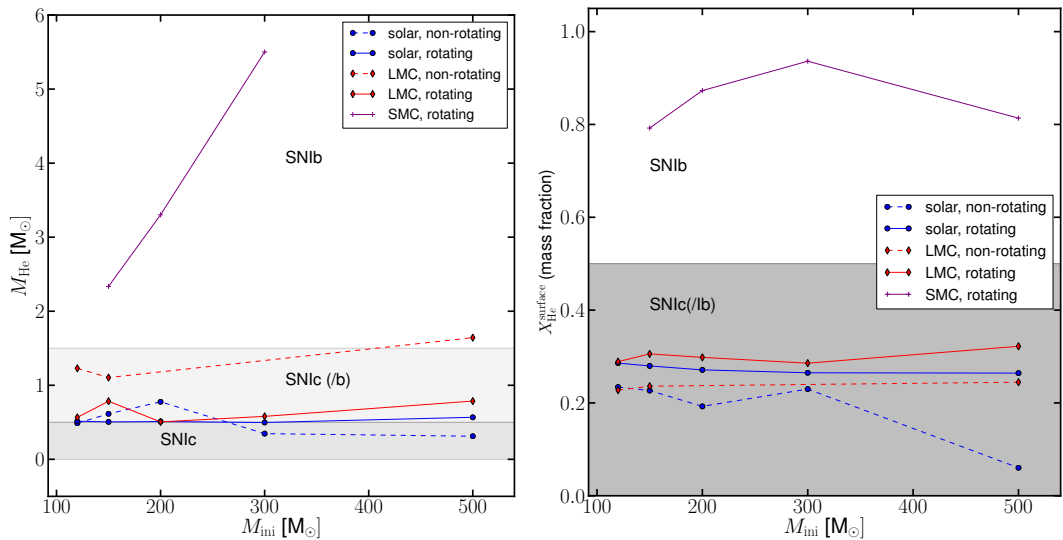


Figure 4.13: Mass of total helium envelope (left) and the mass fraction of He at the surface (right).

4.9 Comparison with the literature

We compare our results with the data obtained from Yoshida & Umeda (2011). In their paper, they computed models with initial mass between 100-500 M_{\odot} using metallicity $Z = 0.004$ which is within the estimated observed metallicity of SN2007bi. In order to compare with our models, we choose case A (standard case) in Yoshida & Umeda (2011) since we have used the standard mass loss prescription in our models. We list out the difference of physics input between our models and Yoshida & Umeda (2011)

1. Heavy elements mixing in Yoshida & Umeda (2011) is from Anders & Grevesse (1989) while our models use the prescription from Asplund et al. (2005).
2. Our models enter WR phase when $X_s = 0.3$ while Yoshida & Umeda (2011) models enter WR phase when $X_s = 0.4$.
3. Our code implements additional mass loss prescription by Gräfener & Hamann (2008) while the code used in Yoshida & Umeda (2011) does not include this mass loss prescription.

4.9.1 Post-main sequence evolution of very massive stars

In Fig. 4.14 we compare our 150 M_{\odot} LMC non-rotating, SMC both rotating and non-rotating evolutionary tracks with 140 M_{\odot} model from Yoshida & Umeda (2011). We do not include the 150 M_{\odot} SMC non-rotating models in our calculation earlier since this model ends at the main sequence phase. We illustrate this model in this figure in order to have a clear understanding of the evolution of the stars with low metallicity.

From the HR track, Yoshida & Umeda (2011) followed the similar pattern with our models except that their model created a loop after the main sequence phase. During this phase, Yoshida & Umeda (2011) model experienced sharp drop in the mass loss while in our models, the mass loss decline slowly compared to Yoshida & Umeda (2011). We

had expected the Yoshida & Umeda (2011) total mass changes slower than our $150 M_{\odot}$ SMC non-rotating model since Yoshida & Umeda (2011) has much higher metallicity. Although we use generally similar mass loss prescriptions, the Yoshida & Umeda (2011) model experienced sharper mass loss episode during the LBV and WR (see top panel of Fig. 4.14).

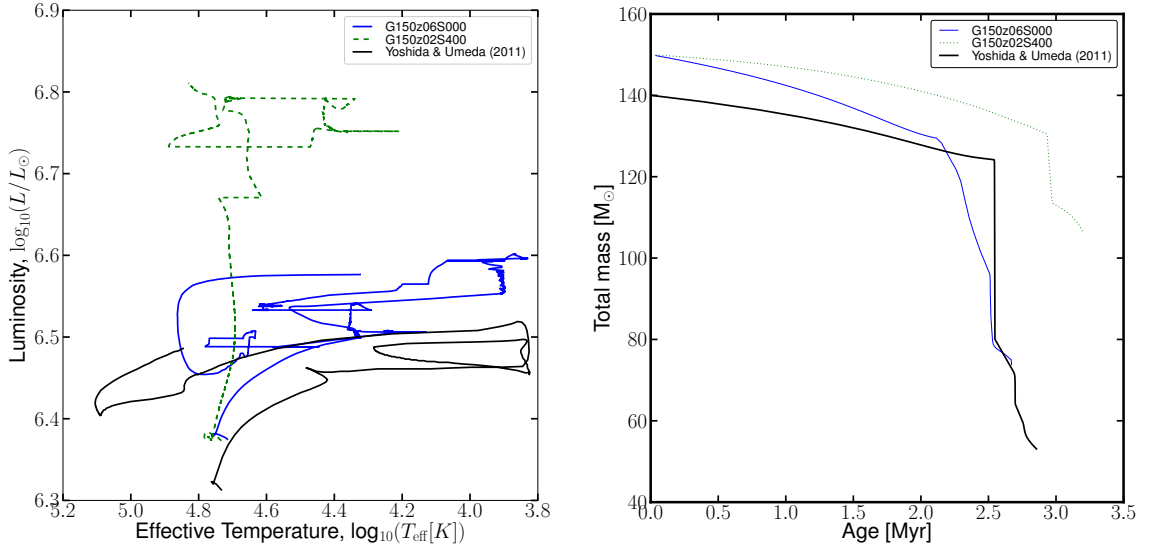


Figure 4.14: Comparison of Yoshida & Umeda (2011) $140 M_{\odot}$ with our $150 M_{\odot}$ with LMC non-rotating and SMC rotating and non-rotating models. Left panel: The HR diagrams of our models and Yoshida & Umeda (2011). The square, circle and triangles symbol represent the entrance of WR phase. Right panel: Comparison of the evolution of mass loss.

4.9.2 Comparison for the fate of very massive stars

In this section, we compare the fate of very massive stars using all the grids for case A in Yoshida & Umeda (2011) with all of our computed models. The comparison figures are shown in Figs. 4.15 and 4.16. We expect the final mass of Yoshida & Umeda (2011) models to lie between our LMC non-rotating and SMC rotating models final mass but instead the models lie below the LMC non-rotating models. This might be due to the different conditions of mass loss prescription as discuss in Section 4.9.1.

Given the values of M_{co} , Yoshida & Umeda (2011) models with initial mass of 300, 400 and 500 M_{\odot} have sufficiently large M_{co} to explode as PCSN. Compared to our models, for metallicity higher than $Z = 0.004$ like LMC only the 500 M_{\odot} retains a large M_{co} .

For the analysis of total He mass envelope and He surface mass fraction, only 100 M_{\odot} Yoshida & Umeda (2011) ended up as SN Ib.

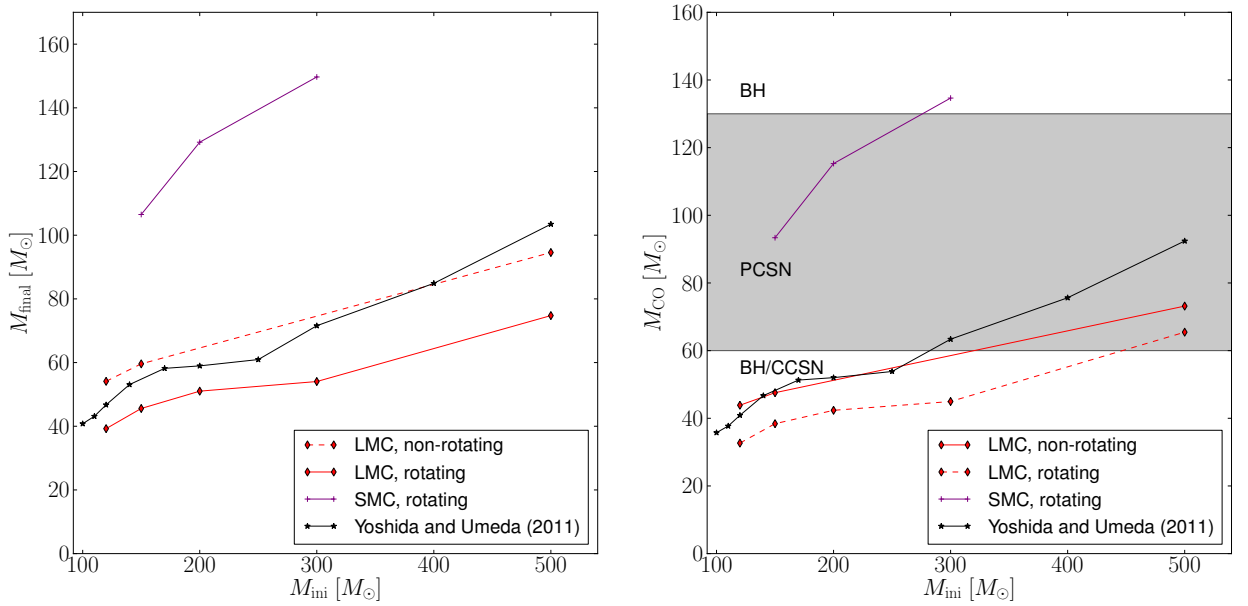


Figure 4.15: Fate comparison of final mass (left) and mass of carbon-oxygen core (right) Yoshida & Umeda (2011) with our models.

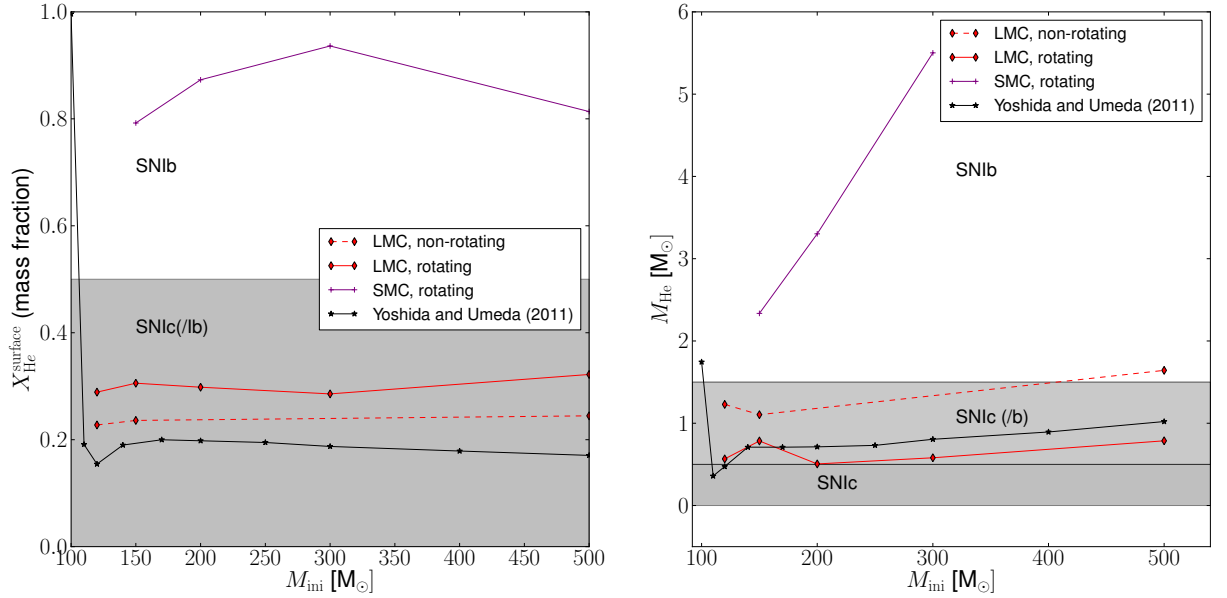


Figure 4.16: Fate comparison of He surface mass fraction (left) and total He mass envelope (right) Yoshida & Umeda (2011) with our models.

4.10 Initial mass range for SN2007bi progenitors

We have evaluated the initial mass range that might produce the PCSN and core collapse SN progenitors by taking into account the M_{co} , total mass of helium envelope, $M_{\text{He}_{\text{env}}}$ and the He surface mass fraction. We do not consider the SN2006gy since this SN is in Type IIIn and all computed models clearly end up as either SN Ic, SN Ib/Ic or SN Ib. We also compare our models with the models from Yoshida & Umeda (2011) as the authors have computed the progenitor for SN2007bi. As suggested in Yoshida & Umeda (2011), the M_{co} for the SN2007bi is around 160-175 M_{\odot} . Two figures of M_{co} with SN2007bi region are provided in Fig. 4.17.

The figure in the upper panel shows all our computed models and we find that the SN2007bi can occur in the rotating SMC metallicity models with initial mass range roughly between 160-175 M_{\odot} . Lower panel in Fig. 4.17 is the comparison between Yoshida & Umeda (2011) with our LMC and SMC models. Yoshida & Umeda (2011) models using the standard mass loss prescription do not explode as SN 2007bi although

their $500 M_{\odot}$ is very near to the lower limit M_{co} range of SN2007bi.

The other models which have either more massive or smaller CO core than SN2007bi M_{co} will the explode as CC SN and form a black hole. From our results, the mass loss plays very important role in determining the fate of very massive stars.

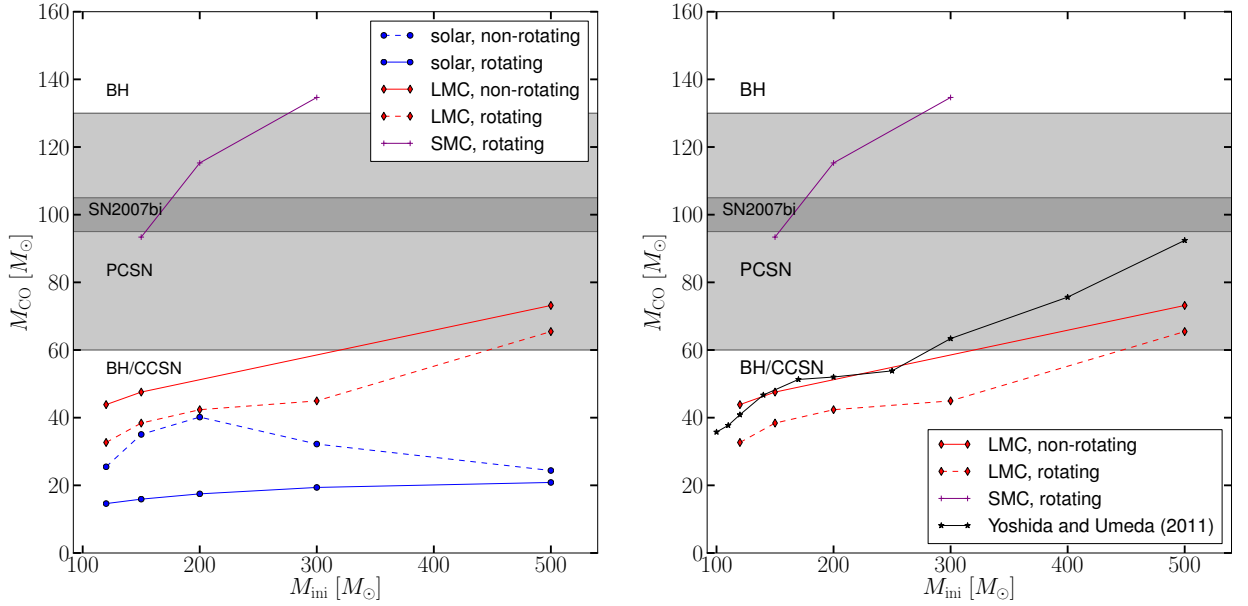


Figure 4.17: Fate comparison of Yoshida & Umeda (2011) with our models.

4.11 Mass loss effect using different mass loss prescriptions

In this section, we study the impact of different mass loss prescriptions. Massive stars particularly at solar metallicity lose a significant amount of mass during their evolution. Mass loss is sensitive to T_{eff} , L and Z . These values change with time during the evolution and the application of different mass loss rates changes the profiles of the models and thus influences their fate. For massive stars, the most extreme mass loss rate is during the WR phase, where the outer layers become chemically enriched and thus modifying

\dot{M} .

In this work, we choose different mass loss prescriptions to estimate the mass loss rate \dot{M} during the WR phase where we investigate the following three cases:

- Case A : Estimated mass loss rate using mass loss prescription by Vink et al. (2001). It gives minimum \dot{M} , with lower mass limit of \dot{M} and upper limit of final mass.
- Case B : Estimated mass loss rate using mass loss prescription by Vink et al. (2001) multiply by a factor 5. This gives WR stars final mass average corresponds to an average of \dot{M} WR star.
- Case C : Estimated mass loss using mass loss prescription by Nugis & Lamers (2000) which is specific for eWNE phase. As seen in Table 4.7, this mass loss rate is extremely high and probably unrealistic to WR. It presents an upper limit of \dot{M} and lower limit for final mass.

These three samples represent the range of the full mass loss that massive stars could experience and therefore we can see the impact of mass loss of the star.

From these cases, we estimate the final mass of the models and investigate the impact of these different mass loss rates towards the fate of the models. The estimated values are presented in Table 4.7. The first part of the table represents the mass of the star at various WR stages from our models, part two represents the mass loss estimate and final mass of Case A, part three represents mass loss estimate and final mass of Case B, part four for mass loss estimate and final mass of eWNE and finally part five the mass loss rate obtained directly from the models at final stage of eWNE phase.

For Case A, we estimate the mass loss rate $\langle \dot{M} \rangle$ as:

$$\langle \dot{M}_{Vink} \rangle = \frac{M_{ini} - M_{Y_H(0.3)}}{\text{Age}_{Y_H(0.3)}} \quad (4.3)$$

while for Case B:

$$\langle \dot{M}_{Vink5} \rangle = \left(\frac{M_{ini} - M_{Y_H(0.3)}}{\text{Age}_{Y_H(0.3)}} \right) \times 5 \quad (4.4)$$

and for Case C:

$$\langle \dot{M}_{eWNE} \rangle = \frac{M_{H(0.05)} - M_{Y_{C+O/He(0.03)}}}{(\text{Age}_{Y_H(0.05)} - \text{Age}_{Y_H(0.3)})}. \quad (4.5)$$

In the last column in Table 4.7, we provide the values of mass loss from our stellar evolution models at the end of eWNE phase. These values are given for comparison. From the values tabulated in Table 4.7, we find that $\langle \dot{M}_{Vink} \rangle$ (Case A) is lower than the WR estimated mass loss rate (Case C). Vink et al. (2001) mass loss prescription is computed for O-B stars which is more suitable during the main-sequence stage and it underestimates the mass loss rate during the advanced stages. To give a more reasonable estimate, we multiply the values from Case A by a factor of five. This will give an average value of WR mass loss. From the table (c.f Case B, $\langle \dot{M}_{Vink5} \rangle$), these values give more reasonable final mass values closer to the estimated values using Nugis & Lamers (2000) mass loss prescription, $\langle \dot{M}_{eWNE} \rangle$ (Case C) and mass loss from our stellar models. However, the estimate for $\langle \dot{M}_{eWNE} \rangle$ is very high compare to Case A, Case B and mass loss from our stellar models which might overestimate the mass loss of the models.

From the estimated mass loss rate values, we list the summaries of the results:

- $\langle \dot{M}_{Vink} \rangle$: Give minimum mass loss rate during the evolution since it underestimates the value for mass loss rate of WR star.
- $\langle \dot{M}_{Vink5} \rangle$: This rate gives reasonable value for the mass loss during WR phase. which is higher than the mass loss rate estimated by $\langle \dot{M}_{Vink} \rangle$.
- $\langle \dot{M}_{eWNE} \rangle$: This estimate gives stronger mass loss rate during the WR phase. The value is so high ($\geq 10^{-3}$) it is probably unrealistic.
- \dot{M}_{eWNE_f} : This mass loss rate is from our stellar models. Most of these values are lower than $\langle \dot{M}_{eWNE} \rangle$. This is because these value are taken at the final stage of

eWNE after the models have already loss a lot of mass and thus have smaller mass loss rate.

The effect of different implementation of the mass loss rates can be seen from their final mass. Low mass loss rate will produce higher final mass. This can affect the fate of the models itself when different mass loss rates are applied in the models during the evolution. To calculate the estimated final mass, we use the following equations:

- Case A:

$$M_{f(\text{Vink})} = M(Y_H(0.05)) - \langle \dot{M}_{\text{Vink}} \rangle \times t_{\text{left}}. \quad (4.6)$$

- Case B:

$$M_{f(\text{Vink5})} = M(Y_H(0.05)) - \langle \dot{M}_{\text{Vink5}} \rangle \times t_{\text{left}}. \quad (4.7)$$

- Case C:

$$M_{f(\text{eWNE})} = M(\text{eWNE}) - \langle \dot{M}_{\text{eWNE}} \rangle \times t_{\text{left}}. \quad (4.8)$$

M_{eWNE} is the mass of the star when it enters eWNE phase i.e when $\frac{C+O}{He} > 0.03$ at the surface and t_{left} is the time before core collapse in years.

The final mass of our models and estimated final mass for Case A and Case B are shown in Fig. 4.18. Case C is not plotted since we obtain negative values for the estimated final mass except for the 120 M_{\odot} LMC non-rotating model. For the $\langle \dot{M}_{\text{Vink5}} \rangle$ (Case A), since the mass loss is low, we expect less mass is ejected during the evolution. This is also shown in the figure where even in the solar metallicity models, the final mass is extremely large and one can expect to have PCSN at this metallicity. For Case B, the models still retain large amount of final mass but not as high as in Case A. The PCSN is expected for LMC metallicity models for this case. Finally, the lower panel shows the full stellar models final mass.

Comparing with all these estimated final mass, for Case A, most of the models in-

cluding solar, LMC and SMC retain enough mass to end as PCSN. Case B has similar pattern with our full models and it has higher final mass at LMC and SMC with rotation. This is due to the higher mass loss rate estimated for this case compared with the mass loss rate from the models. For Case C since most of the values are negative and they are expected to end up as core collapse SN.

By using the different mass loss rates, we can see how it can affect the final mass and the fate of the models itself. To summarise, we list the important points:

- Case A : $\langle \dot{M}_{Vink} \rangle$ represents the minimum mass loss rate compared to other mass loss rates. By using this mass loss rate, we probably underestimate the mass loss rate during the WR phase. Lower mass loss rate using this prescription gives higher final mass even in the solar metallicity models (both rotating and non-rotating models). Since its final mass is extremely high, PCSN can be expected even from solar metallicity models.
- Case B : $\langle \dot{M}_{Vink5} \rangle$ represents a reasonable mass loss rate for WR stars. The final mass for this case has the same pattern with the final mass loss from our full stellar models. This mass loss rate is able to produce PCSN at lower mass range for the LMC rotating models.
- Case C: $\langle \dot{M}_{eWNE} \rangle$ is the mass loss rate using mass loss prescription for eWNE stars from Nugis & Lamers (2000). This mass loss rate overestimates the mass loss during the WR phase and is much higher than the observed mass loss (c.f last column of Table 4.7 and see for example Crowther et al. (2010)). The final mass using this estimate gives negative values which shows that all the models will end up only as CCSN and no PCSN is expected if such higher mass loss would occur in stars.

Finally, we can conclude that the fate of the models are very sensitive to different

mass loss prescriptions. By varying the mass loss rates between the minimum and maximum mass loss expected in massive stars, we can see that the fate of the stars changes drastically. It is therefore crucial to develop reliable mass loss prescription to predict the fate of the most massive stars.

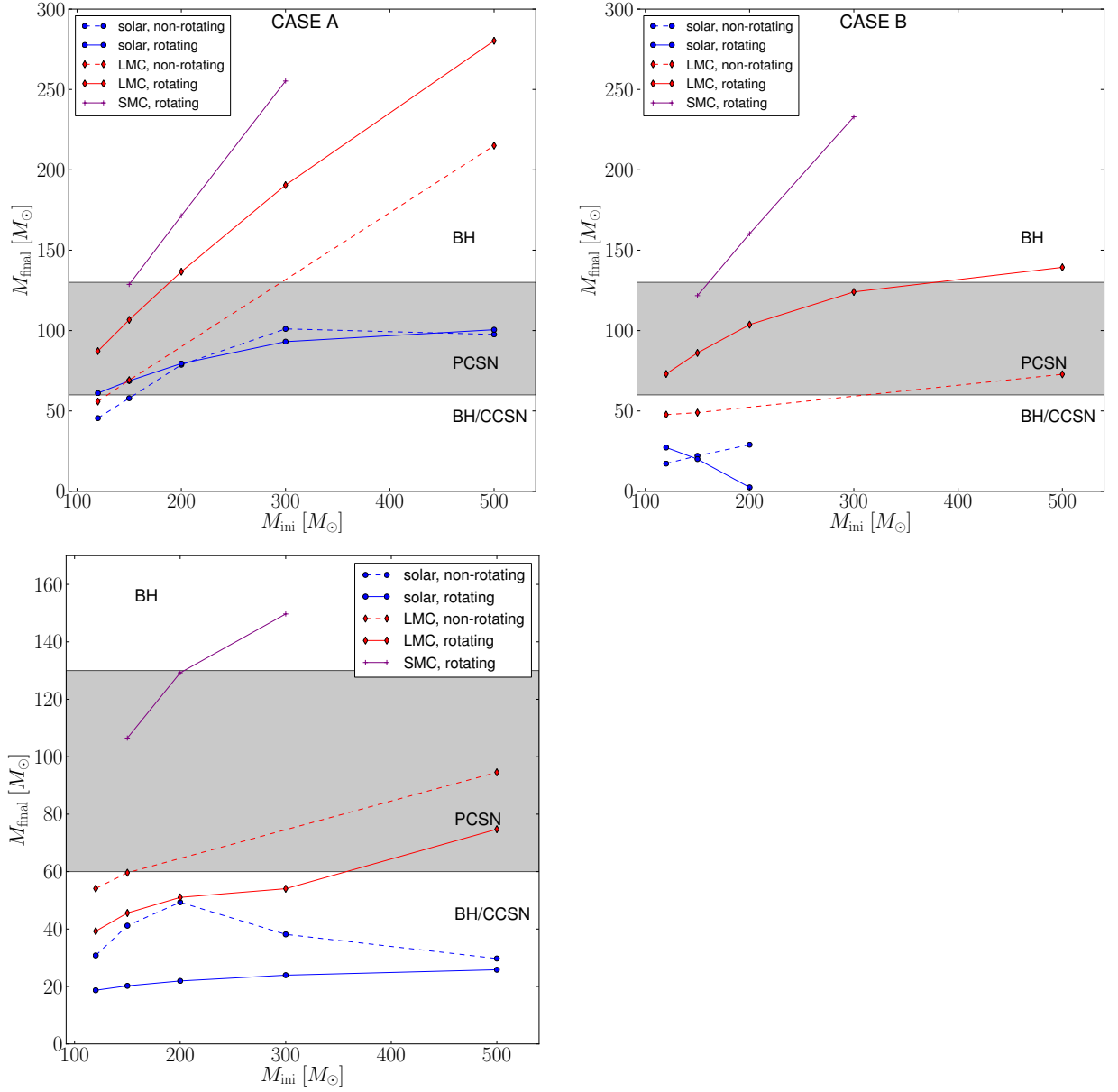


Figure 4.18: Estimated final mass for Case A and Case B at the upper panel. Lower panel shows the final mass from our full stellar models.

Table 4.7: Total mass estimates of the models using different mass loss rates. The table is divided into 5 parts: Total mass of the models at various stages of WR phase, Case A and Case B. In each case, we provide the mass loss rate and the final mass. The unit for $\langle \dot{M} \rangle$ is in M_{\odot}/year and $\langle M_f \rangle$ is M_{\odot} .

M_{ini}	Total mass of the models				Case A		Case B		Case C		Case D
	$Y_{\text{H}(0.3)}$	$Y_{\text{H}(0.05)}$	eWNE _f	Final	$\langle \dot{M}_{\text{Vink}} \rangle$	$\langle M_{\text{fVink}} \rangle$	$\langle \dot{M}_{\text{Vink5}} \rangle$	$\langle M_{\text{fVink5}} \rangle$	$\langle \dot{M}_{\text{eWNE}} \rangle$	$\langle M_{\text{feWNE}} \rangle$	\dot{M}_{eWNE}
Z=0.014, $v/v_{\text{crit}} = 0.0$											
120	69.43	52.59	47.62	30.81	2.477e-05	45.52	1.239e-04	17.26	3.638e-04	-56.14	3.148e-04
150	88.86	66.87	61.20	41.16	3.274e-05	57.90	1.637e-04	22.06	6.107e-04	-105.93	5.236e-04
200	121.06	91.20	83.85	49.32	4.618e-05	78.76	2.309e-04	29.00	1.150e-03	-225.98	3.524e-03
300	184.27	130.47	52.05	38.15	8.047e-05	101.05	4.023e-04	-16.66	8.912e-04	-273.88	3.548e-04
500	298.79	169.50	45.14	29.75	1.736e-04	97.60	8.680e-04	-190.00	9.590e-04	-352.07	2.655e-04
Z=0.014, $v/v_{\text{crit}} = 0.4$											
120	88.28	69.54	27.43	18.68	1.675e-05	61.08	8.375e-05	27.25	2.057e-04	-76.45	8.395e-05
150	106.64	80.88	29.49	20.22	2.467e-05	68.71	1.233e-04	20.04	2.640e-04	-100.75	9.954e-05
200	137.52	98.75	31.84	21.93	3.985e-05	79.49	1.992e-04	2.45	3.564e-04	-140.44	1.189e-04
300	196.64	129.10	34.45	23.93	7.559e-05	93.10	3.780e-04	-50.91	5.160e-04	-211.29	1.422e-04
500	298.42	174.05	38.30	25.83	1.594e-04	100.53	7.969e-04	-193.55	7.901e-04	-326.16	1.811e-04
Z=0.006, $v/v_{\text{crit}} = 0.0$											
120	74.30	57.91	56.91	54.11	2.140e-05	55.87	1.070e-04	47.71	3.272e-04	25.73	3.020e-04
150	94.18	74.20	71.75	59.59	2.839e-05	69.15	1.419e-04	48.96	5.038e-04	-17.80	4.560e-04
500	332.68	250.64	197.41	94.56	1.304e-04	215.07	6.521e-04	72.81	3.334e-03	-711.77	2.818e-03
Z=0.006, $v/v_{\text{crit}} = 0.4$											
120	100.57	90.78	54.43	39.25	9.429e-06	87.23	4.715e-05	73.03	3.219e-04	-66.74	2.000e-04
150	125.79	111.84	60.75	45.58	1.367e-05	106.69	6.836e-05	86.09	4.418e-04	-105.67	2.518e-04
200	166.81	144.86	66.25	51.02	2.180e-05	136.62	1.090e-04	103.68	6.257e-04	-170.12	3.034e-04
300	247.07	207.10	73.11	54.04	4.166e-05	190.49	2.083e-04	124.05	9.524e-04	-306.63	3.698e-04
500	397.34	315.51	86.10	74.75	9.194e-05	280.28	4.597e-04	139.34	1.685e-03	-559.56	5.129e-04
Z=0.002, $v/v_{\text{crit}} = 0.4$											
150	135.06	130.46	113.51	106.50	6.661e-06	128.71	3.331e-05	121.72	4.485e-04	-4.12	4.217e-04
200	181.42	174.18	137.90	129.21	9.902e-06	171.39	4.951e-05	160.24	6.631e-04	-48.76	5.152e-04
300	273.18	260.81	156.14	149.70	1.730e-05	255.24	8.650e-05	232.97	1.040e-03	-178.71	6.668e-04

4.12 Summary

We have calculated a grids of stellar models of very massive stars in SMC, LMC and solar metallicities. Our study is motivated by the finding of a very massive star known to date, R136a1 (Crowther et al., 2010) and the observation of PCSN candidate, SN2007bi by (Gal-Yam et al., 2009).

Our stellar evolution models in the main sequence shows that they match the observations of NGC3603 and R136 stars (Crowther et al., 2010). From the main sequence, we evolve the models further until at least the end of He burning. Models evolve using the standard mass loss prescriptions are predicted to end up as PCSN are models at LMC metallicity with mass around $500 M_{\odot}$ and rotating SMC metallicity models with mass $120 < M_{\odot} < 280$. Other than that it will die as a black hole or core-collapse supernova. We also explore the probability of PCSN candidate, the SN2007bi to occur in our models. From our analysis, our models predict SN2007bi will only occur at around $150 < M_{\odot} < 175$ at rotating SMC metallicity.

Finally we estimate the mass loss using different mass loss rates. There are uncertainties in using the correct mass loss prescriptions and by varying different mass loss prescriptions during the transition of WR, the models give different conclusions for their fate. We find that Vink et al. (2001) mass loss prescription if implemented in the models, gives higher final mass compared to models using mass loss prescriptions by Nugis & Lamers (2000) or Gräfener & Hamann (2008). This will change the fate of the stars where PCSN can occur even in solar metallicity with smaller mass lower than $300 M_{\odot}$.

Chapter 5

Neutrino Energy Loss in Massive Stars

5.1 Neutrino loss in massive stars

In the evolution of stars, there are six major burning stages: hydrogen burning, helium burning, carbon burning, neon burning, oxygen burning and silicon burning. During H and He-burnings, the star loses its energy by radiation while during the four last stages, neutrinos dominate the energy loss. Thus, the neutrino cooling rate is important especially during the late stages of the evolution of the star since most of the energy lost is through the neutrino processes. When the star evolves, the temperature and density increase with time; the rate of neutrino energy loss becomes higher since the neutrino processes depend on the temperature and density of the interior of the star.

Itoh and his collaborators have studied the interior neutrino energy loss based on Salam-Weinberg theory (Itoh & Kohyama, 1983; Itoh et al., 1984; Munakata et al., 1985, 1987; Itoh et al., 1989, 1992, 1993; Kohyama et al., 1993, 1994). The neutrino energy loss mechanisms that they studied were pair, photo, plasma, bremsstrahlung and recombination neutrino processes.

There are also calculations on neutrino energy loss done by Dicus et al. (1976); Schinder et al. (1987); Braaten (1991); Braaten & Segel (1993); Haft et al. (1994) using the

same Salam-Weinberg theory. The older calculations based on Feynman-Gell-Mann theory were summarised by Beaudet et al. (1967).

The four most important neutrino processes in a star are the following:

- pair neutrino : $e^+ + e^- \rightarrow \nu + \bar{\nu}$
- photoneutrino : $\gamma + e^\pm \rightarrow e^\pm + \nu + \bar{\nu}$
- plasma neutrino : $\gamma^* \rightarrow \nu + \bar{\nu}$
- bremsstrahlung : $e^\pm + Z \rightarrow \nu + \bar{\nu}$

Each neutrino process gives rise to a dominant contribution in different regions of the density and temperature diagram. We shall discuss in detail each of the neutrino processes in the next subsections. In recent years, there are new additional neutrino processes considered important in the stellar evolution which are the recombination process (Itoh et al., 1996) and neutrino energy loss for ^{55}Co (Nabi & Sajjad, 2008). Esposito et al. (2003) calculated the neutrino energy loss of all four neutrino processes mentioned in the list above with the inclusion of radiative correction in the Hamiltonian.

The current Geneva stellar evolution code uses the treatment from Itoh et al. (1989) for pair, photo and plasma neutrino processes and Dicus et al. (1976) for bremsstrahlung process. In this work our aim is to update the Geneva stellar evolution code using Itoh et al. (1996) where the plasma and bremsstrahlung neutrino processes will be modified accordingly. Although there are several papers (see for eg. Esposito et al. (2003)) describing the neutrino energy loss, we find Itoh et al. (1996) give the analytical fitting formulae that are most convenient to implement in a stellar evolution code.

5.2 Neutrino Processes

During H-burning, for every helium nucleus produced one needs to convert two protons into two neutrons, so inevitably two neutrinos with MeV-range energies emerge. Advanced

burning stages consist essentially of combining α particles to form larger nuclei and do not produce neutrinos in nuclear reactions. However, neutrinos are still produced by several thermal processes which actually dominate the stellar energy losses from carbon burning and in the more advanced phases.

Thermal neutrino emission arises from processes involving electrons, nuclei and photons of the medium and is based on the neutrino interaction with electrons. According to the theory of weak interactions, for each electron process emitting a photon, there is a finite probability $P(\nu_e\bar{\nu}_e)$ of emitting a $\nu_e\bar{\nu}_e$ pair with energy E_ν . The ratio of this probability to that of emitting a photon P_γ is given by

$$\frac{P(\nu_e\bar{\nu}_e)}{P_\gamma} = \frac{G}{\alpha^4} \left(\frac{E_\nu}{m_e c^2} \right)^4 \simeq 3 \times 10^{-18} \left(\frac{E_\nu}{m_e c^2} \right)^4 \quad (5.1)$$

where $G \approx 10^{-5}(m_e/m_\mu)^2 = 3 \times 10^{-12}$ is the constant characterising the ratio of weak and electromagnetic interactions and α is the fine structure constant with value $1/137$. Eq. 5.1 shows that the neutrino emission may occur without nuclear reactions. Neutrino emissions constitute a means of losing energy from the stellar interior and is known as neutrino cooling. The neutrino cooling occurs only when T or ρ of the star is high enough. This process is dominant at the start of C-burning process where the $T > 2 \times 10^8$ K and $\rho > 10^3 \text{ gcm}^{-3}$.

During the evolution of massive stars, when carbon burning starts in the core, the rate of energy release by neutrinos begins to compete with the rate of the convective energy transport. The total energy loss caused by the neutrino emission is the sum of all neutrino processes and it can be written as

$$Q_{tot}(\text{ergcm}^{-3}\text{s}^{-1}) = Q_{pair} + Q_{photo} + Q_{plas} + Q_{brems} + Q_{recomb} \quad (5.2)$$

where Q_{pair} is the energy loss from pair neutrino production, Q_{photo} is the energy loss from

the photoneutrino production, Q_{plas} is the energy loss from plasma neutrino production, Q_{brems} is the energy loss from bremsstrahlung and Q_{recomb} is the energy loss from the recombination process.

In the subsection below, we list out the processes that are used in the code and the formulation of the energy loss for each process. Details of the formulation can be found in Itoh et al. (1996).

5.2.1 Pair neutrino process

The pair annihilation process (Fig. 5.1) becomes dominant at temperature higher than 10^9 K. In Itoh et al. (1996), the energy loss from the pair process can be written as

$$Q_{pair} = \frac{1}{2}[C_V^2 + C_A^2] + N(C_V'^2 + C_A'^2)]Q_{pair}^+ + \frac{1}{2}[C_V^2 - C_A^2] + N(C_V'^2 - C_A'^2)]Q_{pair}^- \quad (5.3)$$

where $C_V = \frac{1}{2} + 2 \sin^2 \theta_w$, $C_A = \frac{1}{2}$, $C_V' = 1 - C_V$, $C_A' = 1 - C_A$ and $\sin^2 \theta_w = 0.2319 \pm 0.0005$. The value of θ_w is the Weinberg angle and n is the number of neutrino flavors other than electron neutrino. This expression is the same as in Itoh et al. (1989) and Munakata et al. (1985). Itoh et al. (1996) provides an analytical fitting formula and also numerical table.

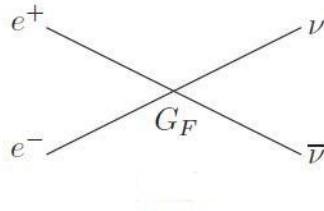


Figure 5.1: Feynman diagram of pair-annihilation neutrino process where G_F is the Fermi coupling constant.

5.2.2 Photoneutrino process

This type of emission process is strongest at low density and temperature below 10^9 K. The Feynman diagram of the photo production process is shown in Fig. 5.2 . The formulation of photoneutrino process can be written as

$$Q_{photo} = \frac{1}{2}[C_V^2 + C_A^2] + N(C_V'^2 + C_A'^2)]Q_{photo}^+ + \frac{1}{2}[C_V^2 - C_A^2] + N(C_V'^2 - C_A'^2)]Q_{photo}^-. \quad (5.4)$$

The values of C_A , C_V , C_A' and C_V' are the same as in the pair neutrino formulation. The calculation in Itoh et al. (1989) superseded the calculation done by Munakata et al. (1985) and Schinder et al. (1987).

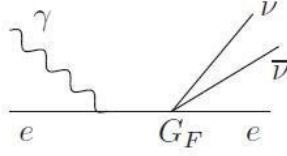


Figure 5.2: Feynman diagram of photo neutrino process.

5.2.3 Plasma neutrino process

Plasma neutrino process is the decay of photons and plasmons into neutrino-antineutrino pairs. The formulation of plasma neutrino energy loss rate can be written as

$$Q_{plasma} = (C_V^2 + nC_V'^2)Q_V, \quad (5.5)$$

$$Q_V = Q_L + Q_T \quad (5.6)$$

where Q_L and Q_T are the contributions of the longitudinal plasmon and transverse plasmon respectively. The plasma neutrino process in Itoh et al. (1996) was taken from

Kohyama et al. (1994) and updated using Haft et al. (1994). The Feynman diagram for the plasma process is shown in Fig. 5.3.

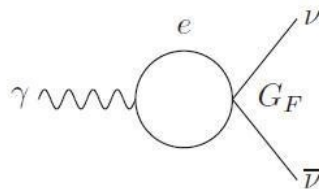


Figure 5.3: Feynman diagram of plasma neutrino process.

5.2.4 Bremsstrahlung neutrino process

Neutrino bremsstrahlung process is dominant at high density but relatively low temperature. The bremsstrahlung neutrino process in Itoh et al. (1996) supersedes the calculation done by Dicus et al. (1976) through the accurate inclusion of the ionic correlation effects and the screening effects attributable to electrons. Dicus et al. (1976) calculated the bremsstrahlung process in the framework of Weinberg-Salam theory but did not cover a wide density-temperature region and this makes their calculation not suitable for the stellar evolution computation.

For the bremsstrahlung neutrino energy process, the process involves different temperature-density region. The temperature-density region is divided into two by the line $T = 0.3T_F$ where T_F is the electron Fermi temperature (Itoh et al., 1996). When $T > 0.3T_F$, the electrons are weakly degenerate and when $T < 0.3T_F$, the electrons become strongly degenerate. The weakly degenerate electrons in the bremsstrahlung

neutrino energy loss can be written as

$$\begin{aligned}
Q_{gas} &= 0.5738(\text{ergcm}^{-3}\text{s}^{-1}) \sum_{i=1} (X_i Z_i / A_i) T_8^6 \rho \\
&\times \{1/2[(C_V^2 + C_A^2) + n(C_V'^2 + C_A'^2)] F_{gas} \\
&- 1/2[(C_V^2 - C_A^2) + n(C_V'^2 - C_A'^2)] G_{gas}\} \tag{5.7}
\end{aligned}$$

For strongly degenerate region, the process can be divided into liquid metal phase and crystalline lattice phase depending on the strength of the ionic correlation, Γ . Here we list out the formulation of each process in the case of strong degeneracy.

- Liquid Metal Phase

$$\begin{aligned}
Q_{liquid} &= 0.5738(\text{ergcm}^{-3}\text{s}^{-1}) T_8^6 \rho [\sum_{i=1} (X_i Z_i / A_i) \\
&\times \{1/2[(C_V^2 + C_A^2) + n(C_V'^2 + C_A'^2)] F_{liquid}(\Gamma_i) \\
&- 1/2[(C_V^2 - C_A^2) + n(C_V'^2 - C_A'^2)] G_{liquid}(\Gamma_i)\}] \tag{5.8}
\end{aligned}$$

- Crystalline Lattice Phase

$$Q_{crystal} = Q_{lattice} + Q_{phonon} \tag{5.9}$$

where

$$\begin{aligned}
Q_{lattice} &= 0.5738(\text{ergcm}^{-3}\text{s}^{-1}) T_8^6 \rho [\sum_{i=1} (X_i Z_i / A_i) f_{band} \\
&\times \{1/2[(C_V^2 + C_A^2) + n(C_V'^2 + C_A'^2)] F_{lattice}(\Gamma_i) \\
&- 1/2[(C_V^2 - C_A^2) + n(C_V'^2 - C_A'^2)] G_{lattice}(\Gamma_i)\}] \tag{5.10}
\end{aligned}$$

and

$$\begin{aligned}
Q_{phonon} &= 0.5738(\text{ergcm}^{-3}\text{s}^{-1})T_8^6[\sum_{i=1}^{\infty}(X_iZ_i/A_i) \\
&\times\{1/2[(C_V^2 + C_A^2) + n(C_V'^2 + C_A'^2)]F_{phonon}(\Gamma_i) \\
&-1/2[(C_V^2 - C_A^2) + n(C_V'^2 - C_A'^2)]G_{phonon}(\Gamma_i)\}] \quad (5.11)
\end{aligned}$$

The summations in Eq. 5.8, 5.9, 5.10 and 5.11 are over the elements tabulated in Itoh et al. (1996).

5.3 Numerical aspect

Geneva code employs Henyey method (Henyey et al., 1964) to solve the system of differential equations describing the stellar structure leading to the spatial solutions in Lagrangian coordinate. The total neutrino energy, ϵ_ν ($\text{erg g}^{-1} \text{s}^{-1}$) is needed at each mass shell in which values of the various neutrino energy loss processes are computed directly from the analytical fitting formulae described by Itoh et al. (1996). In the implementation of the Henyey discretisation process, the partial derivatives of the total neutrino energy with respect to the temperature T and pressure P and in turn the individual neutrino processes are needed. Terms of the form $\frac{\partial \ln \epsilon_\nu}{\partial \ln T}$ and $\frac{\partial \ln \epsilon_\nu}{\partial \ln P}$ which together with ϵ_ν form the major output from the neutrino code. Since the energy loss is a function of temperature and density, $\epsilon_\nu = \epsilon_\nu(\rho, T)$ we derive these derivatives from the fitting formulae given by Itoh et al. (1996). Thus the change in the neutrino energy loss is written as

$$\Delta \epsilon_\nu = \frac{\partial \epsilon_\nu}{\partial T} T + \frac{\partial \epsilon_\nu}{\partial P} dP \quad (5.12)$$

where the change in the neutrino energy loss due to the temperature alone is the sum of all the neutrino energy sources:

$$\frac{\partial \epsilon_\nu}{\partial T} = \frac{\partial \epsilon_\nu^{pair}}{\partial T} + \frac{\partial \epsilon_\nu^{photo}}{\partial T} + \frac{\partial \epsilon_\nu^{plas}}{\partial T} + \frac{\partial \epsilon_\nu^{brems}}{\partial T}. \quad (5.13)$$

Likewise the changes in ϵ_ν due to pressure dependence is

$$\frac{\partial \epsilon_\nu}{\partial P} = \frac{\partial \epsilon_\nu^{pair}}{\partial P} + \frac{\partial \epsilon_\nu^{photo}}{\partial P} + \frac{\partial \epsilon_\nu^{plas}}{\partial P} + \frac{\partial \epsilon_\nu^{brems}}{\partial P}. \quad (5.14)$$

These are then converted to the form $\frac{\partial \ln \epsilon_\nu}{\partial \ln T}$ and $\frac{\partial \ln \epsilon_\nu}{\partial \ln P}$ by using the thermodynamic variables, $\frac{\partial \ln \rho}{\partial \ln T}$ and $\frac{\partial \ln \rho}{\partial \ln P}$.

5.4 Neutrino energy losses for 20, 60 and 120 M_\odot solar metallicity models

In this section, we shall present some results from evolution of very massive stars using the updated neutrino energy loss from Itoh et al. (1996). In the current Geneva stellar evolution code, the neutrino energy loss processes are taken from Itoh et al. (1989) and Dicus et al. (1976). For this work, we evolve only non-rotating models to show the pertinent changes in the evolution due to the updated neutrino energy loss. All models are evolved at least until the middle of O-burning.

5.4.1 HR diagram

Figure 5.4 shows the HR diagram of both models using the neutrino energy loss from Itoh et al. (1996) and from Itoh et al. (1989). The solid lines represent the models using the updated neutrino energy loss while the dotted lines are the models using the old neutrino energy loss prescription.

In the evolution of the HR diagram, all models give agreeable tracks. The 120 M_\odot models have slight changes in the tracks when these models reach the end of the evolution.

These changes are not related to neutrino losses but to slightly different evolutionary paths.

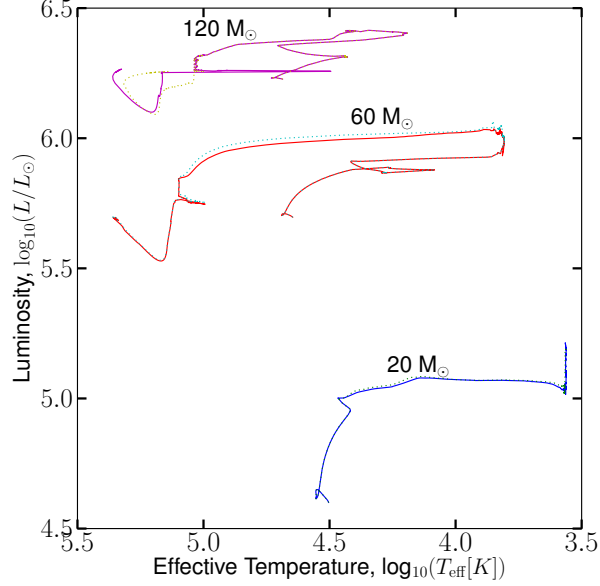


Figure 5.4: HR diagram of 20, 60 and 120 M_{\odot} models.

5.4.2 Internal evolution

The evolution in the T_c - ρ_c diagram for all models is presented in Fig. 5.5. The T_c - ρ_c diagram using both neutrino energy loss prescriptions give agreeable tracks. However, we find that in 20 M_{\odot} models, the T_c - ρ_c diagram using Itoh et al. (1996) gives lower values compared to models using Itoh et al. (1989). Since at this point, the neutrino energy loss starts dominating the energy loss in the star, we are going to study which process affects these changes. From the models, the lower mass model appears to be more sensitive towards the neutrino cooling compared with higher mass models.

5.4.3 Comparison of neutrino energy loss

In this section, we study the comparison of neutrino energy loss using Itoh et al. (1996) and Itoh et al. (1989) with respect to the internal structure of the models. During carbon

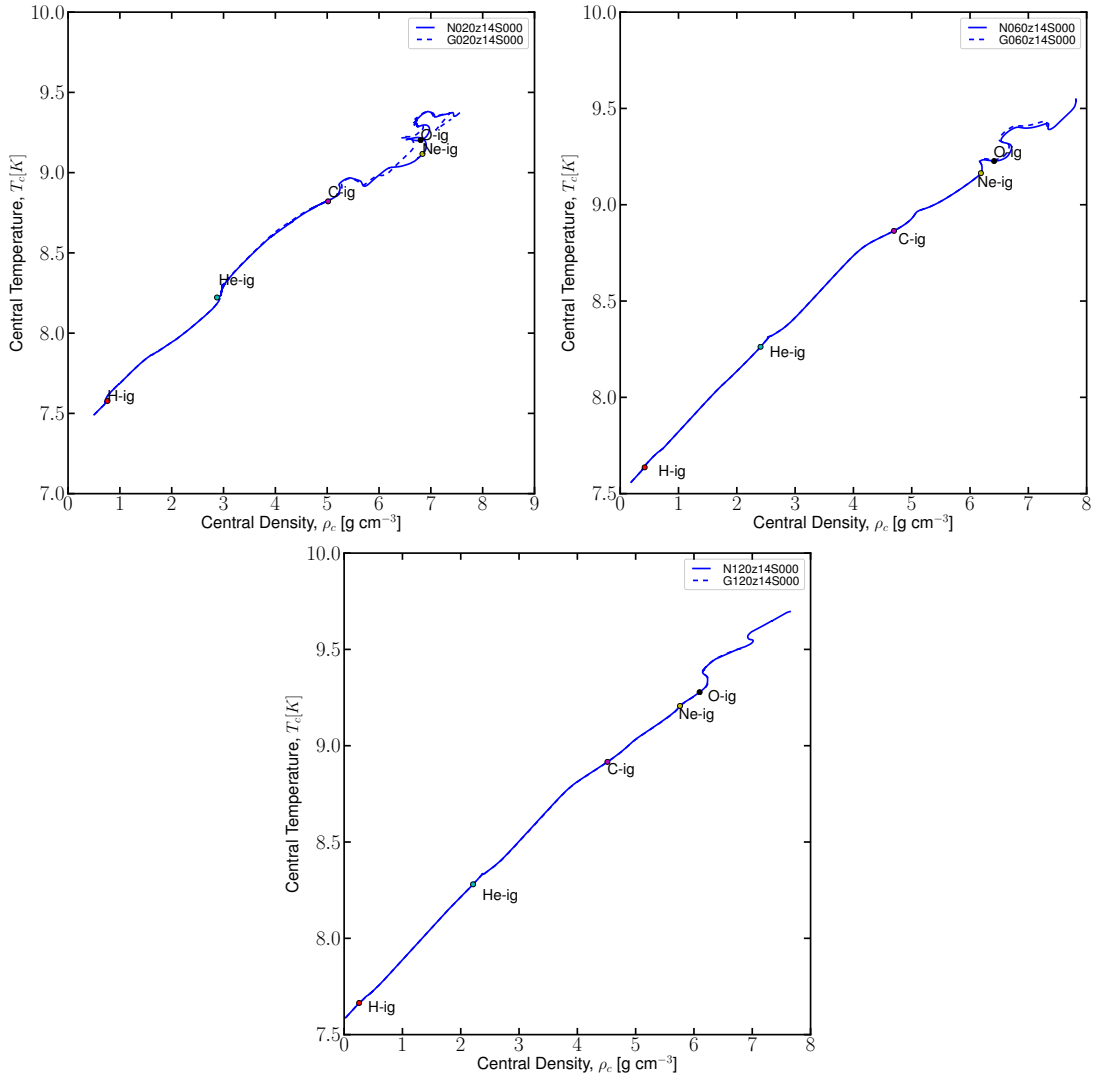


Figure 5.5: T_c - ρ_c diagrams of 20, 60 and 120 M_\odot models. The solid lines represent models with updated neutrino loss while the dotted lines represent models using the old neutrino loss prescription.

burning stage, the neutrino energy loss dominates the energy process at the core of the stars. This scenario is shown in Fig. 5.6, where at the center of the $20 M_{\odot}$ model, the neutrino loss is higher than the nuclear energy generation from the model.

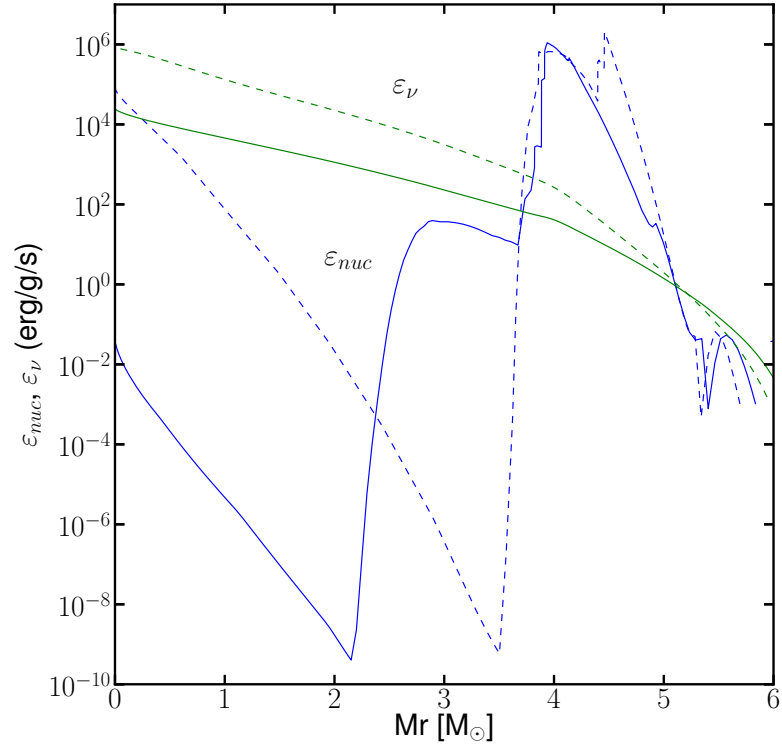


Figure 5.6: Comparison of neutrino energy loss and nuclear energy generation for the $20 M_{\odot}$ models at the start of C-burning. Solid lines represent data from models using Itoh et al. (1996) while dotted lines are from models using Itoh et al. (1989)

The total energy loss for 20 , 60 and $120 M_{\odot}$ models at the start of C-, Ne- and O-burnings are shown in Fig. 5.7. In these figures, the total energy loss by the neutrino processes using Itoh et al. (1996) give agreeable tracks. We notice that for $20 M_{\odot}$ model, the tracks for Itoh et al. (1996) is lower but for the extreme mass, $120 M_{\odot}$ model, the neutrino loss using Itoh et al. (1996) is slightly higher. This might be due to the different effects of neutrino energy loss at different temperature-density regions.

In Itoh et al. (1996) the neutrino energy loss formulations for pair neutrino and photon-neutrino are the same as in Itoh et al. (1989). In Fig. 5.8, we plot two graphs; as

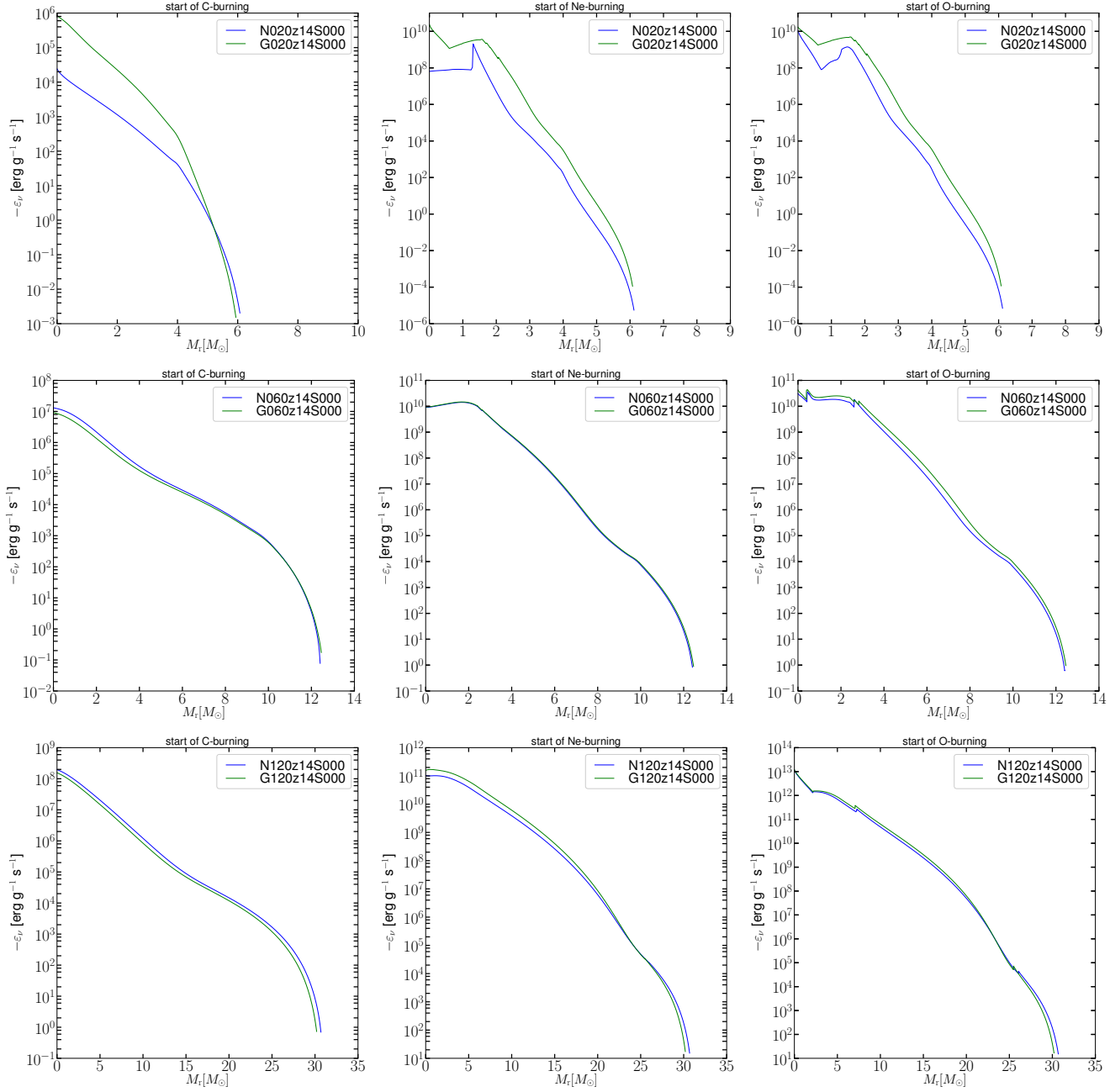


Figure 5.7: Neutrino energy loss for $20 M_{\odot}$ models at start of the C-, Ne and O-burning. Solid lines represent data from models using Itoh et al. (1996) while dotted lines are from models using Itoh et al. (1989)

a function of temperature and density in order to study the neutrino losses from the neutrino processes during the C-burning stages. The photo and pair neutrino energy loss processes do not have significant changes since the formulations used in Itoh et al. (1996) are identical as in Itoh et al. (1989). For plasma neutrino process, the model using Itoh et al. (1996) gives slightly higher value than model using Itoh et al. (1989). This factor has been mentioned in Itoh et al. (1996) where their fitting gives accuracy 5% better when the plasma neutrino process is dominant. But for the bremsstrahlung neutrino energy loss process, there is a huge difference in energy loss which is up to 10 orders of magnitude lower for Itoh et al. (1996).

The difference in bremsstrahlung energy loss is due to the different ionic correlation effects and the screening effects attributable to electrons. The bremsstrahlung neutrino loss formulation for weak and strong degenerate electron in Itoh et al. (1996) is restricted to certain Fermi temperature range, while in Itoh et al. (1989), the authors used Dicus et al. (1976) which does not have this rigid constraint.

However, the neutrino energy loss formulations for plasma and bremsstrahlung processes in Itoh et al. (1996) are different in Itoh et al. (1989). Here we present the comparison for these two processes. Since the neutrino energy loss is dominant in C-burning, we study the neutrino energy loss for plasma and bremsstrahlung processes in the structure of the models from the onset of C-burning, Ne-burning and O-burning. At these stages, the temperature and density of the models are high enough to trigger these processes.

In Fig. 5.9 we present the comparison of plasma and bremsstrahlung neutrino energy loss using Itoh et al. (1996) and Itoh et al. (1989) at the start of C-burning, Ne-burning and O-burning respectively of the $20 M_{\odot}$ model. The solid line represents models using Itoh et al. (1996) while dotted line represents models using Itoh et al. (1989). Both neutrino energy losses from plasma and bremsstrahlung processes using Itoh et al. (1996) are lower compared to Itoh et al. (1989). The value of bremsstrahlung neutrino energy loss using Itoh et al. (1996) is lower in all cases while for plasma neutrino energy loss,

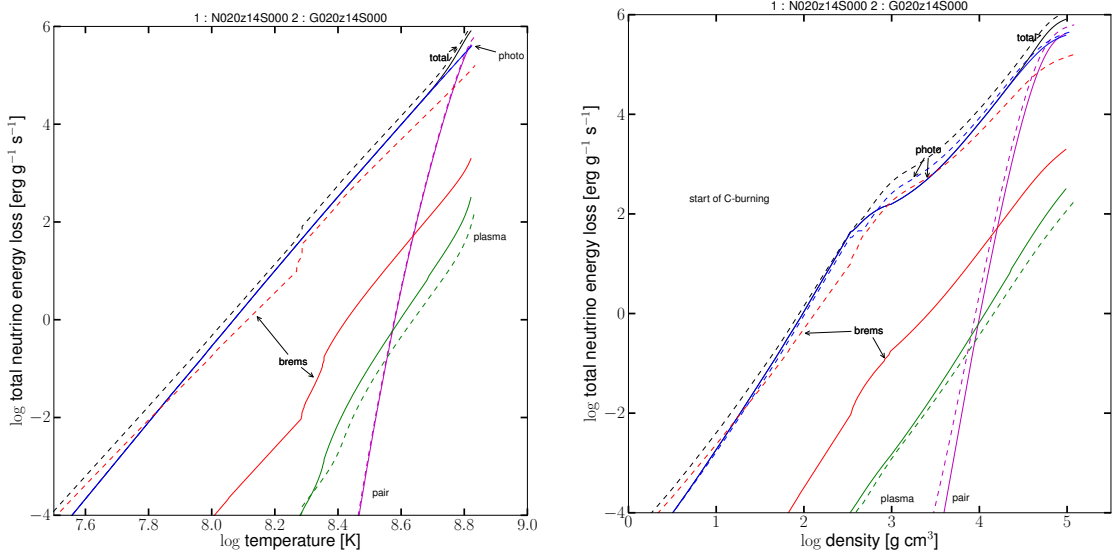


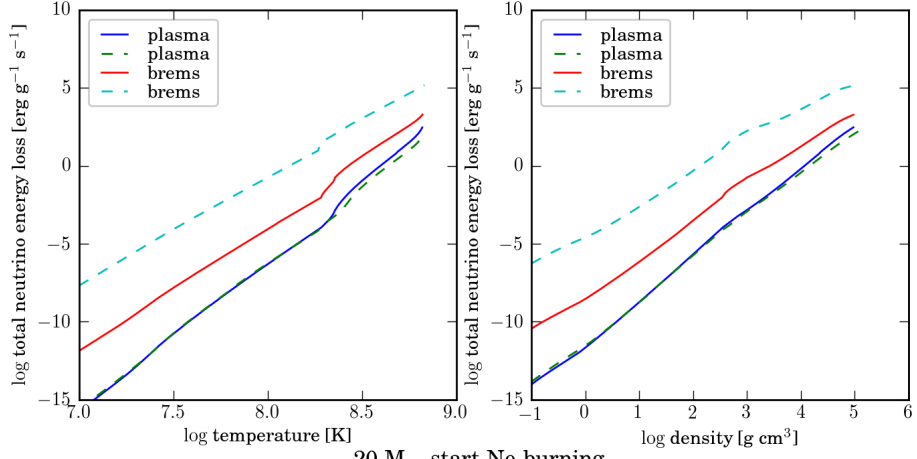
Figure 5.8: Neutrino energy loss for $20 M_{\odot}$ models at the start of C-burning in terms of temperature (left) and density (right). Solid lines represent data from models using Itoh et al. (1996) while dotted lines are for models using Itoh et al. (1989)

the value slightly increase towards the center of the model.

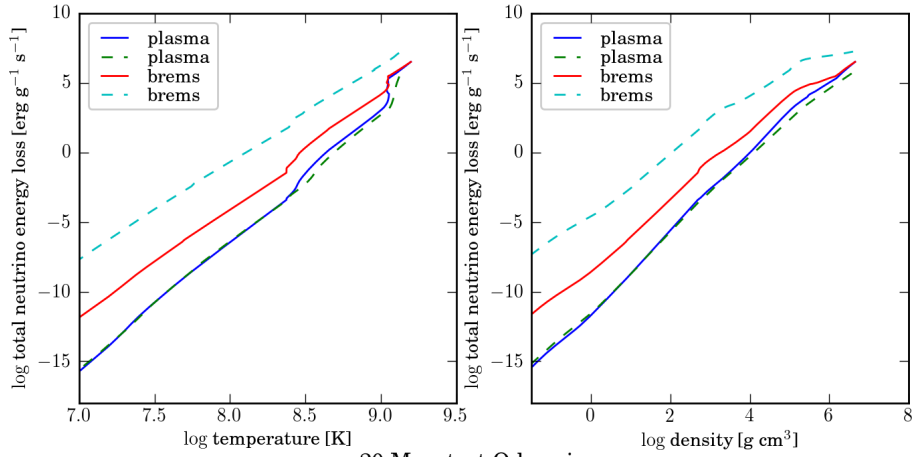
The comparison for $60 M_{\odot}$ model is presented in Fig. 5.10. This model has higher temperature and density compared to the $20 M_{\odot}$ model. For the bremsstrahlung neutrino energy loss, the difference between these two prescriptions is similar to $20 M_{\odot}$ models. We find the plasma neutrino process in models using Itoh et al. (1996) shows significant increase compared to models using Itoh et al. (1989). This difference has been explained in the previous paragraph. When the temperature and density are high enough at the start of O-burning, the plasma process compete with the bremsstrahlung process. This happens when $T \sim \log_{10}(9.3)$ K and $\rho \geq \log_{10}(6)$ gcm^{-3} . When T and ρ are greater than these values, the plasma process dominates over the bremsstrahlung process.

The comparison for $120 M_{\odot}$ model is presented in Fig. 5.11. This model has higher temperature and density compared to $20 M_{\odot}$. This model represents the extreme mass in this study on the neutrino energy loss. The changes of neutrino energy loss in this model are similar to the $60 M_{\odot}$ model except at start of O-burning where the bremsstrahlung is

20 M_{\odot} , start C-burning



20 M_{\odot} , start Ne-burning



20 M_{\odot} , start O-burning

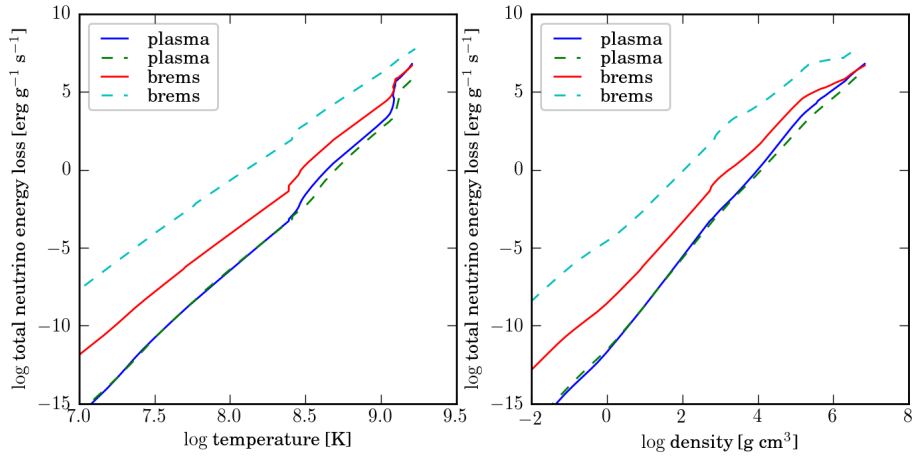
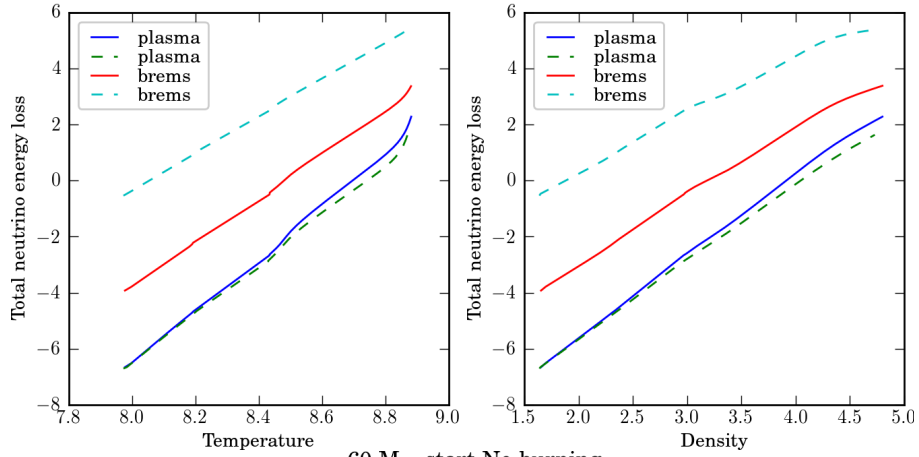
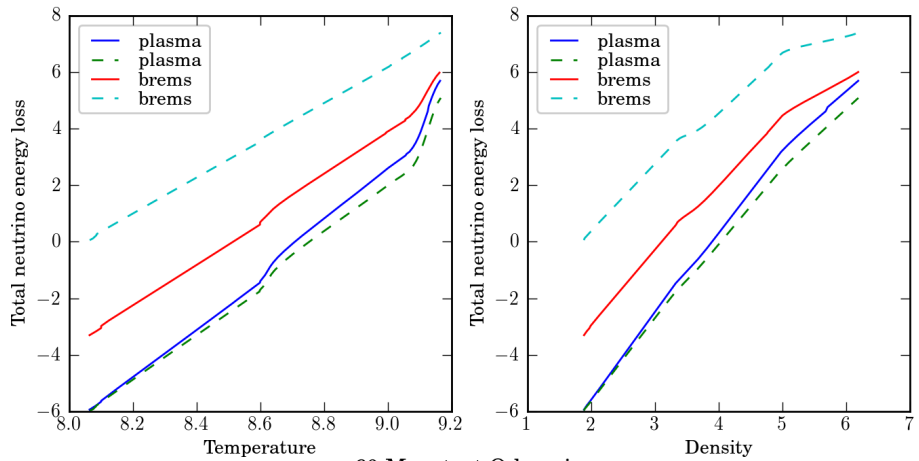


Figure 5.9: Neutrino energy loss for 20 M_{\odot} models at start of C-, Ne and O-burning. Solid lines represent models using Itoh et al. (1996) while dotted lines represent model using Itoh et al. (1989).

60 M_{\odot} , start C-burning



60 M_{\odot} , start Ne-burning



60 M_{\odot} , start O-burning

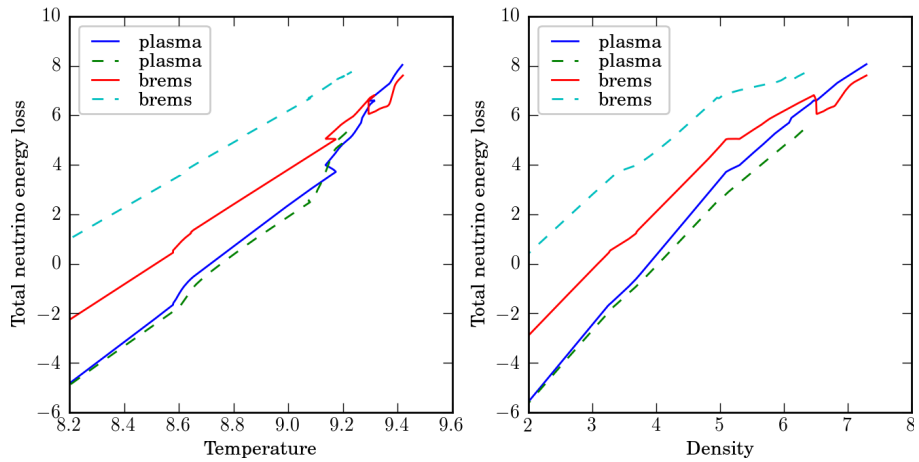
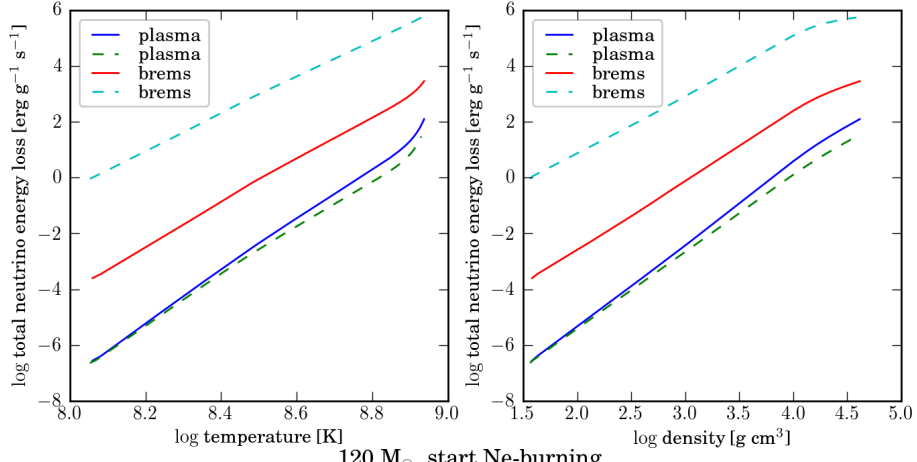
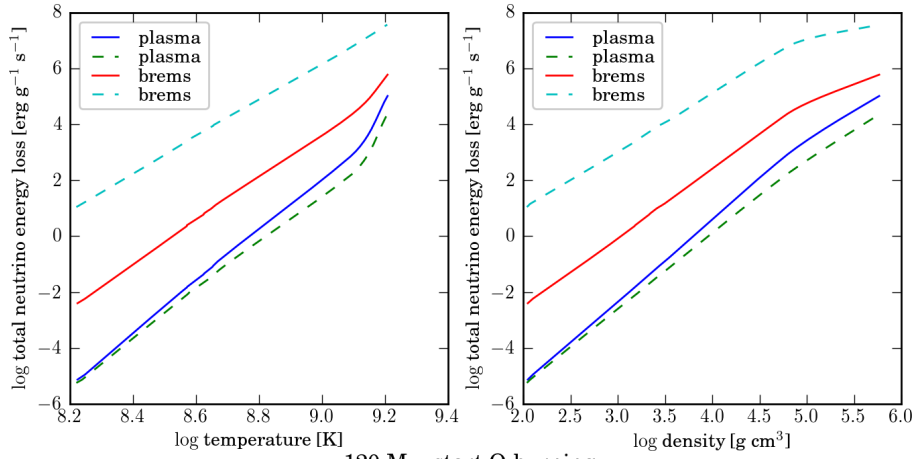


Figure 5.10: Neutrino energy loss for 60 M_{\odot} models at start of C-burning, Ne-burning and O-burning. Solid lines represent models using Itoh et al. (1996) while dotted lines represent model using Itoh et al. (1989).

120 M_⊙, start C-burning



120 M_⊙, start Ne-burning



120 M_⊙, start O-burning

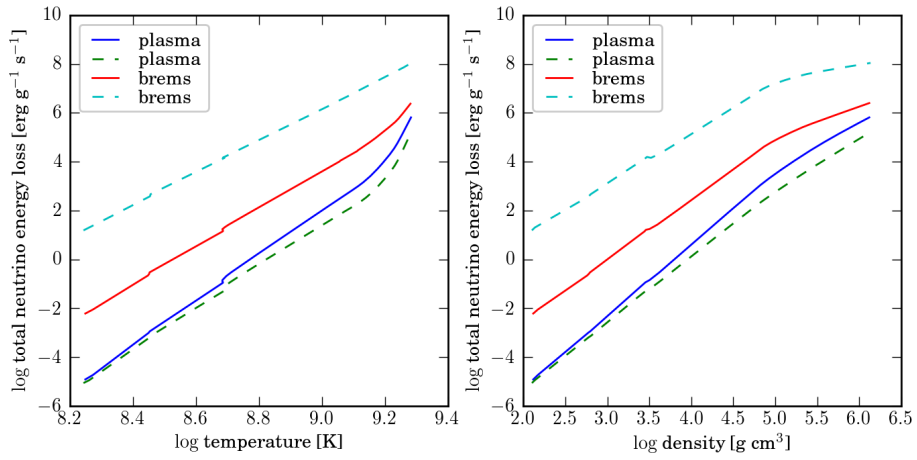


Figure 5.11: Neutrino energy loss for 120 M_⊙ models at start of C-burning, Ne-burning and O-burning. Solid lines represent models using Itoh et al. (1996) while dotted lines represent model using Itoh et al. (1989).

more dominant than the plasma process. Although this model has higher initial mass than $60 M_{\odot}$ model, it loses more mass than $60 M_{\odot}$ model due to the strong mass loss during the evolution. This affects the density of the model where this model is less dense than the $60 M_{\odot}$ model. At the start of O-burning, the density at the center is around $\rho \sim \log_{10}(9.2)$ gcm^{-3} while in $60 M_{\odot}$ model, their density is around $\rho \sim \log_{10}(9.3)$ gcm^{-3} . This gives the reason why the bremsstrahlung is still large compared to the plasma process.

5.4.4 Kippenhahn diagrams

The Kippenhahn diagrams of all models are presented in Fig 5.12 for $20 M_{\odot}$ model, Fig 5.13 for $60 M_{\odot}$ model and Fig. 5.14 for $120 M_{\odot}$ model. The diagrams are plotted as a function of time before core-collapse in order to investigate any changes in the internal burning of the models. In all models, we find there is no significant changes if we use neutrino energy loss from Itoh et al. (1996).

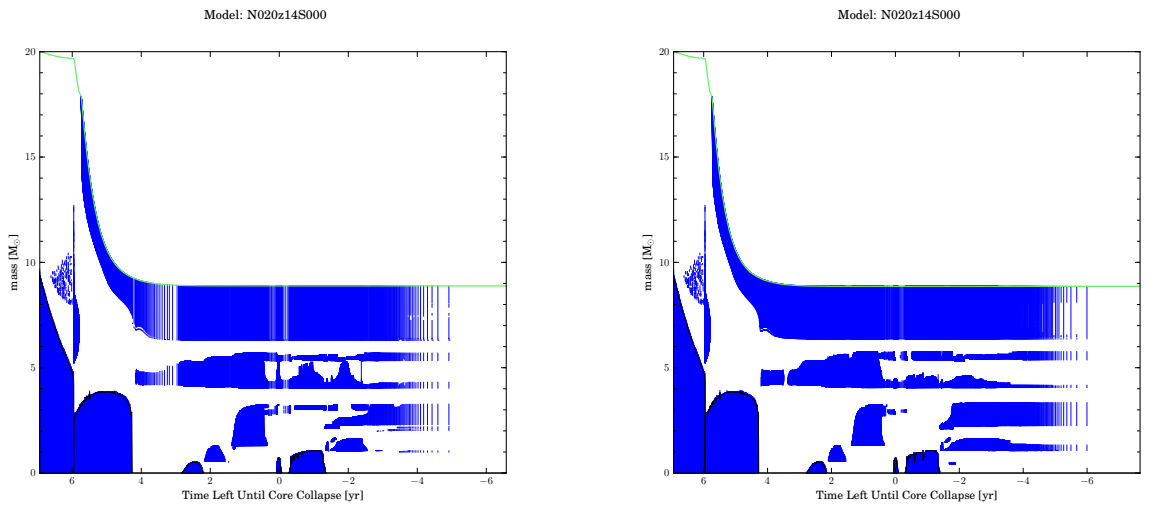


Figure 5.12: Kippenhahn diagrams of $20 M_{\odot}$ models using Itoh et al. (1996) (N020z14S000) and models using Itoh et al. (1989) (G020z14S000).

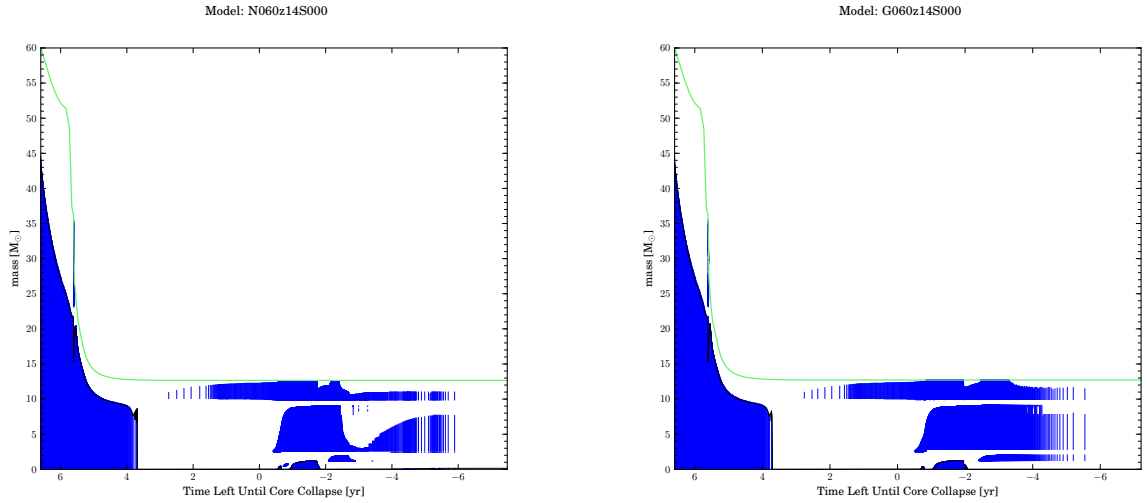


Figure 5.13: Kippenhahn diagrams of $60 M_{\odot}$ models using Itoh et al. (1996) (N060z14S000) and models using Itoh et al. (1989) (G060z14S000).

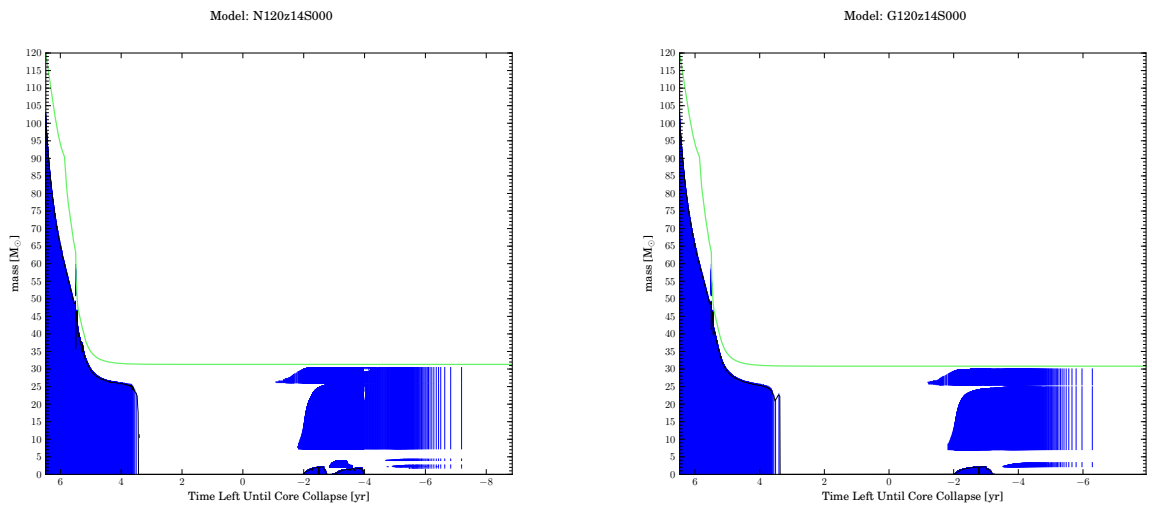


Figure 5.14: Kippenhahn diagrams of $120 M_{\odot}$ models using Itoh et al. (1996) (N120z14S000) and models using Itoh et al. (1989) (G120z14S000).

5.5 Summary

We have implemented an update for the neutrino subroutine in the Geneva stellar evolution code using the neutrino energy loss from Itoh et al. (1996). We find that there is a slight decrease in the total neutrino energy loss using Itoh et al. (1996) compared to models using Itoh et al. (1989) for 20 M_{\odot} model but in 120 M_{\odot} model, the changes are reversed. These slight changes do not affect the overall evolution of the models. From our study, we find this update gives agreeable tracks in the HR diagram. No significant changes are observed in the central and surface of the models. This is due to the dominant neutrino loss throughout the evolution coming from the photoneutrino process.

The most important change in this update is the different formulation used for the plasma and bremsstrahlung neutrino processes in Itoh et al. (1996). At temperature and density relevant to these processes, we study these differences. We summarise these differences in the following points:

- Low bremsstrahlung neutrino energy loss during the evolution for Itoh et al. (1996) compared to Itoh et al. (1989). Itoh et al. (1996) gives more accurate calculation in the ionic correlation effects and screening effects. This reduces the error in calculating the bremsstrahlung neutrino energy loss.
- Slightly higher plasma neutrino energy loss during the evolution for Itoh et al. (1996) compared to Itoh et al. (1989). The fitting provided in Itoh et al. (1996) gives better accuracy by 5 % at high temperature domain compared to the lower temperature range quoted in Itoh et al. (1989).
- Plasma neutrino energy loss contributes more energy than bremsstrahlung at the end of O-burning for 60 M_{\odot} model using Itoh et al. (1996). This contribution cannot be seen if we use Itoh et al. (1989).

Chapter 6

Updated Nuclear Reaction Rate Using WKB Method and Application in the Evolution of Massive Stars

6.1 Motivation

The most important process in stellar evolution and nucleosynthesis is the thermonuclear fusion. Light nuclei fuse into heavier nuclei and produce photons which serve as the interior source of energy radiating from the surface. This idea was first shown by Atkinson & Houtermans (1929) after Gamow discovered the tunneling effect in quantum mechanics. Later, two mechanisms were identified as the main reaction groups for fusion in the stars during hydrogen burning, i.e pp chain (Bethe & Critchfield, 1938) and CNO cycle by Bethe (1939). For helium burning, the nuclear reaction in this stage was described by Salpeter (1952). Finally, the milestone of element synthesis in the star was summarised in the classic paper by Burbidge et al. (1957).

Massive stars spend almost 90% of their life burning hydrogen and most of the rest burning helium. For the first generation stars (Population III), the energy production

is dominated by both pp chain and CNO cycle (see e.g Ekström et al., 2008) since they consist mainly of hydrogen and helium. Most of the present massive stars are second and third generation of stars (Population I) where the energy production is dominated by the CNO cycle during the H-burning. This is due to the fact that these stars are formed from material which, in addition to hydrogen and helium, contains heavier elements synthesised in previous generation of stars.

The aim of this chapter is to study the effects of the updated nuclear reaction rates using WKB (Wentzel-Kramers-Brillouin) method on the evolution of massive stars. First, we demonstrate how we update the nuclear reaction rates from first principle through the improvement in the tunneling effects. This is done by keeping the full expansion in energy of the tunneling probability suitable for the non-resonant reactions. Second, we implement this tunneling probability in the cross section and astrophysical S-factor. We also calculate the effective energy, E_0 related to the tunneling probability and finally obtain the updated nuclear reaction rate, $\langle\sigma v\rangle$.

Five reactions are chosen to study the impact of the improvement in $\langle\sigma v\rangle$ i.e ${}^3\text{He}({}^3\text{He},2\text{p}){}^4\text{He}$, ${}^3\text{He}(\alpha,\gamma){}^7\text{Be}$, ${}^{12}\text{C}(p,\gamma){}^{13}\text{N}$, ${}^{15}\text{N}(p,\gamma){}^{16}\text{O}$ and ${}^{16}\text{O}(p,\gamma){}^{17}\text{F}$. Although ${}^3\text{He}({}^3\text{He},2\text{p}){}^4\text{He}$ and ${}^3\text{He}(\alpha,\gamma){}^7\text{Be}$ are not relevant in the H-burning of Population I massive stars, these reactions are included due to the significant contribution in the production of energy in the Population III stars.

These updated nuclear reaction rates are implemented in the nuclear network in the stellar evolution code. In the Geneva code, the nuclear reaction rates for H-burning are obtained from the NACRE compilation (Angulo et al., 1999). We evolve four solar metallicity models, i.e 20 and 120 M_{\odot} with both rotation and non-rotation applied to the models. From these stellar evolution models, we study the impact of these updated reaction rates to the evolution of massive stars by comparing these stellar models to models using the standard nuclear reactions.

6.2 WKB method and astrophysical S-factor

The interaction between two charged particles can only occur when the reacting nuclei tunnel through the repulsive Coulomb barrier. When this happens, the potential together with the attractive nuclear force is shown in Fig. 6.1

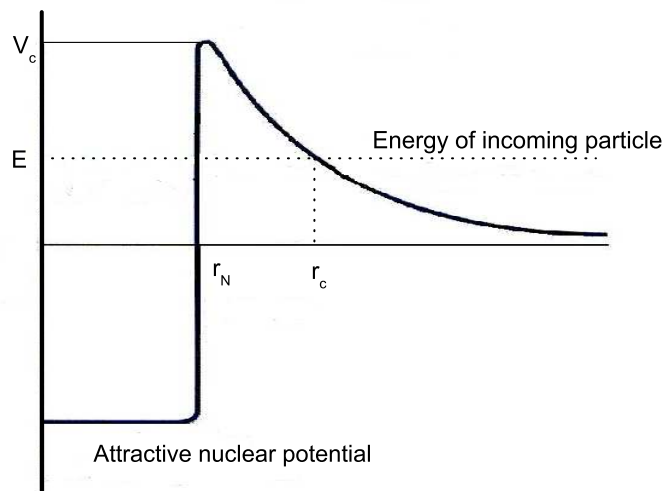


Figure 6.1: Coulomb barrier where r_N is the nuclear radius when the net charge is at the center of the nucleus and r_c is the position of the incoming particle.

The application of WKB method as a tool in calculating tunneling probability of astrophysical interest has been done by several authors (Humblet et al., 1987; Beaumevielle et al., 1999) but was approximated at low energy. In general the WKB tunneling probability, $P(E)$ as a function of energy, E for zero angular momentum is given by

$$P(E) = \exp\left(-\frac{2}{\hbar} \int dr \sqrt{2\mu[V_c - E]}\right) \quad (6.1)$$

where μ is the reduced mass and V_c is the Coulomb potential. By solving the integral,

the exact tunneling probability that is valid over all energies is presented as

$$P_e(E) = - \left(\frac{8Z_1Z_2e^2}{\hbar} \right)^{\frac{1}{2}} \left[\cos^{-1} \left(\frac{r_N}{r_c} \right)^{\frac{1}{2}} - \left(\frac{r_N}{r_c} - \frac{r_N^2}{r_c^2} \right)^{\frac{1}{2}} \right] \quad (6.2)$$

where Z_1 and Z_2 are the atomic numbers of the target nucleus and incoming nucleus respectively, r_N is the nuclear radius and r_c is the width of the Coulomb separation. At low energy, Eq. (6.2) for nuclei with $E \ll V_c$ in which case $r_N \ll r_c$, will lead to the following well known equation for the standard tunnelling probability

$$P_s(E) = \exp(-2\pi\eta) \quad (6.3)$$

where η is the Sommerfield parameter with a numerical value

$$2\pi\eta = 31.29Z_iZ_j \left(\frac{\mu}{E} \right)^{\frac{1}{2}}. \quad (6.4)$$

In this case, E is the centre of mass energy in keV and μ is the reduced mass in amu. As mentioned earlier, our aim is to use the full solution of Eq. (6.2) instead of Eq. (6.3) in calculating $\langle \sigma v \rangle$.

Fig. 6.2 is an example to illustrate the comparison between the probability using the exact probability, P_e with the standard probability, P_s for $^{12}\text{C}(p,\gamma)^{13}\text{N}$. In this figure, the exact probability is higher compared to the standard probability.

6.2.1 S-factor

In nuclear astrophysics, the S-factor is often used when calculating reaction rates instead of cross section, σ since the experimental cross section data vary by orders of magnitude. The S-factor has the advantage that it varies very slowly over a given energy range. We

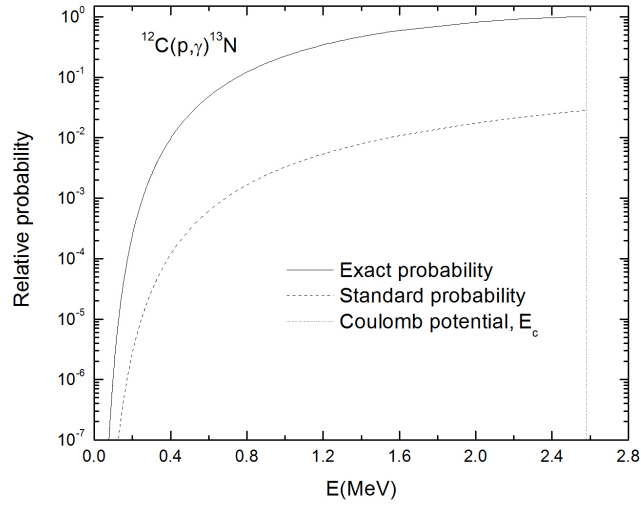


Figure 6.2: Comparison of exact probability and standard probability for $^{12}\text{C}(p,\gamma)^{13}\text{N}$.

define the exact astrophysical S-factor as

$$S_e(E) = \sigma(E)E/P_e(E) \quad (6.5)$$

while the standard definition of S-factor in the literature will be

$$S_s(E) = \sigma(E)E/P_s(E) \quad (6.6)$$

Eq. (6.6) implies a wide Coulomb barrier or low energy but in experiments, very high energy projectiles were used to bombard the target nucleus in order to produce the nuclear reaction. Thus we advocate the use of Eq. (6.5) to calculate the S-factor. In Figs. 6.3, 6.4, 6.5, 6.6 and 6.7, we present the comparison of S-factor by using Eq. (6.5) and Eq. (6.6). We have used the experimental data for cross section, σ obtained from NACRE compilation (Angulo et al., 1999 and their references therein) in order to calculate the S-factor.

${}^3\text{He}({}^3\text{He},2\text{p}){}^4\text{He}$

Our best polynomial fit approximation to the exact S-factor of ${}^3\text{He}({}^3\text{He},2\text{p}){}^4\text{He}$ reaction is

$$S_e(E) = 0.03526 - 0.02672E + 0.03592E^2 \quad (6.7)$$

where E is in MeV and $S_e(E)$ in MeV b. The exact S-factor at zero energy, $S_e(0) = 0.03526$ MeV b while the NACRE compilation gives $S_s(0) = 5.18$ MeV b and this gives a difference of about two orders of magnitude.

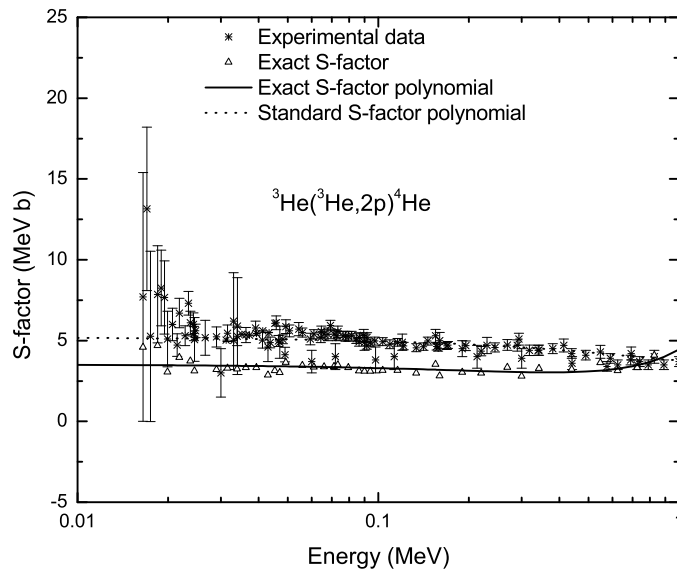


Figure 6.3: S-factor of ${}^3\text{He}({}^3\text{He},2\text{p}){}^4\text{He}$ reaction.

${}^3\text{He}(\alpha,\gamma){}^7\text{Be}$

For ${}^3\text{He}({}^4\text{He},\gamma){}^7\text{Be}$ reaction, our best polynomial fit is

$$S_e(E) = 0.00263 - 4.4677 \times 10^{-6}E + 2.176 \times 10^{-8}E^2 \quad (6.8)$$

where E is in MeV and $S_e(E)$ in keV b. Here the exact S-factor is normalised by a factor of 100. We obtain $S_e(0) = 0.00263$ keV b and the NACRE value is $S_s(0) = 0.54$ keV b. As in ${}^3\text{He}({}^3\text{He}, 2p){}^4\text{He}$ reaction, we again find the value of the exact S-factor is two orders of magnitude smaller than NACRE compilation.

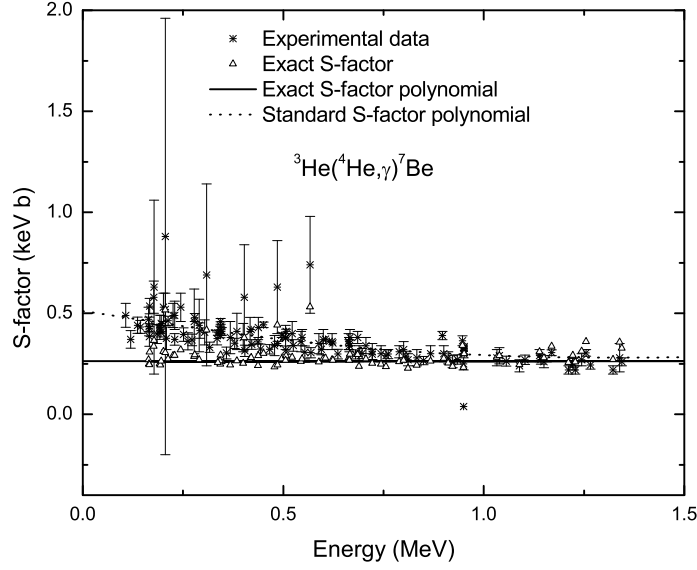
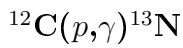


Figure 6.4: S-factor of ${}^3\text{He}(\alpha, \gamma){}^7\text{Be}$ reaction.



${}^{12}\text{C}(p, \gamma){}^{13}\text{N}$ reaction is the first reaction in the CNO cycle which plays an important role in the energy generation of massive stars. This is a resonant reaction at around 0.4 MeV and for this work, we only consider the non-resonant part in order to obtain the S-factor. In NACRE (Angulo et al., 1999), the value for $S(0)$ was not provided but in Rolfs & Azuma (1974), they gave a value of $S(25 \text{ keV}) = 1.45 \pm 0.20$ keV b. The extrapolation for ${}^{12}\text{C}(p, \gamma){}^{13}\text{N}$ in the energy range $E \leq 0.411$ MeV for all data gives the fitting of exact S-factor as

$$S_e(E) = -0.00435 + 0.1378E - 1.6045E^2 + 8.666E^3 - 21.87E^4 + 20.86E^5 \quad (6.9)$$

where E is in MeV and S-factor in MeV b. The exact S-factor is normalized by a factor of 80 and plotted in Fig. 6.5. We are now able to state the zero energy S-factor which is $S_e(0) = -0.00435$ MeV b.

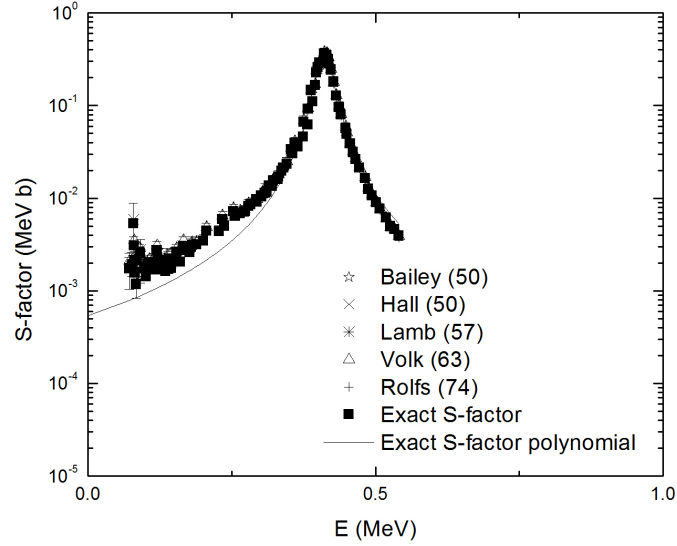


Figure 6.5: S-factor for $^{12}\text{C}(p,\gamma)^{13}\text{N}$ reaction.

$^{15}\text{N}(p,\gamma)^{16}\text{O}$

$^{15}\text{N}(p,\gamma)^{16}\text{O}$ reaction is a reaction that provides the path from the CN cycle to the CNO bi-cycle and CNO tri-cycle. This reaction has a resonance at $E = 0.5$ MeV and extrapolation of the data of this reaction in NACRE gives $S_s(0) = 64 \pm 6$ keV b. The exact S-factor extrapolated by fitting the data for $E \leq 0.319$ MeV only from Rolfs & Rodney (1974) gives

$$S_e(E) = 0.28397 / (1 - 5.95273E + 9.79684E^2) \quad (6.10)$$

where E in MeV and S-factor in MeV b. The exact S-factor is represented in Fig. 6.6 with normalization by a factor of 120. Here $S_e(0) = 0.28397$ MeV b.

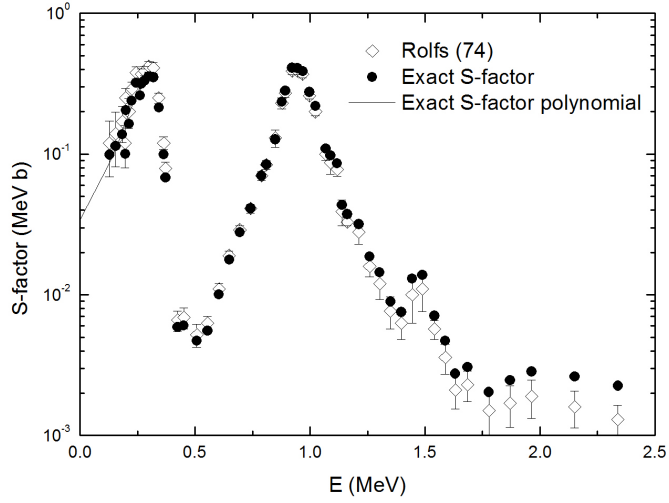
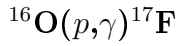


Figure 6.6: S-factor for $^{15}\text{N}(p,\gamma)^{16}\text{O}$ reaction.



The recommended S-factor given in NACRE is 9.3 ± 2.8 keV b. This S-factor takes 30 % of overall uncertainty for low energy approximation that includes 10% systematic error and 20% error due to the model assumptions. The best fit gives a polynomial of order four which is given by

$$S_e(E) = 0.03585 - 0.03616E + 0.03249E^2 - 0.01216E^3 + 0.00191E^4. \quad (6.11)$$

The energy, E is in MeV while the S-factor in units of keV b. The fitting covers energy range $E \leq 3.233$ MeV. The recommended standard S-factor is $S_s(0) = 9.3 \pm 2.8$ keV b at zero energy while $S_e(0) = 0.03585$ keV b. Fig. 6.7 depicts the exact S-factor that has been normalized by a factor of 150.

We shall see what is the effect of the exact tunneling probability and the new definition of S-factor towards the reaction rate per pair. By using Eq. (6.2) and Eq. (6.5) the

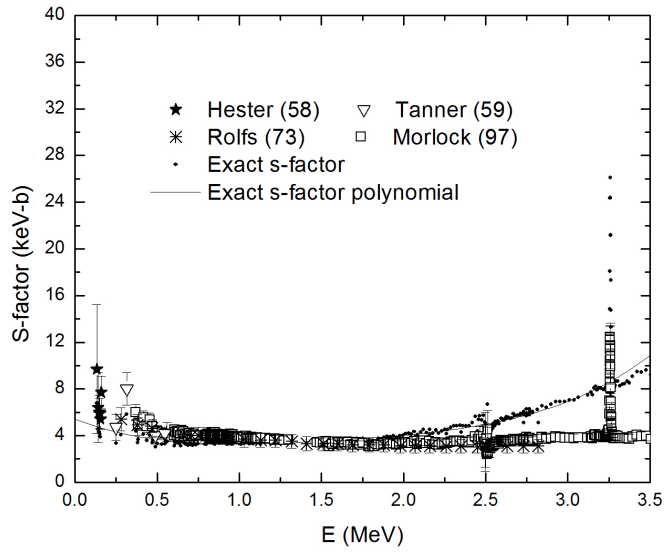


Figure 6.7: S-factor for $^{16}\text{O}(p,\gamma)^{17}\text{F}$ reaction.

reaction rate per pair becomes

$$\langle\sigma v\rangle = \left(\frac{8}{\pi\mu}\right)^{1/2} \left(\frac{1}{kT}\right)^{1/2} \int_0^\infty S_e(E) \exp\left[-\frac{E}{kT} - P_e(E)\right] dE \quad (6.12)$$

where k is the Boltzmann constant and T the temperature.

6.2.2 Derivation of effective energy

In order to integrate Eq. (6.12), we need to impose a finite limit on the energy range. The integrand itself is a sharply peaked function, which is the product between two exponential terms. These nuclei react at the maximum rate when the integrand reaches its peak. The value of the effective energy, E_0 can be obtained by finding the maximum of the integrand. Our E_0 is given as (Yusof & Kassim, 2009)

$$\beta \left[-\frac{1}{(1-x)^{\frac{1}{2}}} \left(1 - \frac{1}{2}x^{\frac{1}{2}}\right) - \frac{1}{2}x^{-\frac{1}{2}}(1-x)^{\frac{1}{2}} \right] - \frac{1}{2} \left(\frac{\gamma}{x}\right)^{\frac{1}{2}} \left[\cos^{-1} x^{\frac{1}{2}} - x^{\frac{1}{2}}(1-x)^{\frac{1}{2}} \right] = 0 \quad (6.13)$$

where $x = E_0/V_c$, $\gamma = 8\mu(Z_1Z_2e^2)^2/\hbar^2V_c$ and $\beta = V_c/kT + (\gamma/x)^{\frac{1}{2}}$.

The effective energy formulation given by Eq. (6.13) is more complex compared to the solution using the standard E_0 ,

$$E_0 = 1.22(Z_1^i Z_2^j \mu T_6^2)^{\frac{1}{3}} \text{keV} \quad (6.14)$$

whose validity is at low energy. Although our new effective energy equation Eq. (6.13) looks more complex than the standard E_0 , its value can be easily computed using a numerical method. In fact, E_0 can be solved by any iterative method. We present the comparison of E_0 using the exact probability and standard probability for $^{12}\text{C}(p,\gamma)^{13}\text{N}$ reaction in Fig. 6.8. In this figure, the E_{0e} is lower than the E_{0s} at $\log T \geq 9$. This value is expected since using the exact probability, there is a higher chance for the nuclei to overcome the Coulomb barrier and thus lowers the effective energy of the interacting nuclei.

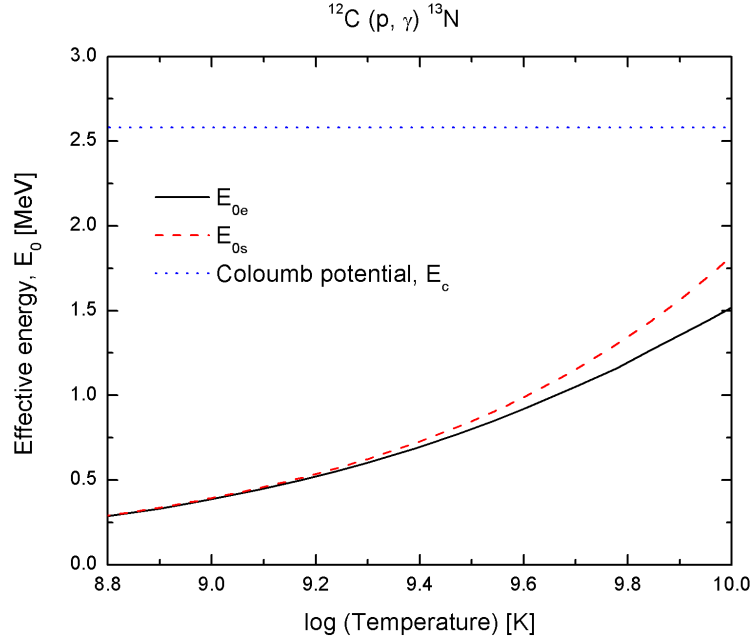


Figure 6.8: The effective energy derived from the exact probability in comparison with the effective energy using the standard probability for $^{12}\text{C}(p,\gamma)^{13}\text{N}$ reaction.

6.2.3 Updated reaction rates

Figs. 6.9, 6.10, 6.11, 6.12 and 6.13 show the ratio of the newly updated reaction rates, $\langle\sigma v\rangle$ of $^3\text{He}(^3\text{He},2p)^4\text{He}$, $^3\text{He}(\alpha,\gamma)^7\text{Be}$, $^{12}\text{C}(p,\gamma)^{13}\text{N}$, $^{15}\text{N}(p,\gamma)^{16}\text{O}$ and $^{16}\text{O}(p,\gamma)^{17}\text{F}$ compared to NACRE. At low temperature, the reaction rates are identical since $P_e \approx P_s$. The feature common amongst the graphs shown is that the ratio starts to decrease at $T \sim 10^9$ K. This shows that at this temperature the improved reaction rate becomes lower compared to NACRE's rate and it is consistent with Fig. 6.2.

We present a table for all the updated reaction rates at temperatures relevant to H-burning in Table 6.1. The updated reaction rates give similar values for $^3\text{He}(^3\text{He},2p)^4\text{He}$, $^3\text{He}(\alpha,\gamma)^7\text{Be}$ and $^{16}\text{O}(p,\gamma)^{17}\text{F}$ reactions. For $^{12}\text{C}(p,\gamma)^{13}\text{N}$ and $^{15}\text{N}(p,\gamma)^{16}\text{O}$ reactions, the updated reaction rates give slightly lower values compared with NACRE.

Table 6.1: Table of $\langle\sigma v\rangle$ at temperatures relevant to H-burning, $\log_{10} T = 7$ and $\log_{10} T = 8$. The unit for these values is $\text{cm}^3 \text{mol}^{-1} \text{s}^{-1}$.

Reaction	$\log_{10} T = 7$	$\log_{10} T = 8$	$\log_{10} T = 7$	$\log_{10} T = 8$
	This work		NACRE	
${}^3\text{He}({}^3\text{He}, 2\text{p}){}^4\text{He}$	2.64E-13	9.83E-01	2.16E-13	8.33E-01
${}^3\text{He}(\alpha, \gamma){}^7\text{Be}$	1.55E-18	2.33E-05	1.64E-18	2.42E-05
${}^{12}\text{C}(p, \gamma){}^{13}\text{N}$	5.28E-20	1.06E-05	1.18E-19	2.18E-05
${}^{15}\text{N}(p, \gamma){}^{16}\text{O}$	2.93E-21	3.38E-05	4.33E-21	4.23E-05
${}^{16}\text{O}(p, \gamma){}^{17}\text{F}$	6.32E-25	1.33E-07	6.73E-25	1.26E-07

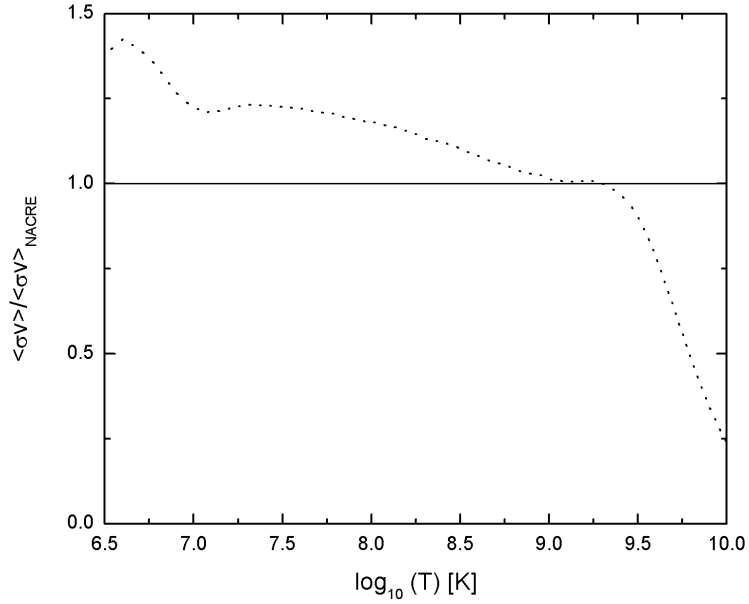


Figure 6.9: The reaction rate ratio of ${}^3\text{He}({}^3\text{He}, 2\text{p}){}^4\text{He}$ compared to NACRE.

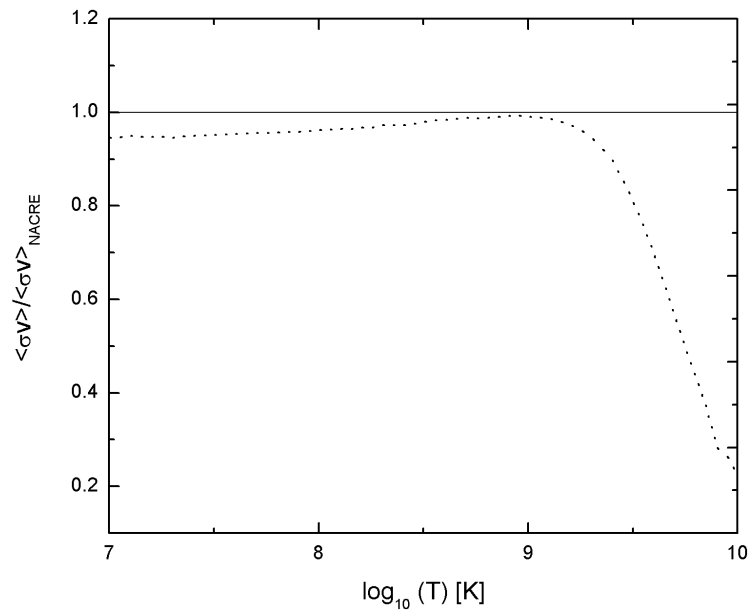


Figure 6.10: The reaction rate ratio of ${}^3\text{He}(\alpha, \gamma){}^7\text{Be}$ compared to NACRE.

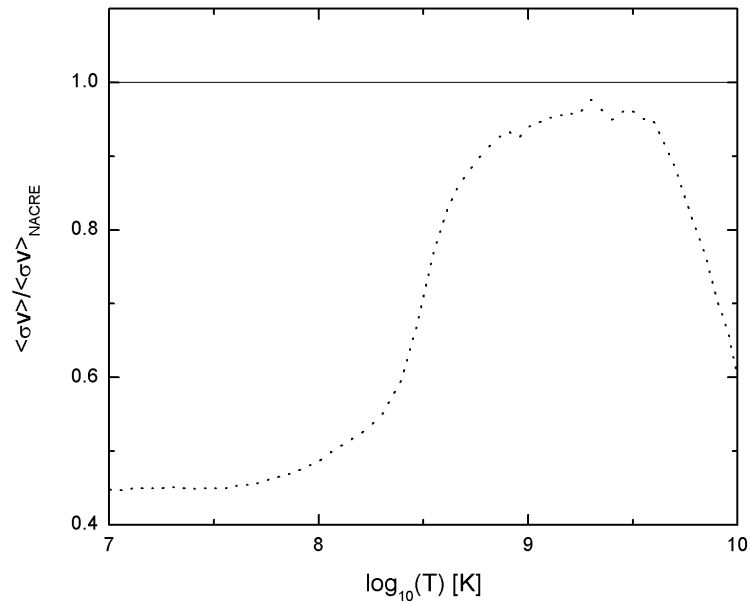


Figure 6.11: The reaction rate ratio of ${}^{12}\text{C}(p, \gamma){}^{13}\text{N}$ compared to NACRE.

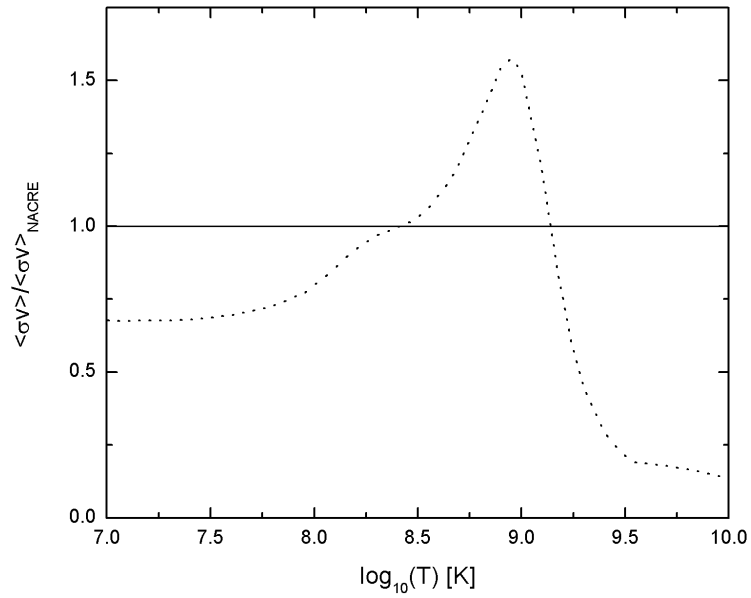


Figure 6.12: The reaction rate ratio of $^{15}\text{N}(p,\gamma)^{16}\text{O}$ compared to NACRE.

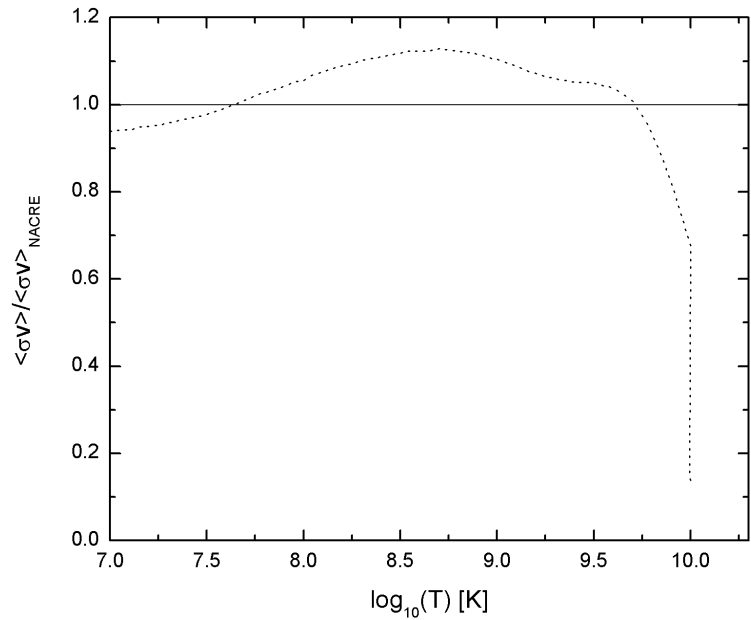


Figure 6.13: The reaction rate of $^{16}\text{O}(p,\gamma)^{17}\text{F}$ compared to NACRE.

6.3 Application to stellar models: $20 M_{\odot}$ and $120 M_{\odot}$ solar metallicity models

In this work, we include the updated reaction rates that are calculated in Section 6.2.3 in the stellar evolution code. In Geneva code, the nuclear network for hydrogen burning is illustrated in Fig. 2.1 of Chapter 2. The code does not follow the ${}^7\text{Be}$ and ${}^7\text{Li}$ evolutions and assumes that their sum is constant. The dominant effect of hydrogen burning is the transformation of protons to ${}^4\text{He}$. The details of nuclear transformation in hydrogen burning network can be found in Maeder (1983).

For this work, two $20 M_{\odot}$ and $120 M_{\odot}$ models at solar metallicity are used as the test models. We choose these two extreme initial mass because we want to study what are the effects of the updated reaction in a common case ($20 M_{\odot}$) and in an extreme case ($120 M_{\odot}$). The test on the solar models using these reaction rates has been published in Yusof & Kassim (2010). Physics of these models are the same as we have used in Chapter 4. For rotation, we choose a rotation rate of $v/v_{crit} = 0.4$. In these models, the mass loss prescriptions are similar as in Chapter 4.

6.4 Hertzsprung-Russell and Kippenhahn diagrams

In this section, we present the Hertzsprung-Russell (HR) and Kippenhahn diagrams of $20 M_{\odot}$ and $120 M_{\odot}$ of both rotating and non-rotating models. In Fig. 6.14, for the non-rotating models there is no difference in the models using the standard nuclear reaction rates. However, for rotating model, we found after the main sequence, the model using the updates rates have higher luminosity. For $120 M_{\odot}$ in Fig. 6.15, both rotating and non-rotating models follow similar pattern as the models using the standard nuclear network.

In order to understand in more detail about the effect of the nuclear reaction rate, we present the evolution of the models in a Kippenhahn diagram. Fig. 6.16 and Fig. 6.17 show the Kippenhahn diagrams of the same models as a function of time before core collapse. In these figures, only $20 M_{\odot}$ rotating models shows slight changes in the convective envelope and shell. The updated nuclear reaction rate model gives thinner convective envelope and experiences stronger mass loss compared to the model using the standard network. We observe less carbon being produce at the start of Ne burning thus enhancing the oxygen burning in this new model.

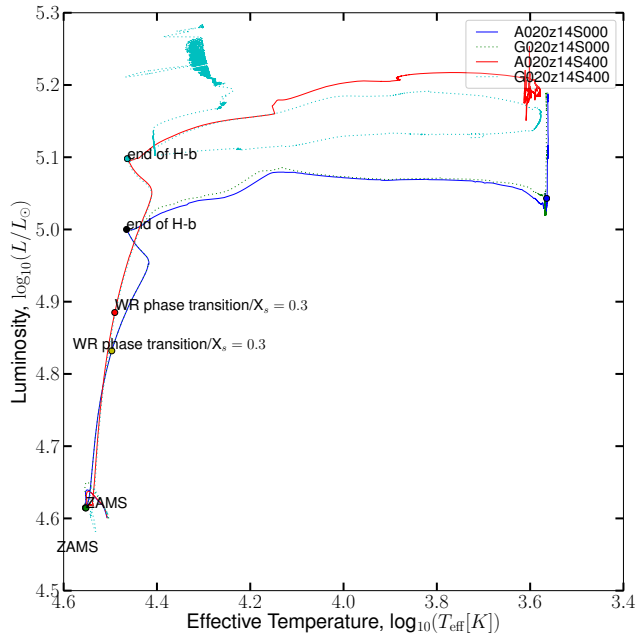


Figure 6.14: HR diagrams of $20 M_{\odot}$ rotating and non-rotating models with comparison to models using standard nuclear reaction rates.

6.4.1 Surface abundances

We present the stellar models surface properties of $20 M_{\odot}$ and $120 M_{\odot}$ solar metallicity rotating and non-rotating models in Table 6.2. In this table, we list the initial mass, lifetimes, current mass, surface helium, N/C and N/O ratios.

The models are compared with models using the standard nuclear reaction obtained from NACRE. From Table 6.2 we find that the updated reaction rates do not affect the lifetimes, mass and surface abundances of the models until the end of H-burning. During the He-burning until the end of the burning, the N/C and N/O ratios are higher when using standard reaction rates compared to the updated reaction rates for the rotating models. Comparison of these surface abundances between the models using standard reaction rates and updated reaction rates can be seen in Figs. 6.18 and 6.19.

For the $20 M_{\odot}$ rotating model, we observe there are changes in the production of ^{12}C and ^{14}N at the surface using the updated reaction rates. Surface abundance of ^{12}C is

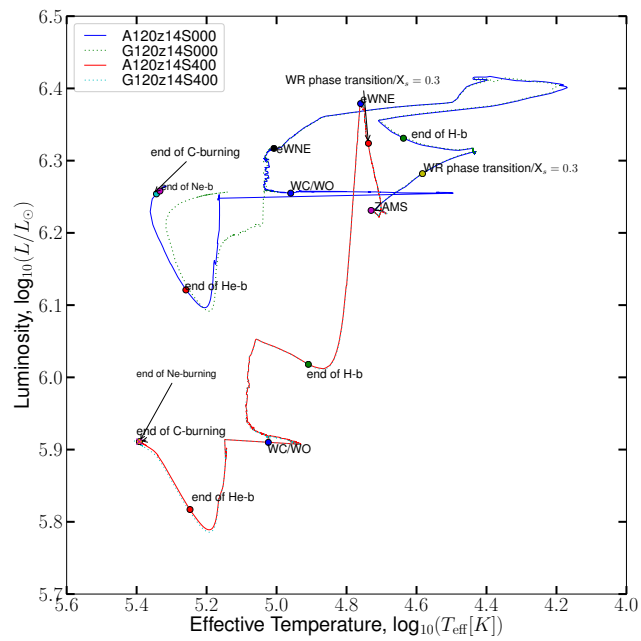


Figure 6.15: HR diagrams of $120 M_{\odot}$ rotating and non-rotating models with comparison to models using standard nuclear reaction rates.

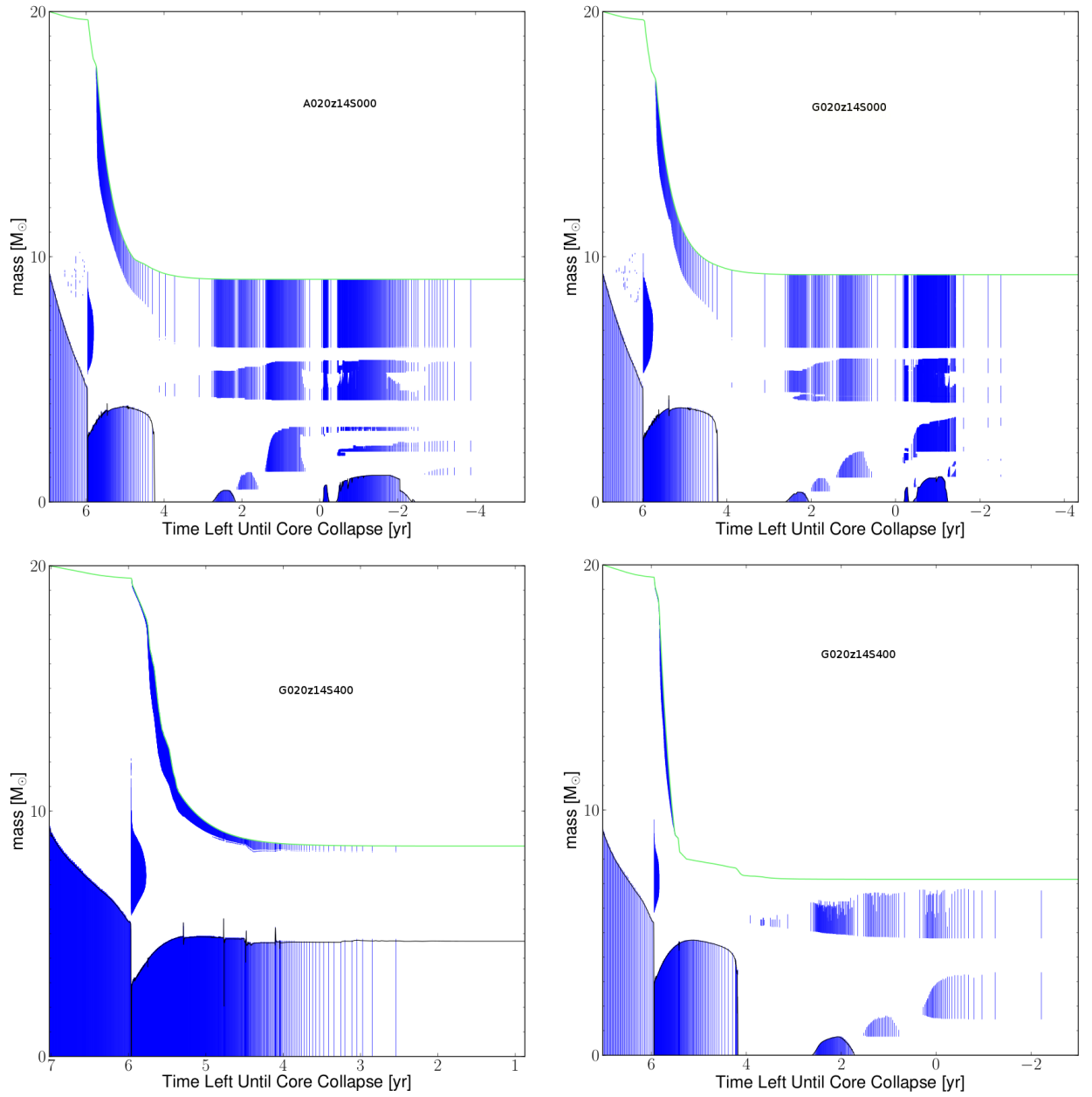


Figure 6.16: Kippenhahn diagrams of $20 M_{\odot}$ rotating and non-rotating models with comparison to models using standard nuclear reaction rates. The models with updated reaction rates are on the left panels and models using standard rates are on the right panels.

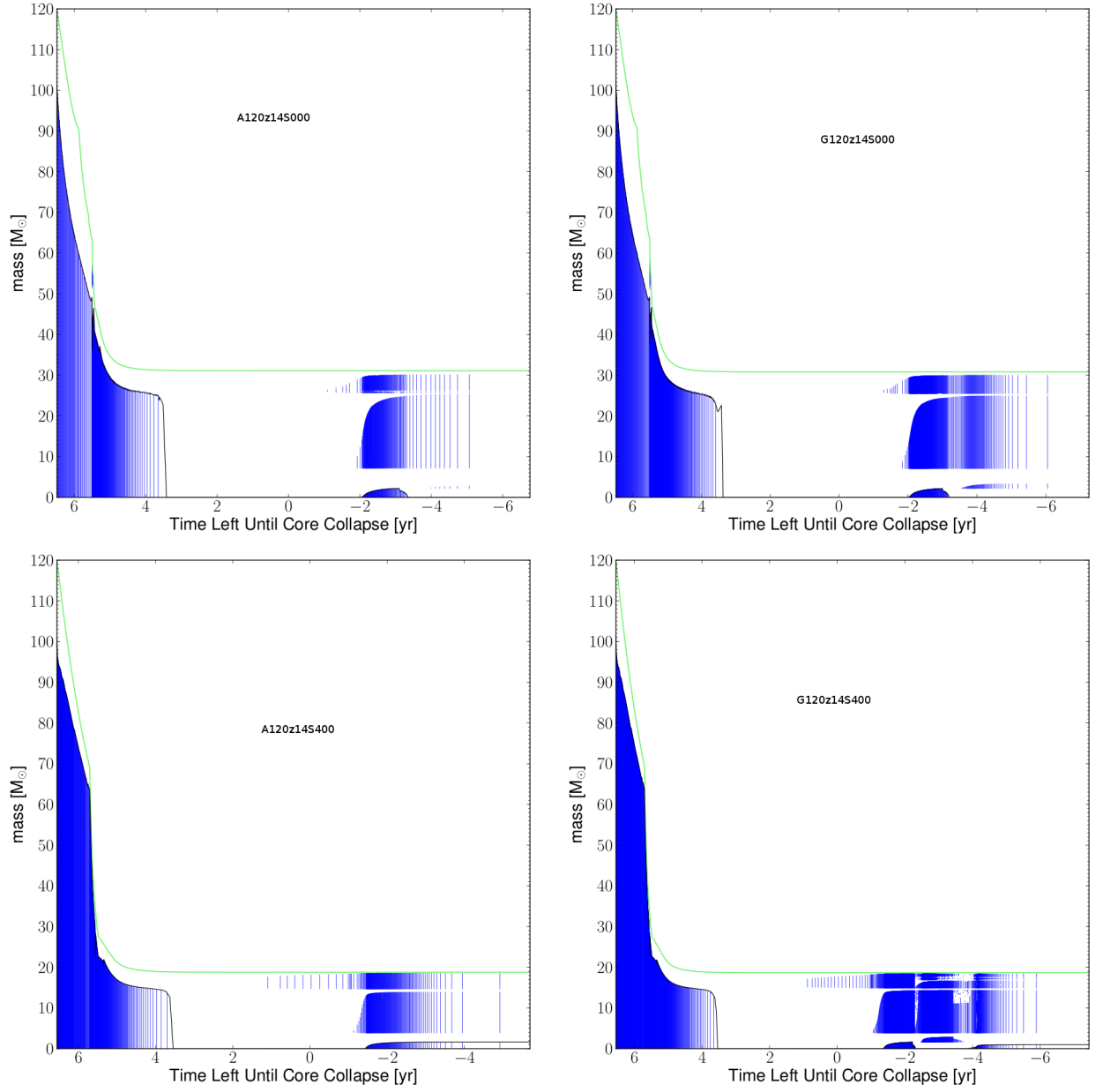
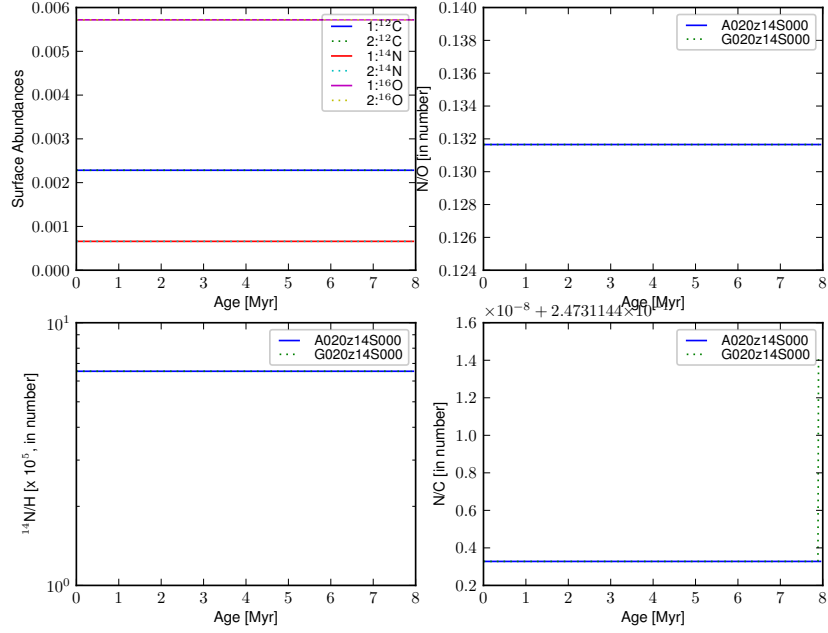


Figure 6.17: Kippenhahn diagrams of 120 M_{\odot} rotating and non-rotating models with comparison to models used standard nuclear reaction rates. The models with updated reaction rates are on the left panels and models using standard rates are on the right panels.

higher which reflects the higher central abundance of ^{12}C . This is due to the rotation induced mixing in the model. For surface abundance of ^{14}N , the model with the updated reaction rates produces lower ^{14}N compared to the model with standard reaction rates. These changes thus effects the ratio of N/H, N/C and N/C. Most of these ratios are lower compared to the standard nuclear reaction models. These changes are the result of the surface induced mixing by rotation. For non-rotating models, no significant changes can be seen in the evolution of He and H at the surface.

For $120 M_{\odot}$ for both rotating and non-rotating models, surface abundances of ^{12}C and ^{14}N give similar results for the $20 M_{\odot}$ rotating model except the ratio of N/H and N/O do not differ much between updated reaction model and standard reaction model. Higher ^{12}C at the surface of $120 M_{\odot}$ gives lower ratio of N/C. This is due to the strong mass loss occurring in the very massive stars especially at solar metallicity during H-burning stage.

Models: 1:A020z14S000, 2:G020z14S000



Models: 1:A020z14S400, 2:G020z14S400

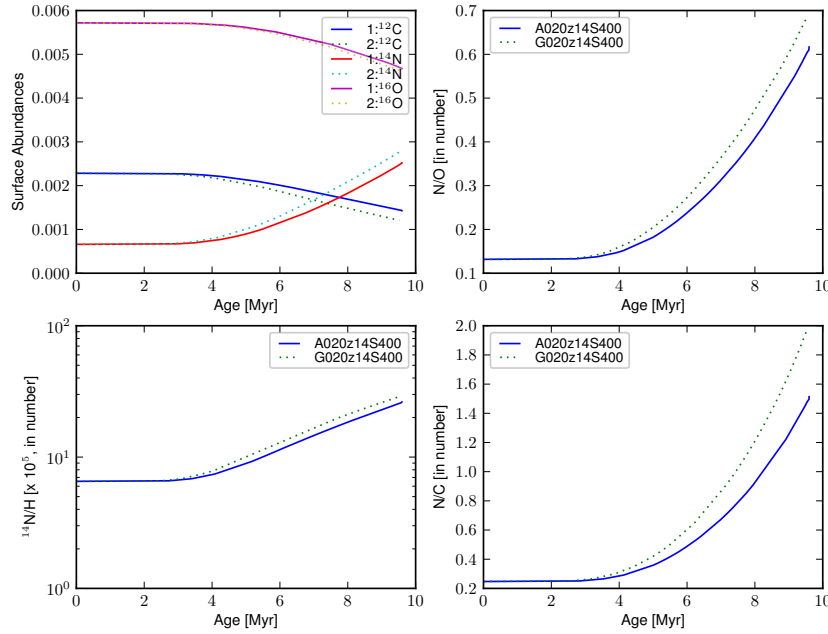
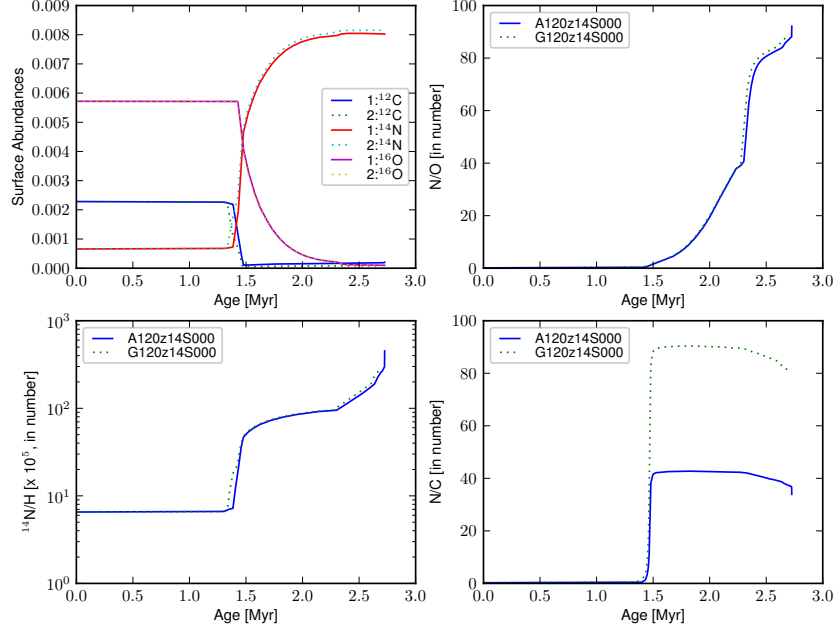


Figure 6.18: Surface abundances of $20 M_{\odot}$ solar metallicity for non-rotating model (upper panel) and rotating models (lower panel). Our models, A020z14z000 and A020z14z400 are compared with models using the standard nuclear reaction rates, G020z14S000 and G020z12S400.

Models: 1:A120z14S000, 2:G120z14S000



Models: 1:A120z14S400, 2:G120z14S400

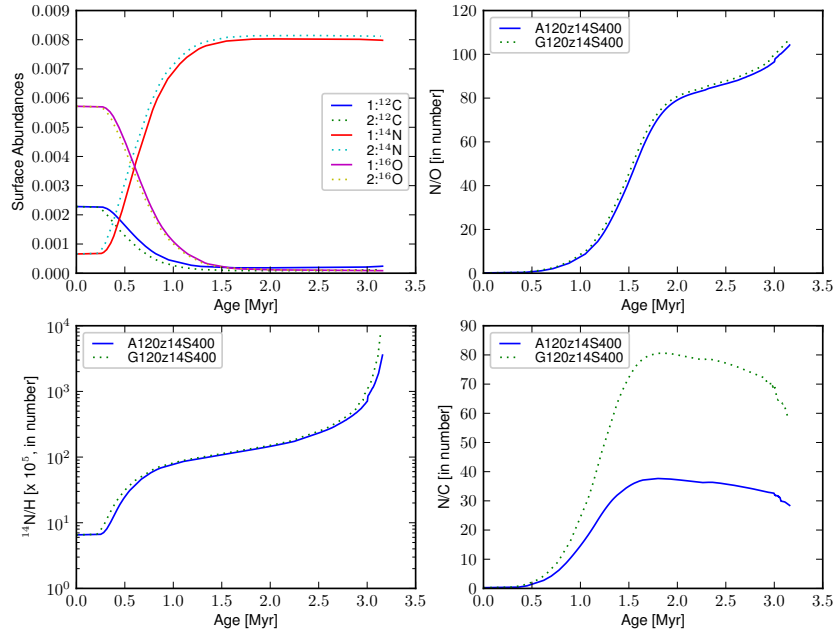


Figure 6.19: Surface abundances of $120 M_{\odot}$ solar metallicity for non-rotating model (upper panel) and rotating models (lower panel). Our models, A020z14z000 and A020z14z400 are compared with models using the standard nuclear reaction rates, G120z14S000 and G120z12S400.

Table 6.2: Properties of the stellar models at the end of H- and He- burning phases. We compare our models with models using the standard reaction rates.

Model	M_{ini}	End of H-burning						End of He-burning					
		t_H	M	v_{surf}	He	N/C	N/O	t_{He}	M	v_{surf}	He	N/C	N/O
A020z14z000	20	7.796	19.7	-	0.266	0.289	0.115	0.877	9.5	-	0.4908	24.17	3.309
G020z14z000	20	7.748	19.7	-	0.266	0.289	0.115	0.867	9.2	-	0.4989	42.21	3.616
A020z14z400	20	9.506	19.5	102.42	0.298	1.735	0.532	1.049	8.7	0.010	0.5842	29.69	3.434
G020z14z400	20	9.504	19.5	112.42	0.302	2.317	0.602	1.049	10.2	0.030	0.5496	23.79	2.729
A120z14z000	120	2.703	63.6	-	0.783	43.075	76.684	0.304	31.2	-	0.2466	1.33e-18	2.20e-18
G120z14z000	120	2.671	63.7	-	0.782	94.974	77.250	0.300	30.9	-	0.2423	1.34e-18	1.82e-18
A120z14z400	120	3.182	34.6	98.17	0.985	28.180	95.309	0.356	18.9	1.620	0.2920	1.42e-18	3.53e-18
G020z14z400	120	3.137	34.6	96.93	0.985	60.904	95.565	0.351	18.8	1.580	0.2919	4.05e-18	1.00e-18

6.4.2 Central abundances

In this section, we analyse the central abundances of both models using the standard reaction rates (models with initial G) and the updated reaction rates (models with initial A). For both $20 M_{\odot}$ and $120 M_{\odot}$ models, CNO cycle plays a dominant role at generating energy in the center of the star during H-burning. The relevant updated reactions are included in the nuclear network, i.e. $^{12}\text{C}(p,\gamma)^{13}\text{N}$, $^{15}\text{N}(p,\gamma)^{16}\text{O}$ and $^{16}\text{O}(p,\gamma)^{17}\text{F}$.

The results are presented in Figs. 6.20 - 6.23. We plot ^{12}C , ^{13}C , ^{14}N and ^{16}O abundances at the centre of the stars. From the models, we find that ^{12}C content is higher when using the updated nuclear reaction rates compared to the standard nuclear reaction. This is due to the fact that our updated reaction rate of $^{12}\text{C}(p,\gamma)^{13}\text{N}$ is low thus the equilibrium abundance of ^{12}C in the CNO cycle is higher.

Other chemical abundances do not show any significant changes during H-burning. Interaction between ^{15}N with protons does not always produce $^{16}\text{O}+p$ but it also produces $^{12}\text{C}+\alpha$. The $^{15}\text{N}(p,\alpha)^{12}\text{C}$ reaction terminates the CN cycle. But the branching ratio to the second subcycle which begins with $^{15}\text{N}(p,\gamma)^{16}\text{O}$ reaction has the probability of about 10^{-4} . Hence, in this case, $^{15}\text{N}(p,\gamma)^{16}\text{O}$ reaction only occur $1/10^4$ compared to the $^{15}\text{N}(p,\alpha)^{12}\text{C}$ reaction during the evolution. For central ^{16}O , only $120 M_{\odot}$ rotating model shows slight increase during the end of H-burning when using the updated reaction rate. This might be due to the strong mass loss and rotation effects that enhances the ^{16}O abundance at the centre.

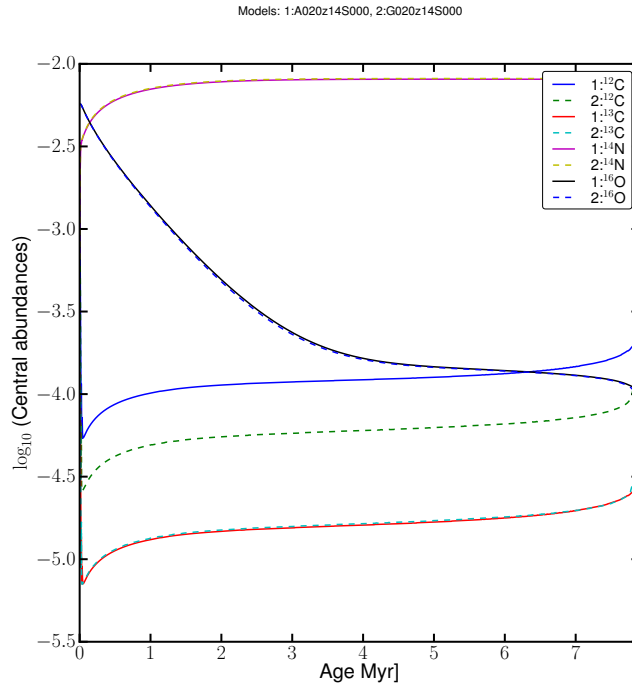


Figure 6.20: Evolution of ^{12}C , ^{14}N and ^{16}O central abundances of $20 M_{\odot}$ non-rotating models.

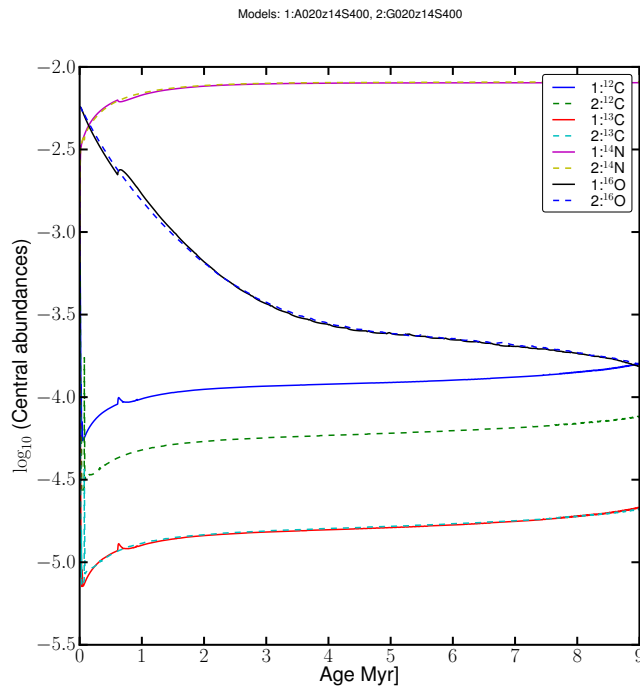


Figure 6.21: Evolution of ^{12}C , ^{14}N and ^{16}O central abundances of $20 M_{\odot}$ rotating models.

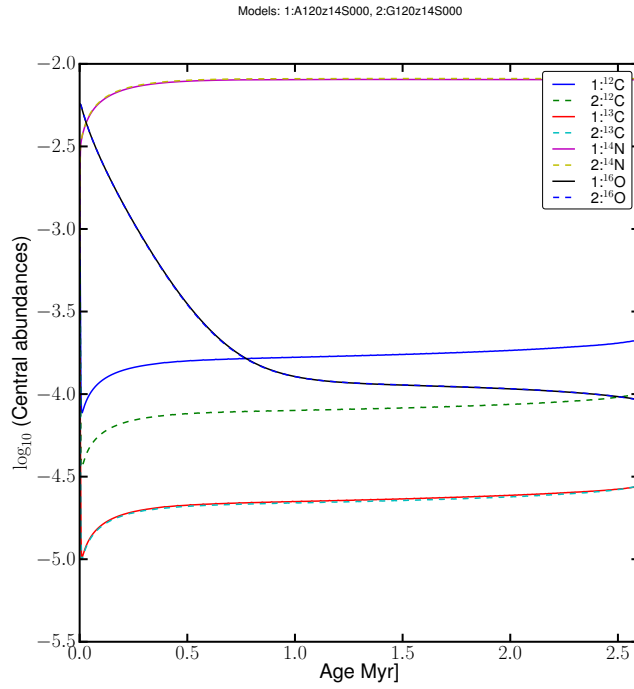


Figure 6.22: Evolution of ^{12}C , ^{14}N and ^{16}O central abundances of $120 M_{\odot}$ non-rotating models.

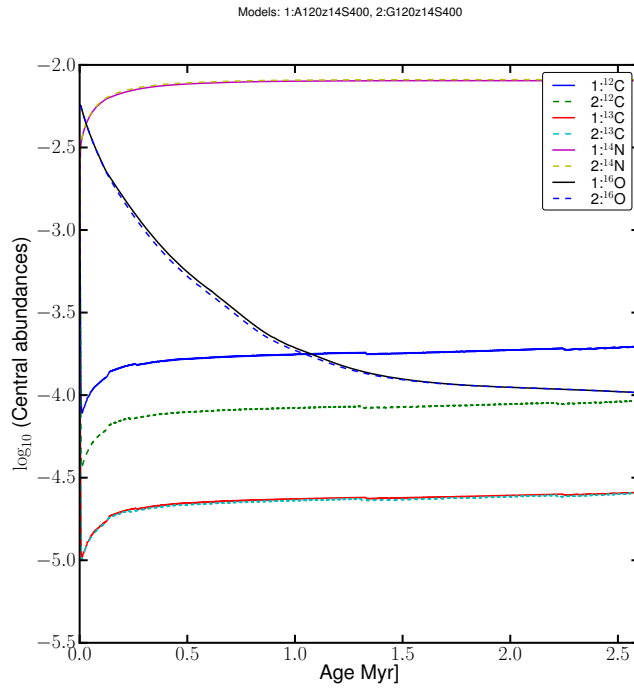


Figure 6.23: Evolution of ^{12}C , ^{14}N and ^{16}O central abundances of $120 M_{\odot}$ rotating models.

6.5 Summary

In this chapter we have calculated an updated nuclear reaction rate for ${}^3\text{He}({}^3\text{He},2\text{p}){}^4\text{He}$, ${}^3\text{He}(\alpha,\gamma){}^7\text{Be}$, ${}^{12}\text{C}(p,\gamma){}^{13}\text{N}$, ${}^{15}\text{N}(p,\gamma){}^{16}\text{O}$ and ${}^{16}\text{O}(p,\gamma){}^{17}\text{F}$ using WKB approximation. This method provides an alternative method in obtaining precise non-resonant nuclear reaction rates. In standard calculation of nuclear reaction rates, $\langle\sigma v\rangle$ first-order approximation is used in order to obtain the astrophysical S-factor in the low-energy region. We have presented an example of the difference in the exact and standard probability in Fig. 6.2. We also recalculated the S-factor and the nuclear reaction rate of each reaction that we have chosen. Although the S-factor is much lower than the S-factor obtained from experiments, the value of $\langle\sigma v\rangle$ at low energy is agreeable with the $\langle\sigma v\rangle$ calculated from NACRE.

The impact of this updated nuclear reaction rates on the evolution of very massive stars are studied in this chapter. We obtained higher central ${}^{12}\text{C}$ contents throughout the H-burning stage compared to models using the standard reaction rates. This is due to the low reaction rate of ${}^{12}\text{C}(p,\gamma){}^{13}\text{N}$ which enhances the ${}^{12}\text{C}$ production. We observe slightly lower ${}^{14}\text{N}$ at the center of the star. These differences influence the changes in the surface abundances of the models. From the models using the updated reaction rates, all these models have lower ratio of N/C except for non-rotating $20 M_{\odot}$ model. The non-rotating $20 M_{\odot}$ model N/C ratio is unchanged. As reflected in the central burning, the higher production of ${}^{12}\text{C}$ also give higher ${}^{12}\text{C}$ at the surface. For $20 M_{\odot}$ rotating model, this impact is due to the rotation induced mixing which transports the central ${}^{12}\text{C}$ to the surface while for $120 M_{\odot}$, this effect is due to the strong mass loss experienced by very massive stars.

Chapter 7

Conclusions and Future Work

This chapter contains the summary of the work done, the results obtained and future prospects.

7.1 Stellar evolution models-life and fate of very massive stars

We have calculated a grid of stellar models of very massive stars at SMC, LMC and solar metallicities. Our study is motivated by the finding of a very massive star known to date, R136a1 (Crowther et al., 2010) and the observation of PCSN candidate, SN2007bi (Gal-Yam et al., 2009).

Our stellar evolution models on the main sequence match the observations of very massive stars in NGC3603 and R136 (Crowther et al., 2010). From this work, the initial mass is around $148 M_{\odot}$ for NGC3603 A1a and $320 M_{\odot}$ for the R136 a1. Our models enabled us to determine the initial mass of these stars and the most massive star that has birth mass of $320 M_{\odot}$, as well as other very massive stars, well above the commonly accepted upper mass limit $\sim 150 M_{\odot}$ (Figer, 2005)

From the main sequence, we evolve the models further until at least the end of He

burning. The major uncertainty in the modelling of massive stars is mass loss and by using different mass loss prescriptions during the transition of WR we study the impact of this uncertainty on the fate of very massive stars. We find that the Vink et al. (2001) mass loss prescription, if implemented in the models, gives higher final mass compared to models using the mass loss prescription by Nugis & Lamers (2000). Using mass loss rates comparable to Vink et al. (2001), the fate of the stars would change where PCSN could occur even at solar metallicity with smaller mass lower than $300 M_{\odot}$.

Our models end up as PCSN are models at LMC metallicity with mass around $500 M_{\odot}$ and rotating SMC metallicity models with mass $120 < M_{\odot} < 280$. Other than that, the stars will die as black holes or core-collapse supernovae.

We have checked whether our models can match the properties of the PCSN candidate, SN2007bi (Gal-Yam et al., 2009). From our analysis, we find that our model can reproduce the properties of SN2007bi for rotating stars at around $150 M_{\odot} < M < 175 M_{\odot}$ at SMC metallicity.

During this work, we encountered the limitation in the code. The code does not include the pair-creation formation which is needed to properly model the late phases of very massive stars.

7.2 Neutrino energy loss

The neutrino energy loss has been updated in Chapter 5. The neutrino energy loss using Itoh et al. (1996) is used. Significant changes can be observed in $20 M_{\odot}$ model while for the higher mass, this updated neutrino energy loss does not have any significant effect since the photoneutrino process contributes the highest energy loss in the models. This is due to the fact Itoh et al. (1996) have used the same formulation as in Itoh et al. (1989). However, there are differences in bremsstrahlung and plasma processes using Itoh et al. (1996). Although the effect in bremsstrahlung is huge it does not change the evolution

of the models due to it is less dominating effects compared to the photoneutrino process.

7.3 Updated nuclear reaction rates

The stellar models of massive stars using the updated nuclear reaction rates are presented in Chapter 6. This work is independent from Chapters 3 and 5. Here we include the reactions in the Geneva stellar evolution code that are relevant to the H-burning in the CNO cycle, i.e $^{12}\text{C}(p,\gamma)^{13}\text{N}$, $^{15}\text{N}(p,\gamma)^{16}\text{O}$ and $^{16}\text{O}(p,\gamma)^{17}\text{F}$. In this work, our updated reaction rates have the most influence in the production of ^{12}C . Since our updated reaction rate of $^{12}\text{C}(p,\gamma)^{13}\text{N}$ is low, the equilibrium abundance of ^{12}C in the CNO cycle is higher. We have investigated the changes at the surface and we find the changes at the center influence the surface abundances except in $20 M_{\odot}$ non-rotating models. The strong rotation induced mixing in the $20 M_{\odot}$ rotating model and the strong mass loss in both $120 M_{\odot}$ rotating and non-rotating models increase the production of ^{12}C at the surface.

7.4 Future work

In near future, we are going to explode these models and study the light curve of the explosion models. This will give complete analysis in determining the fate of very massive stars and PCSN. This work will be done in collaboration with Professor Alexander Heger. We are also planning to calculate the grid of low metallicity models using the same initial mass range in order to extend the study of the fate of very massive stars.

We are going to use the current models to assess whether the Eddington limit constraints the upper stellar mass limit. Based on our grid models, we can derive the theoretical mass - luminosity relations for very massive stars. Estimated Eddington factor, Γ_{Edd} from the sample stars can be compared with Γ_{Edd} from the models.

Several improvements of the code are planned in the near future. We are going to

include the recombination process in neutrino energy loss subroutine. In Chapter 5, we only successfully update the code until bremsstrahlung process using Itoh et al. (1996). This will complete the neutrino energy loss rates in the code. We are also going to implement the mass loss prescription from Vink et al. (2011) in the code that is suitable for massive stars in the range of 40-300 M_{\odot} .

The grids of low-metallicity models are planned in near future. This is the extension of the present grid. Comparison with all grids available will be done together with their fate. We also going to compare the low-metallicity grids with observations and other grids that are available in the literature.

Appendix A

List of Publications

1. The R136 star cluster hosts several stars whose individual masses greatly exceed the accepted $150 M_{\odot}$ stellar mass limit
Crowther, Paul A.; Schnurr, Olivier; Hirschi, Raphael; **Yusof, Norhasliza**; Parker, Richard J.; Goodwin, Simon P.; Kassim, Hasan Abu, Monthly Notices of the Royal Astronomical Society, Volume 408, Issue 2, pp. 731-751. (2010)
2. Life and Death of Very Massive Stars
Yusof, N.; Abu Kassim, H.; Hirschi, R.; Crowther, P.; Schnurr, O.; Parker, R.; Goodwin, S. Proceedings of the 11th Symposium on Nuclei in the Cosmos. 19-23 July 2010. Heidelberg, Germany (2010)
3. Charged-particle induced thermonuclear reaction rates of ${}^3\text{He}({}^3\text{He}, 2\text{p}){}^4\text{He}$, ${}^3\text{He}({}^4\text{He}, \gamma){}^7\text{Be}$ and ${}^7\text{Be}(\text{p}, \gamma){}^8\text{B}$ by using the exact tunneling probability
Norhasliza Yusof and Hasan Abu Kassim, Astrophysics and Space Science Volume 328, Numbers 1-2, 157-161 (2010)
4. Most Effective Energy in Thermonuclear Reactions of Some Light Nuclei
Yusof, Norhasliza; Kassim, Hasan Abu. Modern Physics Letters A, Volume 24, Issue 11-13, pp. 1071-1075 (2009)

Bibliography

- Abel, T., Bryan, G. L., & Norman, M. L. 2000, *Astrophys. J.*, 540, 39
- Anders, E. & Grevesse, N. 1989, *Geochimica et Cosmochimica Acta*, 53, 197
- Angulo, C., Arnould, M., Rayet, M., Descouvemont, P., Baye, D., Leclercq-Willain, C., Coc, A., Barhoumi, S., Aguer, P., Rolfs, C., Kunz, R., Hammer, J. W., Mayer, A., Paradellis, T., Kossionides, S., Chronidou, C., Spyrou, K., degl'Innocenti, S., Fiorentini, G., Ricci, B., Zavatarelli, S., Providencia, C., Wolters, H., Soares, J., Grama, C., Rahighi, J., Shotter, A., & Lamahi Racht, M. 1999, *Nuclear Physics A*, 656, 3
- Asplund, M., Grevesse, N., & Sauval, A. J. 2005, in *Astronomical Society of the Pacific Conference Series*, Vol. 336, *Cosmic Abundances as Records of Stellar Evolution and Nucleosynthesis*, ed. T. G. Barnes, III & F. N. Bash, 25
- Atkinson, R. D. E. & Houtermans, F. G. 1929, *Zeitschrift fur Physik*, 54, 656
- Barkat, Z., Rakavy, G., & Sack, N. 1967, *Physical Review Letters*, 18, 379
- Beaudet, G., Petrosian, V., & Salpeter, E. E. 1967, *Astrophys. J.*, 150, 979
- Beaumevielle, H., Bouchemha, A., Boudouma, Y., Boughrara, A., Ouichaoui, S., & Tsan, U. C. 1999, *Academie des Sciences Paris Comptes Rendus Serie B Sciences Physiques*, 327, 251
- Bethe, H. A. 1939, *Physical Review*, 55, 434

- Bethe, H. A. & Critchfield, C. L. 1938, *Physical Review*, 54, 248
- Bond, J. R., Arnett, W. D., & Carr, B. J. 1984, *Astrophys. J.*, 280, 825
- Braaten, E. 1991, *Physical Review Letters*, 66, 1655
- Braaten, E. & Segel, D. 1993, *Phys. Rev. D*, 48, 1478
- Bromm, V., Coppi, P. S., & Larson, R. B. 1999, *Astrophys. J. Lett.*, 527, L5
- Burbidge, E. M., Burbidge, G. R., Fowler, W. A., & Hoyle, F. 1957, *Reviews of Modern Physics*, 29, 547
- Cassinelli, J. P., Mathis, J. S., & Savage, B. D. 1981, *Science*, 212, 1497
- Castor, J. I., Abbott, D. C., & Klein, R. I. 1975, *Astrophys. J.*, 195, 157
- Chaboyer, B. & Zahn, J.-P. 1992, *Astron. Astrophys.*, 253, 173
- Crowther, P. A. 2007, *ARA&A*, 45, 177
- Crowther, P. A. & Dessart, L. 1998, *Mon. Not. R. Astron. Soc.*, 296, 622
- Crowther, P. A., Hadfield, L. J., Clark, J. S., Negueruela, I., & Vacca, W. D. 2006, *Mon. Not. R. Astron. Soc.*, 372, 1407
- Crowther, P. A., Schnurr, O., Hirschi, R., Yusof, N., Parker, R. J., Goodwin, S. P., & Kassim, H. A. 2010, *Mon. Not. R. Astron. Soc.*, 408, 731
- Cunha, K., Hubeny, I., & Lanz, T. 2006, *Astrophys. J. Lett.*, 647, L143
- Daepfen, W., Mihalas, D., Hummer, D. G., & Mihalas, B. W. 1988, *Astrophys. J.*, 332, 261
- de Jager, C., Nieuwenhuijzen, H., & van der Hucht, K. A. 1988, *A&AS*, 72, 259

- de Koter, A., Heap, S. R., & Hubeny, I. 1997, *Astrophys. J.*, 477, 792
- Dicus, D. A., Kolb, E. W., Schramm, D. N., & Tubbs, D. L. 1976, *Astrophys. J.*, 210, 481
- Ekström, S., Georgy, C., Eggenberger, P., Meynet, G., Mowlavi, N., Wyttenbach, A., Granada, A., Decressin, T., Hirschi, R., Frischknecht, U., Charbonnel, C., & Maeder, A. 2012, *Astron. Astrophys.*, 537, A146
- Ekström, S., Meynet, G., Chiappini, C., Hirschi, R., & Maeder, A. 2008, *Astron. Astrophys.*, 489, 685
- Eldridge, J. J. & Vink, J. S. 2006, *Astron. Astrophys.*, 452, 295
- Esposito, S., Mangano, G., Miele, G., Picardi, I., & Pisanti, O. 2003, *Nuclear Physics B*, 658, 217
- Ferguson, J. W., Alexander, D. R., Allard, F., Barman, T., Bodnarik, J. G., Hauschildt, P. H., Heffner-Wong, A., & Tamanai, A. 2005, *Astrophys. J.*, 623, 585
- Figer, D. F. 2005, *Nature*, 434, 192
- Foellmi, C., Moffat, A. F. J., & Guerrero, M. A. 2003, *Mon. Not. R. Astron. Soc.*, 338, 1025
- Frebel, A., Aoki, W., Christlieb, N., Ando, H., Asplund, M., Barklem, P. S., Beers, T. C., Eriksson, K., Fechner, C., Fujimoto, M. Y., Honda, S., Kajino, T., Minezaki, T., Nomoto, K., Norris, J. E., Ryan, S. G., Takada-Hidai, M., Tsangarides, S., & Yoshii, Y. 2005, *Nature*, 434, 871
- Fukuda, I. 1982, *PASP*, 94, 271
- Gal-Yam, A., Mazzali, P., Ofek, E. O., Nugent, P. E., Kulkarni, S. R., Kasliwal, M. M., Quimby, R. M., Filippenko, A. V., Cenko, S. B., Chornock, R., Waldman, R., Kasen,

- D., Sullivan, M., Beshore, E. C., Drake, A. J., Thomas, R. C., Bloom, J. S., Poznanski, D., Miller, A. A., Foley, R. J., Silverman, J. M., Arcavi, I., Ellis, R. S., & Deng, J. 2009, *Nature*, 462, 624
- Georgy, C., Meynet, G., Walder, R., Folini, D., & Maeder, A. 2009, *Astron. Astrophys.*, 502, 611
- Gräfener, G. & Hamann, W.-R. 2008, *Astron. Astrophys.*, 482, 945
- Haft, M., Raffelt, G., & Weiss, A. 1994, *Astrophys. J.*, 425, 222
- Heger, A., Fryer, C. L., Woosley, S. E., Langer, N., & Hartmann, D. H. 2003, *Astrophys. J.*, 591, 288
- Heger, A. & Woosley, S. E. 2002, *Astrophys. J.*, 567, 532
- Heney, L. G., Forbes, J. E., & Gould, N. L. 1964, *Astrophys. J.*, 139, 306
- Hirschi, R., Meynet, G., & Maeder, A. 2004, *Astron. Astrophys.*, 425, 649
- Hoyle, F. & Fowler, W. A. 1960, *Astrophys. J.*, 132, 565
- Huang, W. & Gies, D. R. 2006, *Astrophys. J.*, 648, 591
- Humblet, J., Fowler, W. A., & Zimmerman, B. A. 1987, *Astron. Astrophys.*, 177, 317
- Hummer, D. G. & Mihalas, D. 1988, *Astrophys. J.*, 331, 794
- Hunter, D. A., Shaya, E. J., Holtzman, J. A., Light, R. M., O'Neil, Jr., E. J., & Lynds, R. 1995, *Astrophys. J.*, 448, 179
- Iglesias, C. A. & Rogers, F. J. 1996, *Astrophys. J.*, 464, 943
- Itoh, N., Adachi, T., Nakagawa, M., Kohyama, Y., & Munakata, H. 1989, *Astrophys. J.*, 339, 354

- Itoh, N., Hayashi, H., Nishikawa, A., & Kohyama, Y. 1996, *Astrophys. J. Suppl. Ser.*, 102, 411
- Itoh, N. & Kohyama, Y. 1983, *Astrophys. J.*, 275, 858
- Itoh, N., Kohyama, Y., Matsumoto, N., & Seki, M. 1984, *Astrophys. J.*, 285, 304
- . 1993, *Astrophys. J.*, 404, 418
- Itoh, N., Mutoh, H., Hikita, A., & Kohyama, Y. 1992, *Astrophys. J.*, 395, 622
- Kasen, D., Heger, A., & Woosley, S. 2008, in *American Institute of Physics Conference Series*, Vol. 990, *First Stars III*, ed. B. W. O'Shea & A. Heger, 263–267
- Kawabata, K. S., Tanaka, M., Maeda, K., Hattori, T., Nomoto, K., Tominaga, N., & Yamanaka, M. 2009, *Astrophys. J.*, 697, 747
- Kippenhahn, R. & Thomas, H.-C. 1970, in *IAU Colloq. 4: Stellar Rotation*, ed. A. Slettebak, 20
- Kippenhahn, R., Weigert, A., & Hofmeister, E. 1967, *Methods in Computational Physics*, ed. Alder B., Fernbach S. and Rotenberg M (Academic Press)
- Kohyama, Y., Itoh, N., Obama, A., & Hayashi, H. 1994, *Astrophys. J.*, 431, 761
- Kohyama, Y., Itoh, N., Obama, A., & Mutoh, H. 1993, *Astrophys. J.*, 415, 267
- Langer, N. 2009, *Nature*, 462, 579
- Langer, N. & El Eid, M. F. 1986, *Astron. Astrophys.*, 167, 265
- Langer, N., Norman, C. A., de Koter, A., Vink, J. S., Cantiello, M., & Yoon, S. 2007, *Astron. Astrophys.*, 475, L19
- Lejeune, T. & Schaerer, D. 2001, *Astron. Astrophys.*, 366, 538

- Lucy, L. B. & Solomon, P. M. 1970, *Astrophys. J.*, 159, 879
- Maeder, A. 1983, *Astron. Astrophys.*, 120, 130
- . 2003, *Astron. Astrophys.*, 399, 263
- . 2009, *Physics, Formation and Evolution of Rotating Stars*, ed. Maeder, A.
- Maeder, A., Georgy, C., & Meynet, G. 2008, *Astron. Astrophys.*, 479, L37
- Maeder, A. & Meynet, G. 1994, *Astron. Astrophys.*, 287, 803
- . 2000, *ARA&A*, 38, 143
- Martins, F., Hillier, D. J., Paumard, T., Eisenhauer, F., Ott, T., & Genzel, R. 2008, *Astron. Astrophys.*, 478, 219
- Massey, P. & Hunter, D. A. 1998, *Astrophys. J.*, 493, 180
- Meynet, G. & Maeder, A. 1997, *Astron. Astrophys.*, 321, 465
- . 2005, *Astron. Astrophys.*, 429, 581
- Meynet, G., Maeder, A., Schaller, G., Schaerer, D., & Charbonnel, C. 1994, *A&AS*, 103, 97
- Mihalas, D., Dappen, W., & Hummer, D. G. 1988, *Astrophys. J.*, 331, 815
- Mokiem, M. R., de Koter, A., Vink, J. S., Puls, J., Evans, C. J., Smartt, S. J., Crowther, P. A., Herrero, A., Langer, N., Lennon, D. J., Najarro, F., & Villamariz, M. R. 2007, *Astron. Astrophys.*, 473, 603
- Moriya, T., Tominaga, N., Tanaka, M., Maeda, K., & Nomoto, K. 2010, *Astrophys. J. Lett.*, 717, L83
- Munakata, H., Kohyama, Y., & Itoh, N. 1985, *Astrophys. J.*, 296, 197

- . 1987, *Astrophys. J.*, 316, 708
- N. Walborn (STScI) et al., WFPC2, H. N. 2001, *Star Cluster R136 Bursts Out*
- Nabi, J. & Sajjad, M. 2008, *Phys. Rev. C*, 77, 055802
- NASA, ESA, H. H. S.-E. H. C. 2007, *Starburst Cluster in NGC 3603*
- Nomoto, K., Umeda, H., Maeda, K., Ohkubo, T., Deng, J., & Mazzali, P. 2003, *Nuclear Physics A*, 718, 277
- Nugis, T. & Lamers, H. J. G. L. M. 2000, *Astron. Astrophys.*, 360, 227
- Ohkubo, T., Nomoto, K., Umeda, H., Yoshida, N., & Tsuruta, S. 2009, *Astrophys. J.*, 706, 1184
- Ostriker, J. P. & Gnedin, N. Y. 1996, *Astrophys. J. Lett.*, 472, L63
- Rakavy, G. & Shaviv, G. 1967, *Astrophys. J.*, 148, 803
- Rogers, F. J. & Iglesias, C. A. 1996, in *Bulletin of the American Astronomical Society*, Vol. 28, American Astronomical Society Meeting Abstracts #188, 915
- Rogers, F. J. & Nayfonov, A. 2002, *Astrophys. J.*, 576, 1064
- Rolfs, C. & Azuma, R. E. 1974, *Nuclear Physics A*, 227, 291
- Rolfs, C. & Rodney, W. S. 1974, *Nuclear Physics A*, 235, 450
- Salpeter, E. E. 1952, *Astrophys. J.*, 115, 326
- Savage, B. D., Fitzpatrick, E. L., Cassinelli, J. P., & Ebbets, D. C. 1983, *Astrophys. J.*, 273, 597
- Schaller, G., Schaerer, D., Meynet, G., & Maeder, A. 1992, *A&AS*, 96, 269

- Schinder, P. J., Schramm, D. N., Wiita, P. J., Margolis, S. H., & Tubbs, D. L. 1987, *Astrophys. J.*, 313, 531
- Schnurr, O., Casoli, J., Chené, A., Moffat, A. F. J., & St-Louis, N. 2008, *Mon. Not. R. Astron. Soc.*, 389, L38
- Schnurr, O., Chené, A., Casoli, J., Moffat, A. F. J., & St-Louis, N. 2009, *Mon. Not. R. Astron. Soc.*, 397, 2049
- Smith, N., Li, W., Foley, R. J., Wheeler, J. C., Pooley, D., Chornock, R., Filippenko, A. V., Silverman, J. M., Quimby, R., Bloom, J. S., & Hansen, C. 2007, *Astrophys. J.*, 666, 1116
- Stacy, A., Greif, T. H., & Bromm, V. 2010, *Mon. Not. R. Astron. Soc.*, 403, 45
- Sung, H. & Bessell, M. S. 2004, *Astron. J.*, 127, 1014
- Turatto, M. 2003, *ArXiv Astrophysics e-prints*
- Umeda, H. & Nomoto, K. 2002, *Astrophys. J.*, 565, 385
- Vink, J. S., de Koter, A., & Lamers, H. J. G. L. M. 1999, *Astron. Astrophys.*, 350, 181
- . 2001, *Astron. Astrophys.*, 369, 574
- Vink, J. S., Muijres, L. E., Anthonisse, B., de Koter, A., Gräfener, G., & Langer, N. 2011, *Astron. Astrophys.*, 531, A132
- Weidner, C. & Kroupa, P. 2006, *Mon. Not. R. Astron. Soc.*, 365, 1333
- Weigelt, G. & Baier, G. 1985, *Astron. Astrophys.*, 150, L18
- Wellstein, S. & Langer, N. 1999, *Astron. Astrophys.*, 350, 148
- Woosley, S. E., Blinnikov, S., & Heger, A. 2007, *Nature*, 450, 390

- Woosley, S. E., Heger, A., & Weaver, T. A. 2002, *Reviews of Modern Physics*, 74, 1015
- Yoon, S.-C., Woosley, S. E., & Langer, N. 2010, *Astrophys. J.*, 725, 940
- Yoshida, T. & Umeda, H. 2011, *Mon. Not. R. Astron. Soc.*, 412, L78
- Yungelson, L. R., van den Heuvel, E. P. J., Vink, J. S., Portegies Zwart, S. F., & de Koter, A. 2008, *Astron. Astrophys.*, 477, 223
- Yusof, N. & Kassim, H. A. 2009, *Modern Physics Letters A*, 24, 1071
- . 2010, *Astrophys. Space Sci.*, 328, 157
- Zahn, J.-P. 1992, *Astron. Astrophys.*, 265, 115